Consortium

for

Small-Scale Modelling

Newsletter

January 2010 ***No. 10***

Deutscher Wetterdienst

MeteoSwiss

Ufficio Generale Spacio Aero e Meteorologia

ΕΘΝΙΚΗ ΜΕΤΕΩΡΟΛΟΓΙΚΗ ΥΠΗΡΕΣΙΑ

Instytucie Meteorogii i Gospodarki Wodnej

Administratia Nationala de Meteorologie

Agenzia Regionale per la Protezione Ambientale dell Emilia-Romagna: Servizio Idro Meteo

Agenzia Regionale per la Protezione Ambientale dell Piemonte

Centro Italiano Ricerche Aerospaziali

Amt für GeoInformationswesen der Bundeswehr

Federal Service for Hydrometeorology and Environmental Monitoring

www.cosmo-model.org

Editors: Ulrich Schättler (DWD); Cosmin Barbu (NMA)
Printed at Deutscher Wetterdienst, P.O. Box 100465, 63004 Offenbach am Main

Table of Contents

1 Introduction

This COSMO Newsletter documents a few of the many presentations given at the last COSMO General Meeting which took place from 7 to 11 September 2009 in Offenbach, Germany. With over 100 participants, it was the largest COSMO General Meeting since its beginning in 1999.

Additional to this Newsletter, final reports of the COSMO Priority Projects VERSUS and SREPS have in the meantime been published as COSMO Technical Reports, and the QPF Priority Project has published its final results in the December 2009 issue of Meteorologische Zeitschrift. This reflects our aim to more often publish in peer-reviewed journals rather than COSMO-internal publications to further increase the visibility of COSMO.

With Russia as the newest member of COSMO, the next COSMO General Meeting will take place from 6 to 10 September 2010 in Moscow, Russia. - See you there!

Marco Arpagaus
COSMO Scientific Project Manager

Figure 1: Participants of the 11th COSMO General Meeting in Offenbach

Soil initialization strategy for the COSMO model

Francesca Di Giuseppe, Giovanni Bonafé, Davide Cesari

ARPA-Servizio IdroMeteoClima, Bologna, Italy

1 Introduction

Soil initialization is not a straightforward task for a number of reasons. Firstly there are almost no suitable measurements for operational analysis. In situ observations are rare and heterogeneous. The Global Soil Moisture Data Bank project [5] is an example of collection, dissemination, and analysis of gravimetric observations of soil moisture and temperature data from around 600 sites over the globe, but until now has served mainly the scope of creating a dataset for verification and initialization of climate simulation, without attempting to satisfy the real-time needs. Remotely sensed surface soil moisture data are available with mostly daily frequancy, but the detected radiation is directly linked only to the model's uppermost soil layer and therefore can only provide partial information. Moreover soil moisture retrieval from microwave frequencies requires accurate specification of the vegetation cover and soil type at the pixel location which, is not usually possible with the desidered precision. In addition to the lack of useful observations, it has to be mentioned the small representativity of soil measurements, where they exist. Correlation lenght for soil moisture, for example, can be as small as 10 m [8], making the design of an observational network almost an utopia.

The need for soil initialization without representative measurements has led the interest in indirect determination of soil prognostic variables. In this work, three different choices to initialise limited area model soil fields are compared, with the aim of identifying the most suitable strategy which combines ease of implementation, improvement in forecast skills and realistic estimations of soil paremeters, expecially in the light of hydrological applications. The regional model COSMO is used as limited area model forecasting system. The ECMWF, IFS model as global model.

For a three month long integration period spanning September-October-November (SON) 2008, the COSMO soil scheme TERRA is initialised either by a simple interpolation from the IFS soil moisture analysis or by fields generated by a COSMO previous integration or by a local soil analysis implemented with a variational scheme which uses screen level temperature to adjust the soil hydric content to minimises the distance between background and observations.

Extensive comparisons with observations show that most of the improvements are achieved when passing from a simple interpolation from ECMWF experiment to a free running COSMO model, while the soil moisture correction adds a marginal benefit to the prediction of surface fluxes. This suggests that keeping the model soil fields in good equilibrium with the soil scheme, especially for what concerns temperature, is more relevant than the subsequent correction of soil moisture provided by an analysis scheme.

2 Models, data and experiment design

In this section the set-up for the experiments is desccribed in details as well as the validation dataset used for the comparison. Since soil moisture analysis based on atmospheric observations is indirect and relies heavily on the underlying model, a brief summary of the main features of the land surface schemes in the operational ECMWF model (IFS) (used in the experiment named ECMWF) and in the COSMO model is given.

2.1 Experiment strategy

To isolate the effect of soil prognostic variables (i.e. temperature and humidity) on the model analysis, only the methods for initialzing those fields are varying among the three different experiments, while all other model configurations, external fields and boundary fields are kept invariant. The bottom layer soil temperature and humidity and the sea-surface temperature are interpolated from the global model IFS. In all experiments the atmospheric forcing is prescibed from the previous COSMO analysis as in the operational implementation. A three month long integration is performed starting the 1st of September 2008 (SON period). Each cycle lasts 24h starting at 00 UTC, 3-hourly boundary conditions are provided by IFS run at roughly 25 km resolution.

Three soil moisture intialization methods are implemented.

- *Initialization by interpolation from the ECMWF soil analysis (hereandafter ECMWF experiment).* The soil moisture and temperature fields are initialised using IFS analysis. At the beginning of each assimilation cycle the soil temperature and moisture fields are re-initialised with interpolated fields from ECMWF. The interpolation is firstly performed horizontally by taking the nearest IFS land point, and then vertically by a linear fit.
- *Free running soil initialization (hereandafter COSMO experiment).* The initialization is performed using the soil moisture and temperature fields from the previous COSMO run. After the first few days of start up the soil moisture of this experiment represents the equilibrium between the source terms (precipitation, dew, rime, snow) and the sink terms (evaporation from bare soil, transpiration from plant, run-off). The temperature profile is instead calculated with the force-restore method using the energy budget at the surface and it's therefore a direct consequence of the atmospheric model radiative forcing.
- *Free running soil initialization plus variational soil moisture analysis using surface 2 m synop observations (SMA experiment)* A local soil moisture analysis is performed using the variational scheme from [10]. The soil moisture is adjusted to minimize the distance between background and synop observations. The soil temperature is initialized from the previous COSMO run but, being the soil heat capacity a function of the soil moisture, it will predict a soil temperature profile which is different from the one of the COSMO experiment. Moreover a different soil moisture produces a different radiative coupling with the atmosphere. (sono giuste le correzioni qui?)

In table 1 a brief summary of the three experiment is reported

2.2 The COSMO soil moisture analysis

The soil moisture analysis used in the SMA experiment is based on a variational approach outlined in [10]. Firstly, a T_{2m}^{an} analysis field is obtained by optimal interpolation of synop observations and model background coming from the previous, T_{2m}^{fg}, COSMO run. Then, increments, ΔT_{2m}, at 12 and 15 UTC are calculated as $T_{2m}^{an} - T_{2m}^{fg}$. Finally, ΔT_{2m} are converted in moisture increments Δwg_i at the various soil levels using a parameterized form of

Exp Name	Temperature	Soil Moisture	Comments
ECMWF	Interpolated from IFS	Interpolated from IFS	
COSMO	From the previous COSMO run	Interpolated from COSMO	Bottom layer from IFS. First initialization from IFS
SMA	From the previous COSMO run	Adjusted with a local soil moisture analysis based on T_{2m} from the synop network	Bottom layer from IFS. First initialization from IFS

Table 1: Summary of the main characteristic of the three experiments under analysis

the jacobian $\frac{\partial w_g}{\partial T_{2m}}$. ΔT_{2m} are evaluated at two instants only when the soil-atmosphere coupling is supposed maximum. One should therefore expect that the major benefit from the soil moisture analysis arises primarily for situations the scheme is designed for, i.e. correcting forecast errors at the time the observations are assimilated, which is around noon. If the bias does not change its sign, the scheme should nevertheless be able to improve screen level errors caused by misspecification of bowen ratio at other lead times. On the other hand, in cases in which the soil is characterised by a substantial heating during daytime and cooling during night, as it happens for example in very dry soil conditions, then the application of this kind of soil moisture correction can exacerbate the reduction in soil thermal inertia with a worsening of the biases during nightime.

All these aspects will be investigated in the following sections.

2.3 The IFS soil analysis

The IFS soil scheme has four prognostic soil layers for moisture and temperature, with a free drainage and a zero heat flux condition at the bottom of the deepest layer. It also includes a precipitation interception layer and a skin temperature level. From the surface to the bottom, the layer thicknesses are, respectively, 0.07, 0.21, 0.72, and 1.89 m. The three top layers correspond to the root zone with a total depth of 1 m. The root density decreases exponentially with depth. The surface evaporation has a bare soil part controlled by soil moisture in the top layer and a vegetation part. The role of the vegetation is represented explicitly, through a transpiration term and an interception loss term corresponding to the evaporation of dew and intercepted rain at the potential rate. The transpiration is controlled by the leaf area index (LAI) and the stomatal conductance, which is regulated by the water availability in the root zone (top three layers) and the photosynthetically active solar radiation.

The IFS implements a soil moisture analysis which employs an Optimal Interpolation (OI) method proposed by [4]. Similarly to the SMA experiments described above, it is based on the analysis increments of 2 m temperature and relative humidity. Every 6 h, corrections applied in each soil layer (analysis increments) are linear combinations of atmospheric increments of 2 m temperature and relative humidity. The details of the method can be found in [1], while for full details on the quality of the IFS soil scheme and comparison with observations we refer to [7].

2.4 The verification dataset

The verification dataset is composed of three sources; surface flux measurements collected by the EU-funded research project CARBOEUROPE Integrated Project (CEIP), soil humidity data collected at the ARPA-SIMC meteo station located at San Pietro Capofiume (SPC) in the middle of the Italian Po Valley and the standard network of synop surface stations (400) which cover the COSMO-I7 domain.

The CARBOEUROPE project has the main aim of quantifying the relationship between carbon fluxes and vegetation characteristics. Therefore, great attention has been posed to locate observing stations over different land use/cover types. Measurements [1] are recorded since 2004 half-hourly on more than one hundred Eddy flux stations over Europe. The collected dataset therefore potentially possesses a good representativity of fluxes over different ecosystem types. The location and the vegetation characteristics of the stations which fall into the COSMO-I7 domain and were active during the validation period (SON 2008) are reported in table 1.

SPC meteo station is an intensive observation meteo station managed by ARPA-SIMC. In addition to the conventional meteorological measurements including SYNOP and TEMP variables, since 2007, is operating a Time-Domain Reflectometer (TDR) which measures soil water content and temperature profiles at 8 unevenly spaced levels below the ground between 10 and 100 cm. At the time of the experiments, SPC was not provided with instrumentation for surface fluxes measurements. Finally, global diagnostic are calculated using the synop

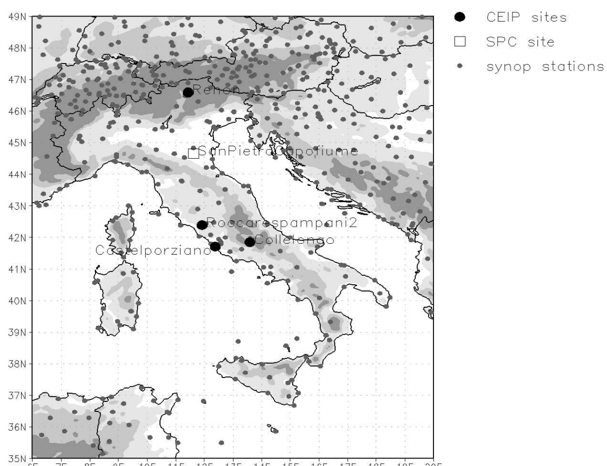

Figure 1: Type and location of the observational dataset used in this study. The displayed area is the operational domain of the COSMO-I7 suite.

network which comprises more then 400 surface stations over land. A map of the location of the stations used for the comparisons is reported in figure 1.

3 Problem diagnosis and impact of soil initialization

The main motivation for investigating a different soil moisture initialization strategy from the simple ECMWF interpolation are systematic annual biases in screen-level temperatures and humidities. As soil variables were initially interpolated from the IFS model it was often

[1] data available at www.carboeurope.org

observed that in the Po Valley, in early spring, temperatures were systematically too high while in summer they were too low. Figure 2 shows the diagnosis of the various problems to be faced. The seasonal variation of the outgoing longwave radiation clearly shows a shift in the annual wave phase, which is superinposed to the delay in the daily cycle. The soil model appears to be too conductinve and thus unable to buid-up thermal enargy during the summer. Moreover the weak daily cycle and its offset of few hours is responsible for a warm nighttime bias and a cold daytime bias. The first prevents the establishment of stable stratified PBL conditions typical of fog formation, the latter inhibits strong daytime mixing with dalay in the triggering of local convection.

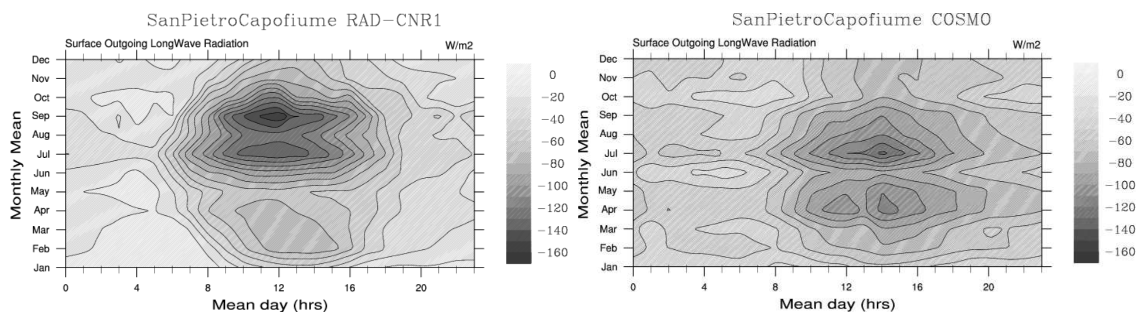

Figure 2: Seasonal versus daily outgoing longwave radiation at SanPietroCapofiume location as measured by the CNR-1 (upper panel) radiometer and as predicted by the COSMO-I7 model (lower panel). The data are averaged over two years 2007-2008.

The September-October-November 2008 period chosen for verification was a typical autumn season with an intermittent series of heavy precipitations and dry spelt days. Figure 3 shows the daily averaged observed precipitation and T_{2m} at the SanPietroCapofiume location. The first 10 days of October experienced no precipitation and have been marked as 'Dry Period'. Between the 24th of October to the 2nd of November several rain bands were moving estlerly from a low pressure minimum located in the middle of the mediterranean sea. Ten days of almost continous precipitation were recorded and have been marked as 'Wet period'. Figures 4 and 5 show the 3-hourly 2m temperature and relative humidity for the 10 days during the 'Dry Period' and the 'Wet period'.

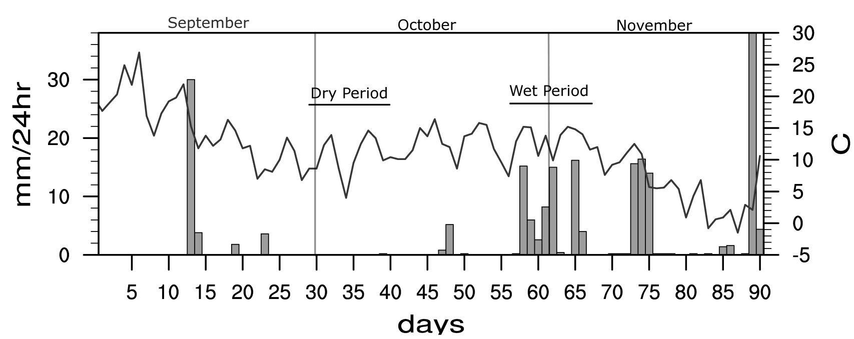

Figure 3: Observed daily precipitation at SPC during the SON period 2008

As expected the largest model discrepancy with the observations is at nightime during the dry period. These biases are exacerbated in the relative humidity due to the fact that the model is evidently also slighly dry. In dry condition, the best performance during daytime is achieved by the SMA initialization as one would expected. Under strong radiative forcing screen-level temperature, used as predictors, strongly depend on the soil moisture content. Moreover soil moisture incremens are only calculated during daytime and it is when the scheme works at its best. If, as it happens, the daytime bias has opposit sign with respect to the nighttime bias, the SMA approach will tend to dry-up a soil which is already too dry exacerbating the nighttime bias as shown, for example, at day 38 in figure 4 where correcting the max 2m temperature brings a worsening of the minimum night temperature. The limitation depited is inherent in the methodology which applays increments calculated at 'noon' to the whole assimilation window.

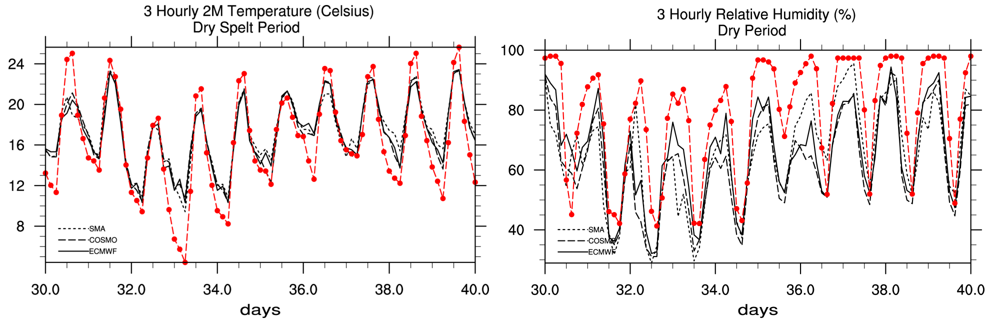

Figure 4: Time series of 3-hourly 2m temperature and relative humidity for the 10 days during the 'Dry Period'.Observations are from the rain gauges while the model simulations are from the three different intializations.

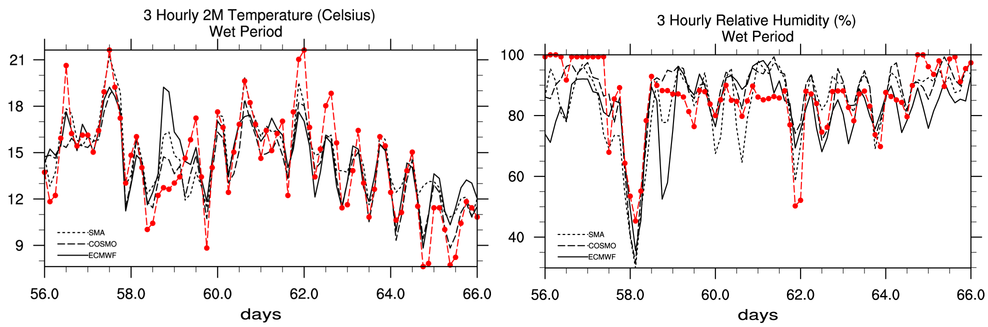

Figure 5: Same as figure 4 but for the wet period

The 'wet period' is characterised by smaller biases, with the exception of day 59 when all the three model simulations missed completly the observed precipitation. It is worth nothing that in this wet regime when the soil moisture is close to its field capacity value the SMA experiment produces unrealistic warm increments. This is a side effect produced by the missing strong coupling between the soil and the boundary atmospheic level. Indeed care has to be taken regarding the applicability of a soil moisture scheme when the information content at screen level is weak. Some thinning is therefore recommended to exclude synoptic situations with weak coupling between soil and atmosphere and when horizontal coupling between neighbour grid points is weak (cloud free, not too strong advection).

Biases of up to -4 K in the T_{2M} and 20 % in the RH_{2M} highlight problems in the estimations of both turbulent surface fluxes which can be due both to ground temperature and humidity estimations and/or wrong surface turbulent coefficients. Figure 6 shows the mean-day sensible and latent heat fluxes at one of the CARBOEUROPE station taken as example averaged over 10 days during the dry and wet periods identified. Since the other sites show very similar results they have not been included. On average both sensible and latent heat fluxes are always underestiamted (see also figure 8), nevertheless, during nightime there is a substantial over-estimation of both turbulet fluxes. The nightime bias is expecially marked in the ECMWF experiment as was diagnosted by the excess in the outgoing longwave emission of figure 2. The soil–atmosphere interface is too warm and prevents the formation of nightime stratified stable boundary layer conditions.

The diurnal cycle, almost completly absent in the ECMWF experiment, is highly improved by both the COSMO and SMA experiments, showing the role played in turn by the ground temperature and humidity initialization. Moreover this highlights the main danger of external interpolation from global models as a strategy for surface initialization. TERRA in its present implementation is very conductive, so that, deep levels heating is conveyed to upper layers very efficiently, while IFS SVAT scheme is tuned to a much lower conductivity. When the interpolation is performed the initial ground temperature profile given to TERRA is therefore not optimal for the new scheme which then predict a completly unrealistic cycle of the diurnal cycle. As an example, figure 7 shows the daily variation of the ground temperature at two levels as predicted by the three assimilation cycles at Collelongo during the dry period. Despite the fact that SMA and COSMO have a more pronounced diurnal cycle the most stricking feature is the very high temperature predicted by the ECMWF experiment in the deeper ground levels. The use of this value into the TERRA scheme probably causes the unrealistic noctournal heating diagnosted in figure 8. Most of the improvements are achieved when passing from the ECMWF experiment to the COSMO one while the SMA initialization only adds a marginal benefits to the prediction of surface fluxes. This also suggests that a correction of soil temperature is more relevant then the subsequent correction of soil moisture at least in dry condition. In other words, when the soil is close to its wilting point it is hard to estimate the dominating effect between thermal inertia and radiative cooling and possibly simply running the forecast model can furnish the zero-order correction to the soil initialization problem. Near surface variable biases are strongly dependent on the soil conditions. Therefore schemes which for their design only correct for errrors on a selective basis can therefore only be able to 'conditionally' correct them.

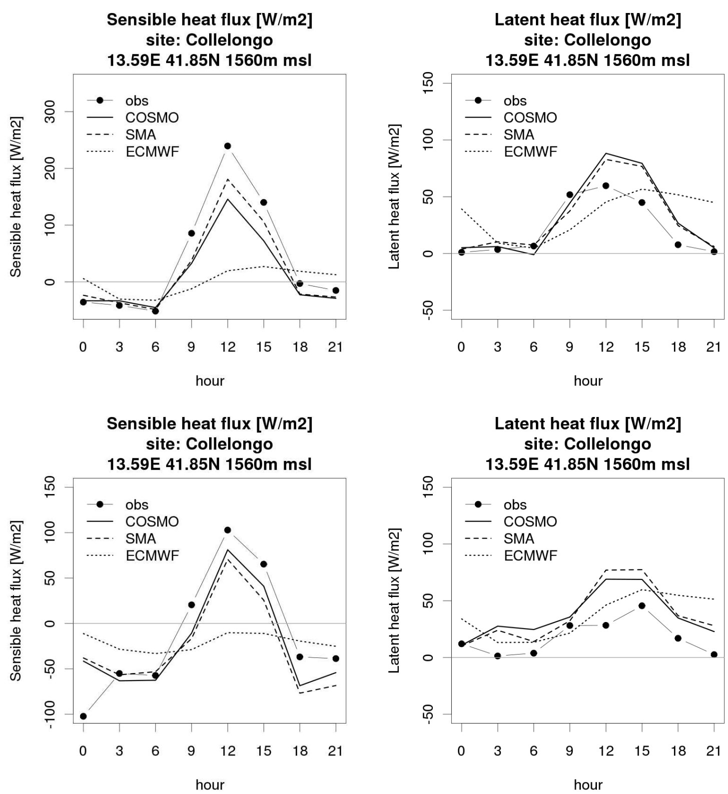

Figure 6: Top panel.Comparison of model and observed meanday sensible and latente heat fluxes for the dry period under study. Low panel. as on the top panel but for the wet period. Similar results have been found in the other CARBOEUROPE sites (not shown)

Keeping these caveats in mind it is nevertheless important to assess the global statistical performance of the various experiments in terms of forecast scores. Figure 8 shows the comparison between H and L_E at two CARBOEUROPE locations for the three methods as

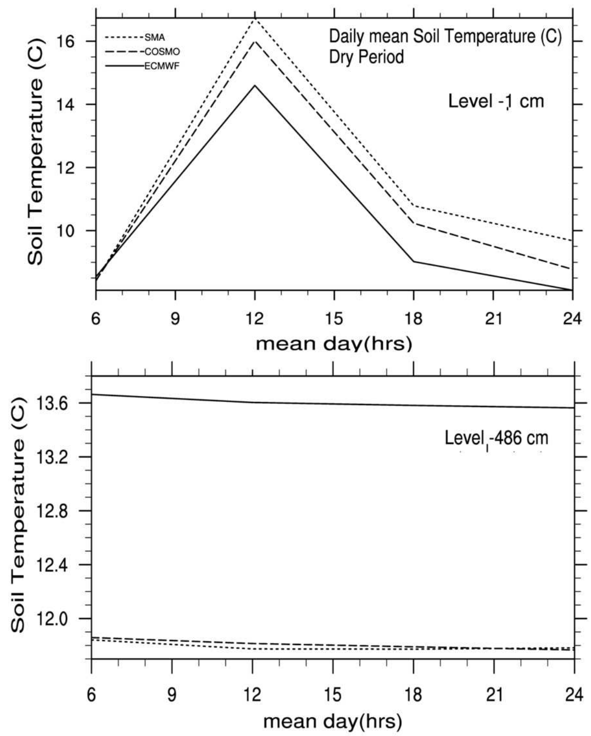

Figure 7: Mean day temperature profiles at two model levels as predicted by the three initialization scheme.

compared to the observations for the whole period. The fit accross the data is performed locally. That is, for the fit at given point x, the fit is made using points in a neighbourhood of x, weighted by their distance from x following [9]. These diagnostics are calculated for the whole period so different soil condition are sampled. On average the model underestimates both sensible and latent heat during daytime and nighttime. It is clear that even on domain mean statistics the improvements produced by the COSMO experiment with respecty to ECMWF interpolation largely offset the addictional benefit of also performing a soil moisture analysis. Similar conclusions can be drawn if looking at 2m diagnostics evaluated using the synop network over the whole COSMO-I7 domain and reported in figure 9. Most of the bias contribution is due to the cold bias at noon which is reduced by both the COSMO and SMA experiments. The nightime warm bias, even if smaller in size, is nevertheless very significative from the point of view of weather inpact. It is likely infact that these biases cause the missing prediction of local weather phenomena such as fog and brine formation.

4 Conclusions

Given the lack of any representative soil measurement network and the often insufficient knowledge of surface pedology, lithology, and vegetation characteristics, at the present soil analysis should be considered simply as a *tuned* lower boundary condition to drive at its best lower level atmospheric processes. The first and more obvious consequence of this strong assertion is that soil outputs from atmospheric models are not appropriate to drive for example hydrological models, as absolute soil moisture content strongly depends on the design of the soil model [6]. Onces this is given for acquired, there are a number of practical considerations which directly stems from this acknowledgment. They have been proved along this work in which different soil initialization methods have been compared in the quest for the best strategy to provide a soil analysis in regional models. They main findings are now

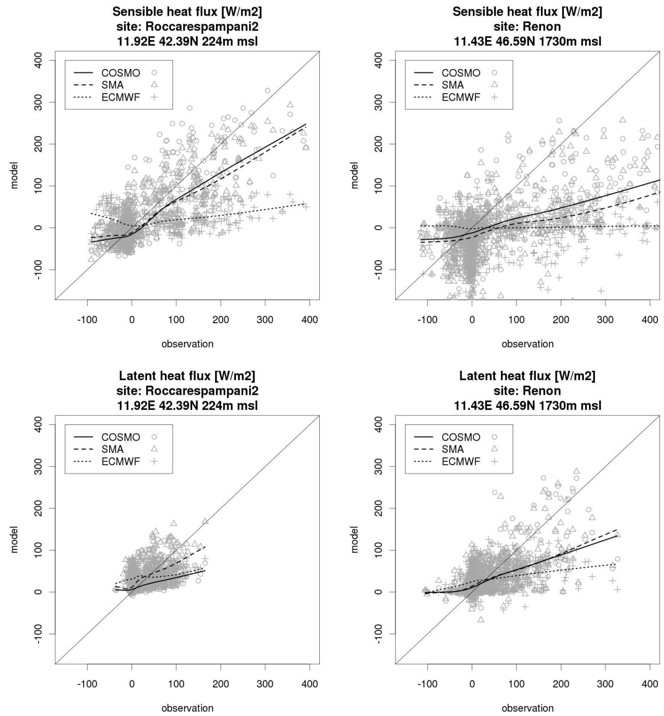

Figure 8: SON 2008 period statistics for the latent and sensible heat fluxes at two Carboeurope locations.

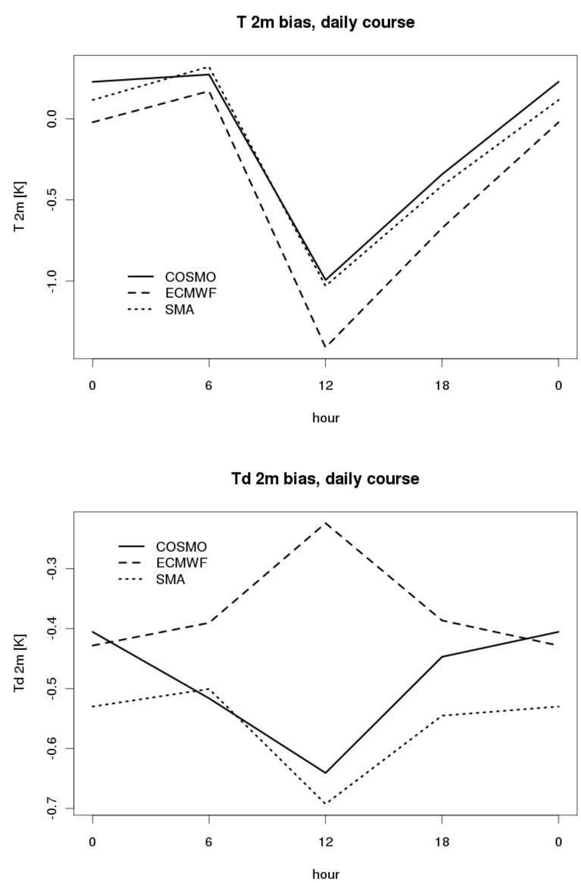

Figure 9: Global domain statistics of the T_{2m} variable as predicted by the three experiments. The bias is calculated using the 400 stations of the synop network.

synthesized in this conclusive section.

Firstly, there are serious problems in trying to use soil analysis derived from a global model into a limited area model if the two models are different. While this is certainly a suitable option for the atmospheric fields which to some extend represent the true atmospheric state it looses any validity for the soil prognostic variables if, as it is at the present, they only represents parameters to be tuned to compensate for various model biases. It is clear that SVAT models with different characteristics will also adjust to different thermal and hydrological equilibria with little connection to the reality. If the global model and the regional one have varying assumptions, the consequences on the surface fluxes estimation can be severe especially under selective circumstances (i.e. dry condition, little advection, large cloud cover, etc). In our study we found, for example, that initializing the regional model COSMO SVAT moudule TERRA by interpolation from the global IFS model induce in COSMO a strong warn nighttime bias and a weakening of the diurnal cycle in both latent and sensible heat surface fluxes. The cause was identified in the different specification of the soil thermal conductivity between the two models. What therefore could be appropriate (.i.e. 'tuned') for IFS is probably not optimal when used into another model.

Simply using COSMO in a freely running configuration can avoid these imbalances and it is found a winning and therefore recommended strategy especially for situation when the soil is close to its wilting point. This condition are particularly challenging since higher amplitudes in soil heating during daytime and cooling during night are expected. The correct prediction of the soil vertical temperature profile becomes then fundamental. Soil temperatures profiles which are in balance with the soil scheme are the zero order factor for correct surface flux estimations. Any subsequent improvement in the soil moisture estimation performed, for example, using indirect measurements such as T_{2m} only adds a marginal benefit. This apparently striking result is justified by the design of current soil mositure schemes which, using near surface observations, as predictors for soil moisture increments, assume that atmosphere is informative about soil moisture. However, forecast errors of atmospheric temperature and humidity do not always contain useful information. For instance, during rain, at nighttime, and with low solar insulation, this method is likely to fail. In the COSMO implementation the soil moisture correction is evaluated at two instants around noon when the soil-atmosphere coupling is supposed maximum. The major benefit from the soil moisture analysis arises therefore primarily for situations the scheme is designed for i.e. correcting forecast errors at the time the observations are assimilated which is around noon. In situation in which the bias does change its sign during the day, it is intuitive that the scheme can dangerously act to exacerbate the bias already present. A possible, and already proposed solution [2] would be a selective application of soil moisture increments only on those cases for which the underline hypothesis are stickily verified. This is nevertheless again an 'ad hoc' solution which doesn't help envisage a substantial improvement of the absolute quality of soil analysis.

The use of other observations such precipitation, satellite derived surface soil moisture can help on future soil moisture analysis. Nevertheless it is clear from this study that a substantial benefit can immediately arise from including temperature as a control variable in the assimilation scheme and from a concreat refinement of the model itself as was also outiled by the intercomparison work done by [3].

Acknowledgment We are in debt with Martin Lange for providing the soil moisture analysis scheme and a series of usufull comments which helped clarifying the scope of the paper. Riccardo Valentini (University of Tuscia, Viterbo), Giorgio Matteucci e Vincenzo Magliulo (CNR ISAFoM) are thanked for providing the data from CARBOEUROPE sites. This work is part of the activities of ARPA-SIMC funded by the Italian National Department for Civil Protection (Protezione Civile Nazionale, Roma).

References

[1] Douville, H., P. Viterbo, J. Mahfouf, and A. Beljaars, 2000: Evaluation of the optimum interpolation and nudging techniques for soil moisture analysis using FIFE data. *Monthly Weather Review*, **128 (6)**, 1733–1756.

[2] Hess, R., M. Lange, and W. Wergen, 2008: Evaluation of the variational soil moisture assimilation scheme at Deutscher Wetterdienst. *Quarterly Journal of the Royal Meteorological Society*, **134 (635)**.

[3] Jacobs, C., et al., 2008: Evaluation of European Land Data Assimilation System (ELDAS) products using in situ observations. *Tellus A*, **60 (5)**, 1023–1037.

[4] Mahfouf, J. F., 1991: Analysis of Soil Moisture from Near-Surface Parameters: A Feasibility Study. *Journal of Applied Meteorology*, **30 (11)**, 1534–1547.

[5] Robock, A., K. Vinnikov, G. Srinivasan, J. Entin, S. Hollinger, N. Speranskaya, S. Liu, and A. Namkhai, 2000: The global soil moisture data bank. *Bulletin of the American Meteorological Society*, **81 (6)**, 1281–1299.

[6] Teuling, A., R. Uijlenhoet, B. van den Hurk, and S. Seneviratne, 2009: Parameter Sensitivity in LSMs: An Analysis Using Stochastic Soil Moisture Models and ELDAS Soil Parameters. *Journal of Hydrometeorology*, **10 (3)**, 751–765.

[7] Viterbo, P. and A. Beljaars, 1995: An Improved Land Surface Parameterization Scheme in the ECMWF Model and Its Validation. *Journal of Climate*, **8 (11)**, 2716–2748.

[8] Western, A., G. Bl
"oschl, and R. Grayson, 1998: Geostatistical characterisation of soil moisture patterns in the Tarrawarra catchment. *Journal of Hydrology*, **205 (1-2)**, 20–37.

[9] Cleveland, W., E. Grosse, W. Shyu, J. Chambers, and T. Hastie, 1991: Statistical models in S. *Wadsworth and Brooks/Cole, Pacific Grove, Ch. Local regression models*, 309–376.

[10] Lange, M., 2009: Parametrisation of the sensitivity $dT2m/dw$ in soil moisture analysis. Tech. Rep. -, Deutscher Wetterdienst, available at Deutscher Wetterdienst Frankfurter Str. 135 63067 Offenbach Germany.

An Empirical Radar Data Quality Function for LHN: Experiments with COSMO-2

Andrea Rossa[1], Franco Laudanna del Guerra[1] and Daniel Leuenberger[2]

1 ARPA Veneto, Teolo, Italy
2 MeteoSwiss, Zurich, Switzerland

1 Introduction

The meteorological and hydrological modelling communities are increasingly using radar observations and place specific demands on the description of the corresponding data quality. A recent concerted effort has been the COST 717 Action Use of radar observations in hydrological and NWP model [13]. Several approaches have been proposed based on how significant the radar data quality control algorithms impact the observations [6, 5, 16]. One element which can be considered common to all these efforts is that a detailed knowledge of the radar systems is a prerequisite to derive an error information, whereas some methods rely on extra information from complementary observations, such as disdrometers [1] or a high-resolution rain gauge network [7], for instance, which makes the task more demanding.

The fact that many NWP centres have recently taken into operations convection-permitting forecast models, many of which assimilate radar data, there is the need for a pragmatic approach to providing quality information in order to avoid that radar errors degrade the model's initial conditions and, therefore, its forecasts [14]. Such pragmatic approaches have been applied and can be as simple as parametrizing the radar data quality with range [10].

In this contribution a pragmatic and empirical approach to deriving a radar data quality description is proposed to be used in radar data assimilation, more specifically for the latent heat nudging (LHN) scheme [12]. In section 2 the data sets, the NWP, and two cases are briefly described, while section 3 is devoted to the formulation of the quality function. Results will be shown and discussed in section 4, and conclusions given in the final section.

2 Data sets, NWP model, and cases

Radar data The Swiss Radar Network [7] consists of three C-band Doppler radars providing full volume information every five minutes. The data are preprocessed and available on a cartesian grid with a mesh size of $2 \times 2\,km^3$ for the network composite.

The Veneto Radar Network (VRN) consists of two EEC single polarization C-band Doppler radars, one located on Mt. Grande a 470 m hill top 25 km southwest of the city of Padova, one at sea level close to the border between Veneto and Friuli in northeast Italy. Their data are post processed by the Hydrometeorological Decision Support System [2]. Here a number of quality control algorithms are applied and surface QPE is derived in the QPE-SUMS algorithm [9]. The QPE is available every 10 minutes.

The COSMO NWP model COSMO-2 is the operational MeteoSwiss implementation of the high-resolution version of the non-hydrostatic weather forecasting model of the COSMO (Consortium for small-scale modelling) community presently operational at several European

Weather Services (Doms and Schattler, 2002, Steppeler et al., 2003). The COSMO-2 model domain covers the Alpine arch (520 x 350 grid points, 60 vertical levels) and uses a horizontal mesh size of 2.2 km. Its forecasts are driven by the regional COSMO-7 model with 6.6km mesh size and covering central Europe, which in turn is nested in the global IFS model of ECMWF. The COSMO-2 model uses a data assimilation system based on a nudging technique (Schraff, 1997) for conventional observations from surface stations, radiosondes, aircrafts and wind profiler.

Radar rainfall assimilation Radar surface rainfall observations are assimilated by the Latent Heat Nudging scheme [10]. The main principle of LHN is to correct the model's latent heating at each time step by a factor derived from the ratio of observed and model-estimated surface precipitation based on the basic assumption that the vertically integrated latent heating is proportional to the surface rain rate. This is accomplished by adding an extra term to the prognostic temperature equation, resulting in a gradual adjustment of the other fields according to the full, nonlinear model. The introduced change in buoyancy provokes an enhancement or dampening of the vertical velocity and the associated cloud and precipitation processes. The vertical shape of the applied forcing is taken from the model latent heating, ensuring consistency with the microphysical parametrisation. At each grid point with non-zero temperature increments, the specific humidity is also adjusted such that the relative humidity is conserved. Latent Heat Nudging has proven to work well in the kilometre-scale COSMO model for idealized and real convection cases [11]. When precipitation is treated as a prognostic model variable and is advected in all three space dimensions, a basic assumption of the LHN scheme is violated. [15] proposed a modified LHN scheme to take into account the spatial and temporal separation of the rate of change in latent heating and surface precipitation and make the LHN algorithm more compatible with the prognostic precipitation scheme of the COSMO model. This improved LHN scheme is part of the operational implementation of COSMO-2 and used for all experiments presented in this study.

Case studies In this section a brief description of the cases is given along with the impact of the LHN on the analysis, in order to be able to assess the impact of the quality function on the LHN analyses.

Veneto case 26 September 2007 This rainfall event was exceptional in terms of rainfall intensities and accumulations (up to $120\,mm$ in 1 hour, $90\,mm$ in $30\,min$, and $24\,mm$ in $5\,min$), and overall accumulation $320\,mm$ in $6\,h$ and caused flooding of the urbanized area of Venice Mestre. A surface low located on the Gulf of Genoa was associated with an upper-level trough which advected cold air from Northern Europe towards the Alps and subsequently onto Veneto, giving rise to organized convective activity.

The COSMO-2 analysis cycle confirms the heavy precipitation but with incorrect timing and extension (Fig.3). A first of two passages took place in the morning hours and hit a much larger area. In the late afternoon the second passage brought even larger intensities over the region. The analysis cycle produced a local precipitation maximum which is quite close to the observed but, on top of that, a number of even stronger and larger maxima were simulated which were not observed (e.g. just east of Mestre over the coast line, and some $50\,km$ northwest of Mestre).

Figure 3 panel b) shows that the latent heat nudging (LHN) of the Veneto radar data managed to reduce the incorrect precipitation to a large extent, for instance reducing values

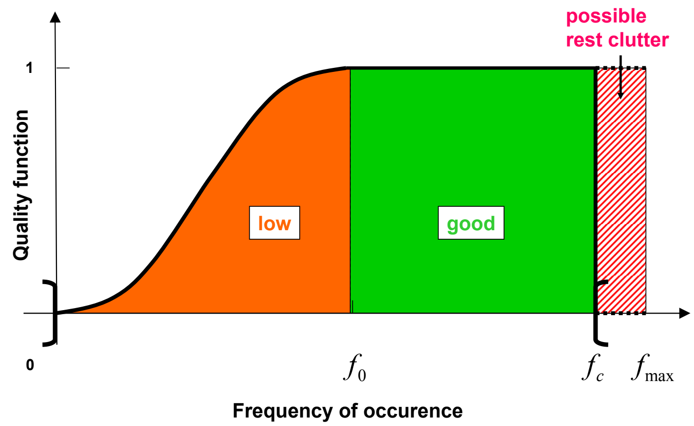

Figure 1: Conceptual definition of the radar data quality function. Rest clutter identification is performed on the very high-frequency pixels, which then are set to zero. Pixels with frequency higher than f_0 are set to one, while the quality is lowered for frequencies below f_0. See text for further explanations.

of more than $100\,mm$ in the the area northwest of Mestre to under $40\,mm$ ($20\,mm$) for the greenish (blueish) colors, values that are in line with the rain gauge measurements (not shown). The highest accumulations simulated just to the east of Mestre were almost entirely suppressed in the LHN run. On the other hand, it successfully triggers the precipitation in the area where it was observed with about the right accumulation.

In summary, the LHN has a very large impact on the simulation in analysis mode featuring a very efficient drying of the excess precipitation and excellent triggering of the observed convection. There is a clear response of the low-level wind and convergence field illustrating that the LHN method is able to modify the microscale circulation around the precipitation systems.

Swiss case 11 August 2008 The case studied over the SRN domain is a less exceptional case of the passage of several frontal rain bands over Switzerland. On 11 August 2008 an extensive long wave trough was situated over Western Europe. An associated low pressure system over the Brithish Isles with a core of 990 hPa was associated to a warm and a cold frontal passage in central Europe on that and the following day. On 11 August in the afternoon, a first rainband associated with the warm front crossed Switzerland, causing up to 18 mm of precipitation. In the night the coldfront entered the SRN domain from west and passed slowly over Switzerland during the 12 August. This coldfront led to heavy frontal and convective rainfall with sums up to 70 mm in northern Switzerland.

In this case, the overall effect of the LHN was to insert the main convective activity observed over northern Switzerland, along with a significant drying over the main Alpine crest in central Switzerland, where evident convective activity was suppressed (Fig. 4 panels a and b). Even on the minor precipitation peaks the LHN managed to improve the precipitation analysis.

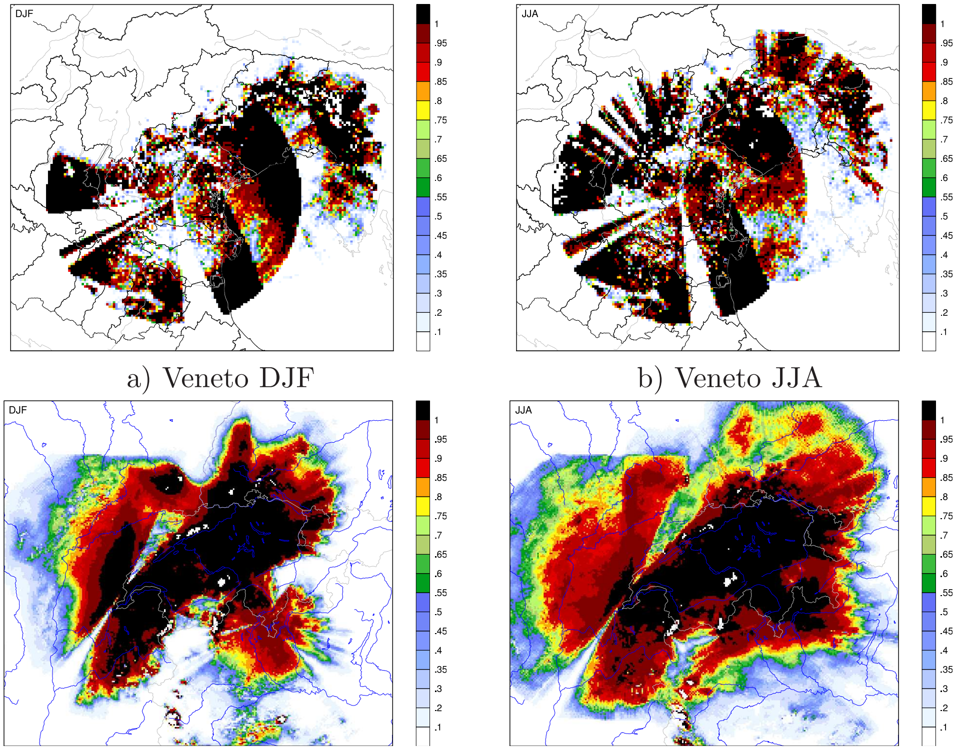

a) Veneto DJF b) Veneto JJA

a) Swiss DJF b) Swiss JJA

Figure 2: Radar data quality function for VRN and SRN for winter and summer period.

3 Empirical radar data quality function

Simple, economical schemes for cloud-scale radar data assimilation, one of which is Latent Heat Nudging (LHN), have recently received considerable attention for deployment in rapid update cycles, and were reported to produce beneficial results [4, 3]. There is, however, no explicit accounting of the observation quality in LHN, a fact which makes the scheme vulnerable, for instance to non-rain echoes which may be significantly amplified in convectively unstable environments [14].

Another typical situation which can lead to problems in the assimilation cycle are areas in which the radar has a greatly reduced visibility or is 'blind'. Suppose that the model has precipitation in an area which are badly seen by the radar. Without accounting for this reduced radar quality the LHN scheme tries to reduce or suppress the model precipitation by cooling the profile, which can induce subsidence. If this happens close to a boundary of the radar domain such a subsidence can act to produce an outflow boundary which, in turn, can create a low-level convergence able to trigger precipitation.

Motivated by [8] who pointed out the structural similarity of the long-term radar QPE accumulation with the visibility map of the radar, an empirical radar data quality function is proposed here based on a long-term frequency analysis of precipitation occurrence f, which counts for each radar pixel the number of times when precipitation is observed. The main idea is to attribute quality to these pixels as follows (Fig. 1):

- pixels which are seen too many times are likely to be rest clutter and are assigned $w(x, y) = 0$ for $f \geq f_c$;
- pixels which are regularly seen are likely to be of sufficient quality to be taken verbatim, i.e. $w(x, y) = 1$ for $f_0 \leq f \leq f_c$;

- pixels which are rarely seen are likely to be in blocked areas and are assigned $w(x, y) = g(f) \to 0$ for $f \to 0$;

The lag correlation of the time series for each pixel is found to discriminate clutter pixels from rain pixels, in that the decorrelation length is shorter for the former. This is used to identify plausible values of f_c. The function $g(f) = 1 - 1/(1 + e^{0.7f-4})$ is chosen such as to provide a smooth transition between the good and the still acceptable pixels.

In the perspective of updating such an analysis by adding the latest day while taking out the oldest in the data set, the length of the period should be long enough to avoid too large day-by-day variability, while it should be short enough to allow for at least seasonal differences. One-month periods proved to be rather short, while three-month periods seem more adequate. Figure 1 upper panels shows the results for the summer and the winter seasons for the Swiss radar network. It can be easily seen that the main and well known error prone areas are reproduced by the quality function, i.e. the scarse visibility in the valleys like the Valais and the Engadin, the cones due to nearby obstacles of the La Dole radar, the range effect in all three radars, as well as a number of small scale clutter-prone areas.

The seasonal variability is also plausible in that in summer the precipitation systems are higher-reaching than in winter so that they are seen at longer ranges in summer yielding better quality. In particular, in winter the quality at long ranges is reduced, the orographic blocking as well as the cone of the La Dole radar extending to the northeastmuch much more pronounced. The rest clutter pixels (white wholes) are remarkably stable and tend to be larger in winter than in summer.

For the Veneto radar network (Fig. 1 lower panels) the cones due to two closeby hill peaks are well visible in the quality function, as are the shielded areas behind the pre-Alpine chain to the north. The range effect, however, is inverted especially for the Mt. Grande radar, showing good quality at longer and reduced quality in large patches at shorter ranges. The lower quality regions close to the radar occur mostly over completely flat terrain and still require explanation. Also, there is a significant difference between the two radars of the network, with the Concordia Sagittaria radar exhibiting a frequency of occurrence which is significantly lower than for the Mt. Grande radar. This fact is unlikely to depend on differences in the precipitation climatology but is expression of differences in the performance of the two radars.

The seasonal differences are well in line with those found for the SRN. Most evident features include the longer ranges over the mountains to the north. Again, the maximum quality is found out to the border of the radar domain in summer.

4 Impact of the quality function on radar data assimilation

In order to assess the impact of the quality function on the LHN scheme assimilation experiments were run as listed in Tab. 1. In the following two subsections this impact is described for the cases presented in Section 3.

Veneto case 26 September 2007 The main impact of the quality function in experiment REF_RQ as compared to REF_R is the reduced dipolar structure at the western border (Fig. 3

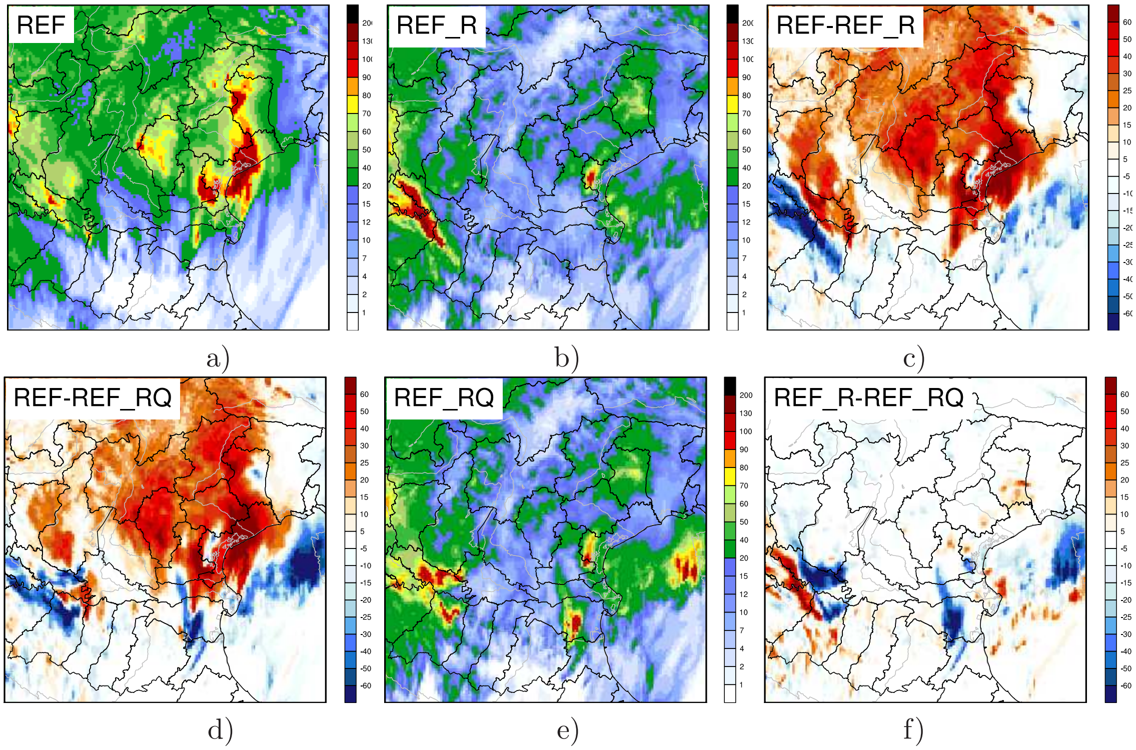

Figure 3: 24-hour precipitation accumulation (in mm) of the Veneto case 26 September 2007 00 UTC simulations as listed in Table 1 (panels a, b, and e), as well as the corresponding differences (panels c, d, and f). The arrangement of the panels has been chosen to help the comparison of the accumulation and their differences.

experiment	description	Swiss case	Veneto case
REF	without LHN	48h analysis	24h analysis
REF_R	with LHN, without quality function	starting	starting
REF_RQ	with LHN, with quality function	11 Aug 2008 00UTC	26 Sep 2007 00UTC

Table 1: Assimilation experiments for the assessment of the impact of the radar data quality function on the LHN scheme.

panels d and f) of the radar domain and, most prominently, the differences in the blind cones of the Mt. Grande radar. In fact, here the quality function allows for the model precipitation to stay in the simulation. More subtly, and due to the fact that the quality function of the Veneto radar network is one in this area, the cone constitutes a border between the areas where the radar is assigned zero and full quality. In this case, the erroneous model rainfall is suppressed by inducing subsidence, but not in the cone, so that the resulting low-level outflow produces a convergence and, therefore, enhanced rainfall. This effect is evident in the difference plots REF - REF_RQ and REF_R - REF_RQ (Fig. 3 panels c and f).

Swiss case 11 August 2008 The most evident feature of the LHN run REF_R for this case is the artificially looking structure in the southwestern border of the SRN domain (Fig. 4. Infact, the SRN quality is close to zero in this area due to a visibility cone of the La Dole radar and a progressive range effect. The model analysis simulated significant precipitation in this area which the LHN sucessfully reduced. Just outside the SRN domain, on the other hand, there are precipitation bands along the border. Again, these are compatible with the mechanism discussed above. The quality function recognizes this as an area in which the radar data should not have a strong impact on the model. Accordingly, the run with the quality function REF_RQ strongly reduces the artifacts, both within the radar domain and

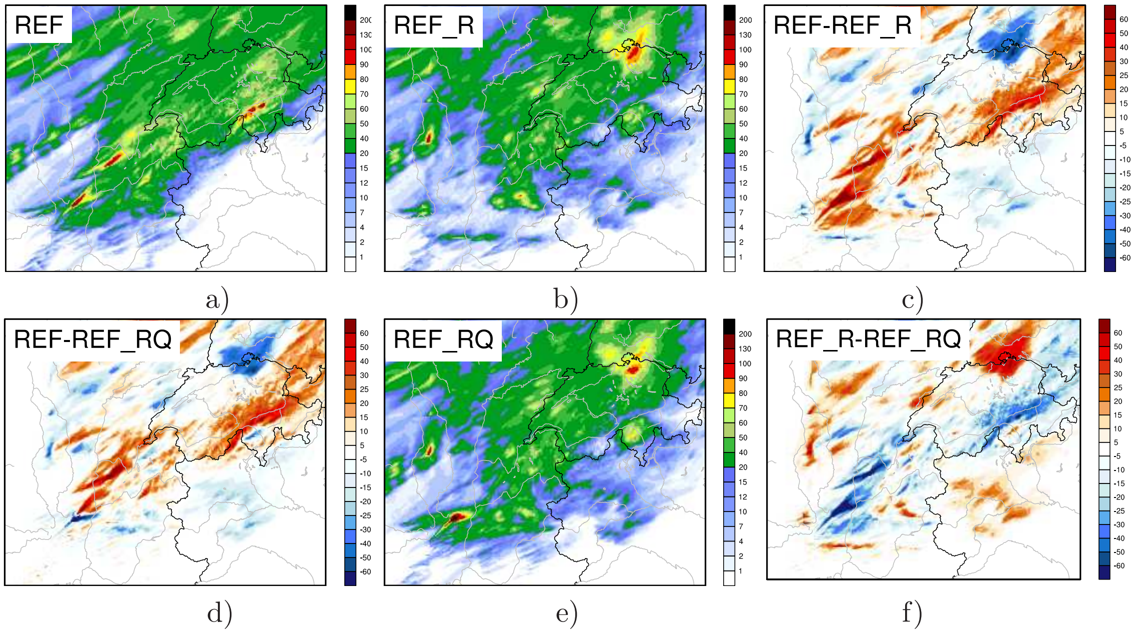

Figure 4: As in Fig. 3 but for the Swiss case 11 August 2008 and 48-hours accumulation period.

just across its border. On the rest of the SRN domain the quality function has a minor impact on the LHN scheme, as the model did not produce precipitation in areas of low radar data quality.

5 Summary and discussion

In this contribution a novel, yet simple, empirical quality description of radar-derived quantititive precipitation estimates (QPE) was proposed. It was constructed using a long-term frequency of occurrence of precipitation analysis. Hereby frequent (rare) occurrence of precipitation is assessed as 'good' ('bad') quality, while rest clutter was identified and assigned quality zero. How and for what frequencies the quality descreases from one to zero is tunable to some extent, and can be conceived as an overall weight one subjectively intends to assign to the radar observation. The empirical radar data quality function proposed with a moving 90-day accumulation window has the following characteristics:

- it is conceptually simple and easy to construct;
- it reproduces the main error structures and is, therefore, a plausible way to account for the average problems in radar QPE;
- it has a sufficiently smooth day-to-day evolution for an Alpine climate;
- it accounts for the seasonal variability of the radar QPE;
- it is, to some extent, generic, in that it can 'easily' be evaluated for different radar networks (here for two) and, potentially, also for heterogeneous networks in that it does not rely on specifics of the radar processing.

The impact of the proposed quality function on the LHN assimilation has been found to be beneficial in that it:

- reduces artifacts which can be induced close to boundaries of the radar domain;

- constitutes an additional means to reduce rest clutter and its potentially harmful impact on the analysis;
- does not artificially interfere with the model precipitation in areas where the radar is (almost) blind;

The limitations of such an empirical radar data quality description are recognized in that:

- it is empirical and not physically based and does, therefore, describe the effects of the error sources without taking them into account explicitly;
- it is an average, rather than a instantaneous quality description and thus accounts for average errors, rather than actual real time errors;
- the present formulation will yield good (bad) quality in case of precipitation occurrence much higher (lower) than climatology, hence not reflecting effective radar data quality;
- the quality is described as a weight between 0 and 1, i.e. an index, rather than in units of the precipitation and is, therefore, not directly applicable to statistical data assimilation schemes as ensemble Kalman filters, for instance, nor does it, in its present form, account for error covariances.

In a radar network single radars may be missing occasionally, or for longer periods, a fact which is not easily accounted for in the presented approach. A solution to this problem could be performing the analysis on the single radars and then composited following the compositing procedure of the network. Alternatively, the quality information thus obtained could be used in support of the compositing method, preferring the radar with the best quality for a given pixel.

An obvious extention of this work is to apply the quality function to longer assimilation periods and assess its impact more systematically. Also, its impact on the free forecasts has yet to be addressed. In view of the OPERA efforts to make radar data available on a European scale this approach could be a candidate method to pragmatically deal with the inevitably very heterogeneous radar data quality in the framework of assimilation methods like LHN.

References

[1] Berenguer, M., and I. Zawadzki, 2008: A Study of the Error Covariance Matrix of Radar Rainfall Estimates in Stratiform Rain. *Weather and Forecasting*, **23**, 1085–1101.

[2] Conway, J. W., C. Barerre, G. Formentini, L. Lago, A. Rossa, and M. Calza, 2007: Flash Flood Prediction in Italy: Development and Testing of a New Capability. *Proceedings of 21st Conference on Hydrology*, AMS, AMS Annual.

[3] Dixon, M., Z. Li, H. Lean, N. Roberts, and S. Ballard, 2009: Impact of Data Assimilation on Forecasting Convection over the United Kingdom Using a High-Resolution Version of the Met Office Unified Model. *Monthly Weather Review*, **137**, 1562–1584.

[4] Ducrocq, V., D. Ricard, J.-P. Lafore, and F. Orain, 2002: Storm-Scale Numerical Rainfall Prediction for Five Precipitating Events over France: On the Importance of the Initial Humidity Field. *Weather and Forecasting*, **17**, 1236–1256.

[5] Fornasiero, A., P. P. Alberoni, R. Amorati, and C. Marsigli, 2006: Improving the radar data mosaicking procedure by means of a quality descriptor. *ERAD Publication Series*, Vol. 3, 378–341.

[6] Friedrich, K., M. Hagen, and T. Einfalt, 2006: A Quality Control Concept for Radar Reflectivity, Polarimetric Parameters, and Doppler Velocity. *Journal of Atmospheric and Oceanic Technology*, **23**, 865–887.

[7] Germann, U., G. Galli, M. Boscacci, and M. Bolliger, 2006: Radar precipitation measurement in a mountainous region. *Quarterly Journal of the Royal Meteorological Society*, **132**, 1669–1692.

[8] Germann, U., and J. Joss, 2004: Weather Radar: Principles and Advanced Applications', edited by P. Meischner in Springer monograph series 'Physics of Earth and Space Environment'.

[9] Gourley, J., J. Zhang, R. A. Maddox, C. M. Calvert, and K. Howard, 2001: A real-time precipitation monitoring algorithm - Quantitative Precipitation Estimation and Segregation Using Multiple Sensors (QPE-SUMS). *Preprints, Symp. On Precipitation Extremes: Predictions, Impacts, and Responses.*, AMS, AMS, 57–60. [Albuquerque, NM].

[10] Jones, C. D., and B. Macpherson, 1997: A latent heat nudging scheme for the assimilation of precipitation data into an operational mesoscale model. *Meteorol. Appl.*, **4**, 269–277.

[11] Leuenberger, D., and A. Rossa, 2007: Revisiting the latent heat nudging scheme for the rainfall assimilation of a simulated convective storm. *Meteorology and Atmospheric Physics*, **98**, 195–215.

[12] Manobianco, J., S. Koch, V. M. Karyampudi, and A. J. Negri, 1994: The impact of assimilating satellite-derived precipitation rates on numerical simulations of the ERICA IOP-4 cyclone. *Mon. Wea. Rev.*, **122**, 341–365.

[13] Rossa, A., M. Bruen, D. Fruehwald, B. Macpherson, I. Holleman, D. Michelson, and S. Michaelides, 2005: *COST 717 Action – Use of Radar Observation in Hydrology and NWP Models*. Vol. EUR 21954, *COST Meteorology*, COST, 286 pp.

[14] Rossa, A. M., and D. Leuenberger, 2008: Sensitivity of the LHN scheme to non-rain echoes. *Meteorological Applications*, **15**, 503–511.

[15] Stephan, K., S. Klink, and C. Schraff, 2008: Assimilation of radar-derived rain rates into the convective-scale model COSMO-DE at DWD. *Quarterly Journal of the Royal Meteorological Society*, **134**, 1315–1326.

[16] Szturc, J., K. Osrodka, A. Jurczyk, and L. Jelonek, 2008: Concept of dealing with uncertainty in radar-based data for hydrological purpose. *Natural Hazards and Earth System Sciences*, **8(2)**, 267–279.

Is the Local Ensemble Transform Kalman Filter suitable for operational data assimilation?

Mikhail Tsyrulnikov

Hydrometcentre of Russia, Moscow, Russia

Abstract

Principal approximations inherent in the Local Ensemble Transform Kalman Filter (LETKF) are examined, and conclusions about the related approximation errors are drawn. First, the major difficulty in implementing the LETKF technique in the operational context is its lack of efficiency in assimilation of non-local, primarily satellite, observations. The cause of this difficulty is the restriction of the analysis increment to low-dimensional ensemble space, on the one hand, and large spatial supports of satellite data, on the other hand. Second, making analysis in small local boxes gives rise to small-scale noise due to local data selection—as in Optimum Interpolation. Third, an attempt to account for realistically correlated observational errors makes LETKF and other ensemble-space and model-space Ensemble Kalman Filters (EnKF) computationally inefficient. Published experimental results are discussed in the light of the theoretical and experimental findings made in this study.

1 Introduction

In the recent years, a kind of Ensemble Kalman Filter (EnKF), the Local Ensemble (Transform) Kalman Filter (LEKF/LETKF) has become popular. Numerous papers, starting from (Ott *et al.* 2004), have explored capabilities of LETKF to deal with different data assimilation issues, including real-data assimilation (Hunt *et al.* 2007, Szunyogh *et al.* 2007b, Miyoshi and Yamane 2007, Bonavita *et al.* 2008), satellite data assimilation (Szunyogh 2007a, Fertig *et al.* 2007), four-dimensional assimilation (4D-LETKF, Hunt *et al.* 2004, Kalnay *et al.* 2007, Harlim and Hunt 2007b), non-Gaussian background-error distributions (Harlim and Hunt 2007a), forecast bias (Baek *et al.* 2006) and others. The LETKF technique is simple, computationally efficient, and allows for flow-dependent background-error covariances. Different extensions to the basic LETKF formulation have been proposed. Some of the above papers report on promising results in near-operational setting. But still there are no operational implementations.

The questions arise: Is the LETKF technique a real alternative to variational methods (3D-Var and 4D-Var) as a means of operational (global and limited-area) data assimilation? What are the conditions under which LETKF can be considered to be really competitive?

To answer these questions, we consider below the details of the LETKF algorithm and draw some conclusions about its capabilities, especially in the areas of satellite and meso-scale data assimilation. The focus is on the *analysis* step, where, as we will see below, the major limitations of the technique lie.

2 LETKF. Analysis step: brief description

In this section, we derive the LETKF analysis equations, emphasizing approximations (and thus imperfections) inherent in this technique.

At each analysis step, we have: the deterministic forecast $\mathbf{x}^f$, an ensemble of perturbed forecasts $\{\mathbf{x}_i^f\}$ ($i = 1, \ldots, n_e$, n_e is the ensemble size), and observations $\mathbf{x}^o$. The ensemble mean is usually used as a background field $\mathbf{x}^b$ in the analysis. The deviation fields $\mathbf{x}_i^f - \mathbf{x}^b$ are deemed to be independent samples from the unknown true probability distribution of the (minus) *background error* $\mathbf{x}^b - \mathbf{x}$, where $\mathbf{x}$ is the true field to be estimated. Here, we assume that $\mathbf{x}_i^f$ are already undergone a procedure like 'variance inflation', which attempts to take into account errors due to forecast model imperfections (model errors).

The distinctive features of the LETKF analysis are:

1. At each analysis grid point, the analysis is performed *locally*: using only nearby observations from a box (cylinder, ellipsoid, ...) surrounding the grid point—as in Optimum Interpolation (OI) (Gandin 1963, Lorenc 1981).

2. The analysis is performed in *ensemble space*: within each local box, the analysis increment belongs to the subspace spanned by ensemble deviations, $\mathbf{x}_i^f - \mathbf{x}^b$.

The details of the technique follow.

2.1 Ensemble space

We start by computing the (global) *ensemble vectors*,

$$\mathbf{e}_i := \frac{1}{\sqrt{n_e - 1}}(\mathbf{x}_i^f - \mathbf{x}^b), \tag{1}$$

where the sign := means 'equal by definition'. The normalization by $\sqrt{n_e - 1}$ is introduced into Eq.(1) only with the intention to simplify the analysis-algorithm formulae.

Next, we proceed by forming (theoretically) the ensemble matrix

$$\mathbf{E} = (\mathbf{e}_1 \cdots \mathbf{e}_{n_e}). \tag{2}$$

Note that, as it follows from Eqs.(1) and (2), the ensemble sample covariance matrix $\mathbf{B}^e$ is

$$\mathbf{B}^e = \mathbf{E} \cdot \mathbf{E}^T. \tag{3}$$

Now, we introduce *ensemble space* $\mathcal{E} := Span\{\mathbf{e}_1, \cdots, \mathbf{e}_{n_e}\}$, so that any $\mathbf{z} \in \mathcal{E}$ can be expanded in the ensemble vectors:

$$\mathbf{z} = \sum_{i=1}^{n_e} \tilde{z}_i \mathbf{e}_i \equiv \mathbf{E}\tilde{\mathbf{z}} \tag{4}$$

Here are below, by tilde, we denote coordinates of a vector in the ensemble 'basis', $\{\mathbf{e}_i\}$. Note that the set of ensemble vectors $\{\mathbf{e}_i\}_{i=1}^{n_e}$ does not constitute a true basis in $\mathcal{E}$ if $\mathbf{x}^b$ is the ensemble mean (as $\{\mathbf{e}_i\}$ sum up to zero and are thus not linearly independent). This implies that the expansion Eq.(4) does exist but can be not unique.

Thus, the control variable we wish to estimate in the analysis is $\tilde{\mathbf{x}}$ such that $\mathbf{x} = \mathbf{E}\tilde{\mathbf{x}}$. The dimensionality of $\tilde{\mathbf{x}}$ is as low as n_e (several tens, in practice).

The great advantage of making the analysis in ensemble space is that the dimensionality of $\mathcal{E}$ can be chosen much less than both the number of local influencing observations and the number of grid points in the local box. As a result of this, the analysis equations can be solved substantially faster than both in observation space and model space. But this acceleration comes at a price, which can be high: (low-dimensional) ensemble space can be too poor to reproduce the background-error spatial variability, resulting in poor analysis. In more detail, this issue is considered in section 4.2.

2.2 The ensemble-space observation model

We start with the conventional global-space observation model:

$$\mathbf{x}^o = \mathcal{H}(\mathbf{x}) + \eta, \tag{5}$$

where $\mathcal{H}$ is the observation operator, $\mathbf{x}$ the global-grid state variable (vector), and η the observation error (which consists of the measurement error and the observation-operator error). We linearize $\mathcal{H}(\mathbf{x})$ around the background $\mathbf{x}^b$:

$$\mathbf{x}^o = \mathcal{H}(\mathbf{x}^b) + \mathbf{H}(\mathbf{x} - \mathbf{x}^b) + \eta + \eta_{lin}, \tag{6}$$

where $\mathbf{H}$ is the tangent linear observation operator and η_{lin} is the error due to truncation of the Taylor series in Eq.(6). To simplify the notation, we turn to *increments*—all denoted by $\mathbf{y}$:

$$\mathbf{y} := \mathbf{x} - \mathbf{x}^b, \tag{7}$$

$$\mathbf{y}^o := \mathbf{x}^o - \mathcal{H}(\mathbf{x}^b). \tag{8}$$

With these increment variables, Eq.(6) writes

$$\mathbf{y}^o = \mathbf{H}\mathbf{y} + \eta + \eta_{lin}. \tag{9}$$

This is the linearized global-space observation-increment model. Now, we have to transform it to ensemble space.

2.2.1 The ensemble truncation (representativeness) error

An observation model in ensemble space relates the state vector in ensemble space, $\tilde{\mathbf{y}}$, to the observation increment $\mathbf{y}^o$. To build this model, we project (with an appropriately selected scalar product) $\mathbf{y}$ onto $\mathcal{E}$, getting

$$\mathbf{y} = \mathbf{y}_e + \mathbf{y}_{res}, \tag{10}$$

where $\mathbf{y}_e \in \mathcal{E}$ and $\mathbf{y}_{res} \perp \mathcal{E}$. Being in $\mathcal{E}$, $\mathbf{y}_e$ can be expanded in the ensemble vectors (see Eq.(4)), $\mathbf{y}_e = \mathbf{E}\tilde{\mathbf{y}}$. The residual in Eq.(10), $\mathbf{y}_{res}$, cannot be represented within ensemble space and, as a result of this, manifests itself as a source of *observation representativeness* error. Indeed, from Eqs.(9) and (10), we obtain

$$\mathbf{y}^o = \tilde{\mathbf{H}}\tilde{\mathbf{y}} + \eta + \eta_{lin} + \eta_{et}, \tag{11}$$

where

$$\tilde{\mathbf{H}} = \mathbf{H} \cdot \mathbf{E} \tag{12}$$

and

$$\eta_{et} = \mathbf{H}\mathbf{y}_{res} \tag{13}$$

is the error due to *ensemble truncation*.

To complete the LETKF ensemble-space observation model, we approximate the tangent-linear observation operator in Eq.(12) as follows.

2.2.2 A finite-difference approximation to H

As it is proposed in the LETKF literature, working in ensemble space enables another simplification of the analysis technique: the tangent linear observation operator (and, in the 4-D case, the tangent linear forecast model) can be usefully approximated by finite differencing. To do so, we write the first term on the r.h.s. of Eq.(11), using Eq.(12), as

$$\tilde{\mathbf{H}}\tilde{\tilde{y}} \equiv \mathbf{H}\mathbf{E}\tilde{\tilde{y}} \equiv \sum \tilde{y}_i \cdot \mathbf{H}\mathbf{e}_i \tag{14}$$

and approximate $\mathbf{H}\mathbf{e}_i$ by $\frac{1}{s}(\mathcal{H}(\mathbf{x}^b + s\mathbf{e}_i) - \mathcal{H}(\mathbf{x}^b))$, where $s := \sqrt{n_e - 1}$ and $\mathbf{x}^b + s\mathbf{e}_i \equiv \mathbf{x}_i^f$, getting

$$\mathcal{H}(\mathbf{x}) - \mathcal{H}(\mathbf{x}^b) = \frac{1}{s} \sum \tilde{y}_i \cdot (\mathcal{H}(\mathbf{x}_i^f) - \mathcal{H}(\mathbf{x}^b)) + \eta_{lin} + \eta'_{fd}. \tag{15}$$

Here, η'_{fd} represents the finite-differencing error.

It can be shown that if $\tilde{\mathbf{y}}$ is multivariate Gaussian with zero mean and $\mathcal{H}$ is only second-order non-linear, then the covariance matrix of the sum $\eta_{lin} + \eta'_{fd}$ is larger than that of η_{lin} (in the sense that difference of the two covariance matrices is a positive-definite matrix). In order to find out how important this loss of accuracy is, we need to know intricate properties of the tensor $\partial^2 \mathcal{H}_k / \partial x_i \partial x_j$, which is beyond the scope of this article. For realistic weakly non-linear observation operators the difference is expected to be small, e.g. for linear $\mathcal{H}$, both η_{lin} and η'_{fd} are equal to zero. In addition, Lorenc (2003b) noted that the linearized observation operator is encountered in the analysis equations only combined with error covariance matrices. As the latter are known only approximately, there is little sense in making the linearized observation operator 'very accurate'. So, the finite differencing error is only a minor problem, at least for not too non-linear observation operators.

In Eq.(15), it can be preferential to replace $\mathcal{H}(\mathbf{x}_i^f) - \mathcal{H}(\mathbf{x}^b)$ by $\mathcal{H}(\mathbf{x}_i^f) - \bar{\mathcal{H}}$ with $\bar{\mathcal{H}} = \frac{1}{n_e}\sum_{j=1}^{n_e} \mathcal{H}(\mathbf{x}_j^f)$, as it is done in the LETKF literature. Denoting the error of this approximation by η_{fd}, we finally obtain

$$\mathbf{y}^o = \mathbf{Z}_{glob} \cdot \tilde{\mathbf{y}} + \eta^+ \equiv \sum \tilde{y}_i \cdot \mathbf{z}_i + \eta^+, \tag{16}$$

where $\mathbf{Z}_{glob}$ is the matrix of the same size as $\tilde{\mathbf{H}}$ whose columns are $\mathbf{z}_i := (\mathcal{H}(\mathbf{x}_i^f) - \bar{\mathcal{H}})/s$, and

$$\eta^+ = \eta + \eta_{lin} + \eta_{et} + \eta_{fd} \tag{17}$$

is the total effective observation error.

Thus, the observation model relating the local ensemble-space increment vector $\tilde{\mathbf{y}}$ to the observation increments $\mathbf{y}^o$ is derived—Eq.(16). Note that the corresponding observation error, η^+, has one major additional LETKF specific component, η_{et} (due to finite ensemble size), and one minor additional component, η_{fd} (due to the finite-differencing error). The larger the observation error, the less information it bears, the less accurate the analysis. How important these additional errors are for the performance of LETKF is further discussed in section .

2.3 The analysis equations

Note that all the above equations are written for the *global* state variable and the *global* ensemble vectors. Now, it is time to *localize* the analysis. We achieve this by performing the analysis for each analysis grid point independently and limiting the number of observations used in each local analysis (only observations in a local box surrounding the analysis grid point are selected).

Specifically, from the global matrix $\mathbf{Z}_{glob}$, we build its local version, $\mathbf{Z}$, by leaving only rows that correspond to the selected observations. We also build the local version of $\mathbf{E}$, $\mathbf{E}_{loc}$, by dropping rows that correspond to grid points not within the support of any of the selected observations. Thus, the number of rows in $\mathbf{E}_{loc}$ equals the number of observed degrees of freedom in the current local analysis. It is important to notice that if non-local satellite observations are used, the $\mathbf{E}_{loc}$ matrix is enlarged due to the grid points that can be outside the selected box but within the supports of these observations. This enlargement is further discussed below in section .

For any analysis grid point, having selected 'influencing' observations, and with the observation model, Eq.(16), in hand, we easily write down the (linear) analysis equation

$$\mathbf{x}^a = \mathbf{x}^b + \mathbf{E}_{loc} \cdot \tilde{\mathbf{K}} \cdot \mathbf{y}^o, \tag{18}$$

where $\tilde{\mathbf{K}}$ is the gain matrix in ensemble space,

$$\tilde{\mathbf{K}} = (\mathbf{I} + \mathbf{Z}^T\mathbf{R}^{-1}\mathbf{Z})^{-1}\mathbf{Z}^T\mathbf{R}^{-1}, \tag{19}$$

$\mathbf{R} = \mathbb{E}\eta^+(\eta^+)^T$ is the (local) observation-error covariance matrix, $\mathbb{E}$ denotes the mathematical expectation, and the equality $\tilde{\mathbf{B}} \equiv \mathbb{E}\tilde{\mathbf{y}} \cdot \tilde{\mathbf{y}}^T = \mathbf{I}$ is used following, e.g. (Hunt *et al.* 2007). Note that if $\mathbf{R}$ is diagonal, then the only matrix that requires non-trivial inversion in Eq.(19) is $\mathbf{I}+\mathbf{Z}^T\mathbf{R}^{-1}\mathbf{Z}$, its order being as small as n_e. This results in the very fast numerical algorithm and, essentially, makes it possible to perform multiple analyses at all grid point separately.

An additional 'observation localization' is sometimes applied: the $\mathbf{R}^{-1}$ entries are multiplied by a monotonically decaying function of the distance between the center of the box and the particular observation (within the box). This *ad hoc* device acts to reduce the influence of distant observations, which, first, diminishes the detrimental impact of sampling noise in the background error covariances at large distances, and second, makes the transition from one analysis grid point to the adjacent more smooth.

3. Advantages of the LETKF analysis technique

- Simplicity

  The LETKF analysis algorithm does not require any background-error covariance *model*, which is the major simplification as compared to 3D-Var or 4D-Var.

- Computational efficiency

  First, the LETKF analysis algorithm is fast because of working in low-dimensional ensemble space. Second, as in local OI, LETKF analysis computations at all grid points are completely mutually independent, which enables very efficient parallelization in implementations on present and future massively parallel computers.

- Flow-dependent covariances

  Ensemble statistics allows to easily introduce flow dependence in the background constraint, which is a very desirable feature.

- 4D-LETKF

  The technique is easily and naturally extended to the 4-D case.

4. Weaknesses of LETKF

The above mentioned strengths of the LETKF analysis algorithm are detailed in the LETKF papers, so let us concentrate here on LETKF problems.

4.1 With non-local satellite observations, the effective box size becomes *large*

As it follows from the above description of the LETKF analysis and as it was proposed by Fertig *et al.* (2007), if the support of an observation does not lie within a local box, *global* ensemble ($\mathbf{z}_i$) vectors are used to fit the observation in the local analysis. This implies that the effective box includes supports of all non-local (non-point-support) observations. In other words, if we wish to fit a non-local observation (with the support larger than the set of grid points surrounding the observation point), there in no choice other than to control the fields within its support. As a result, the actual domain in physical space where the local analysis is done (which we call the effective box) is enlarged:

$$a_i \geq |supp\mathcal{H}|_i, \tag{20}$$

where a_i is the effective box extent (diameter), $i = x, y, z$, $|A|_i$ denotes the diameter of the set A along the coordinate axis i, and $supp\mathcal{H}$ denotes support of $\mathcal{H}$.

Supports of real observation types can be quite large:

(i) Nadir radiances are often influenced by a part of the atmospheric vertical column comparable in depth to the whole atmosphere, e.g. AMSU-A channels 6-10 have supports as large as 20-30 km in the vertical (e.g. Goldberg *et al.* 2001). So, including such observations in a *local* analysis makes it, effectively, *global* in the vertical.

(ii) Limb observations (which look through the Earth atmosphere from space to space) imply large effective *horizontal* extents of the local boxes. Indeed, a limb radiance measurement or a radio-occultation observation both depend on a *horizontal* path in the Earth atmosphere. For a thin atmosphere, the length of this tangent path is $l \approx 2\sqrt{2R_e d}$, where R_e is the Earth radius and d the effective depth of the atmosphere. If $d = 30$ km, $l \approx 1200$ km. If $d = 15$ km, $l \approx 900$ km.

Thus, we see that assimilation of (very informative in practice) non-local nadir and limb satellite observations makes the effective size of the local boxes *large*. We cannot avoid this enlargement without cutting distant parts of the observational support (i.e. without nullifying their influence on the observation operator), which would have a serious detrimental impact on their assimilation. With non-local satellite data, the effective boxes can cover (almost) the whole model atmosphere in the vertical and have horizontal extents greater than 1–2 thousand km.

4.2 Within *large* effective boxes, affordable ensemble size implies poor analysis resolution and hence accuracy

As discussed, defining the control variable in ensemble space $\mathcal{E}$ is essential for LETKF because it yields the very fast computational algorithm, but, at the same time, it is the major limitation of the technique. Indeed, as we have seen in section 2.2.1, working in $\mathcal{E}$ entails the additional observation representativeness error, η_{et}, due to the inability of a small number of ensemble vectors to span the physical space within the (effective) local box. This error reduces the analysis accuracy, especially in cases with large difference between the (low) dimensionality of $\mathcal{E}$ and the (large) number of observed degrees of freedom in the local analysis.

The implications of the ensemble being too small can be also explained from a more conventional perspective. Namely, as it is stressed many times in the LETKF and other literature and as it follows from Eq.(18) above, the local analysis increment is a linear combination of the local ensemble vectors. So, as noticed by Lorenc (2003b), in order for an EnKF analysis to be capable of fitting observation, the ensemble size should be comparable with the number of observations within the localization domain. If observations are plentiful whilst the ensemble size is small, the analysis will inevitably *smooth* the observational information, which can lead to loss of analysis accuracy. Note that this problem is also encountered in particle filters (Tsyrulnikov 2007). So, we need to make the ensemble size commensurable with the number of *observed* degrees of freedom within an effective box:

$$n_e \sim n_{odof}. \tag{21}$$

If the local spatial variability is high (the most practically important case) *and* this high variability is captured by the existing high-resolution observing systems, then we need high-dimensional analysis space (not available in LETKF) in order to represent the observed variability in the analysis increments. This is especially important on the meso scale, where small-scale phenomena are abundant both in the horizontal and in the vertical: fronts, jets, inversion layers, convective systems, polar lows, etc.

In other words, small dimensionality of analysis space implies poor resolution in a *local* analysis. In a local box with the effective extents a_i, not more than n_e features can be resolved in the local analysis. The resulting local analysis resolution measured by the effective mesh sizes h_i^{eff} is

$$h_i^{eff} \sim a_i/\sqrt[3]{n_e}. \tag{22}$$

Realizing that the typical ensemble size is $n_e = 30-100$, we conclude that the effective local resolution is only about $\sqrt[3]{n_e}\div 4$ pieces of information in each of the three spatial dimensions. Note that in the 4-D version of LETKF, the local resolution can be even less ($\sqrt[3]{n_e}$ should be replaced by $\sqrt[4]{n_e}$ in Eq.(22)).

On the other hand, we have seen in the previous subsection that assimilating non-local satellite data implies that local boxes become, effectively, as large as $(1-2)\cdot 10^3$ km in the horizontal and (almost) the whole model atmosphere in the vertical. Therefore, if these observations are assimilated, the analysis resolution within a box appears to be very poor: 3–6 km in the vertical and 200–500 km in the horizontal, which is far less than we would require even from a *global* analysis, let alone limited-area *meso-scale* assimilation.

It is worth noting that poor resolution in a local analysis means that even if there are (useful) high-accuracy observations near the centre of the box, they simply can be not resolved. As a result, the accuracy of the resulting analysis at the centre of the box is reduced. It is important to stress that the very attempt to assimilate non-local satellite data using an ensemble-space analysis technique can make assimilation of *all* observations inefficient.

The above $\sqrt[3]{n_e}$ dependency implies that high resolution in a local box cannot be even reached with the ensemble-space analysis technique in practical NWP applications. Indeed, the effective 20-km mesh size in the horizontal (100 pieces of information for a 2000-km box) and 50 levels in the vertical would require unimaginable $n_e \approx 100\cdot 100\cdot 50 = 500,000$ ensemble members, which is, certainly, not feasible. Bishop and Hodyss (2009) proposed to use a kind of resampling technique in order to 'statistically' increase the ensemble size up to thousands. In its simplest form, their idea can be used to generate 'synthetic' ensemble perturbations by $\mathbf{y}_s^* = \mathbf{E}\mathbf{a}$, where $\mathbf{a}$ is a pseudo-random vector with the unit covariance matrix and $s = 1, \ldots, S$

denotes the number of the generated perturbation. Thus defined, any $\mathbf{y}_s^*$ has the covariance matrix exactly equal to $\mathbf{B}^e$ (conditional on the forecast ensemble). Appending the 'synthetic' perturbations to the forecast ensemble perturbations increases ensemble size, improving the local resolution and reducing the ensemble representativeness error. But not dramatically, because the required very large 'synthetic' ensembles are expensive: with the dimensionality of a practical problem as large as $n = 10^8$ and $n_e = 10^2$, just generating $S = 10^4$ 'synthetic' perturbations would require huge $n \cdot n_e \cdot S = 10^{14}$ flops. So, we conclude that an ensemble-space EnKF analysis technique cannot yield high spatial resolution in practice.

Summarizing, we claim that with LETKF, it is not possible to efficiently assimilate non-local satellite data in the presence of high local spatial variability when this variability is observed.

4.3 *Small* local boxes can led to small-scale noise in the analysis increments

The LETKF analysis algorithm can be viewed as an attempt to reintroduce OI but with ensemble covariances instead of analytic ones. As a result, many OI drawbacks are inherited by LETKF. In particular, changes in the sets of influencing observations from one analysis grid point to another can lead to small-scale noise: horizontal and vertical analysis gradients become contaminated. As the gradients directly enter the prognostic equations, their accuracy is as important as accuracy of the fields themselves. In addition, inaccurate gradients can destroy *balances* (hydrostatic, geostrophic, ...).

In order to make the resulting small-scale noise reasonably low, one should ensure that in each box, observations close to its boundaries have low weights in the analysis. With observation errors similar in magnitude to background errors (a typical situation in modern data assimilation), this is the case if background-error correlations between the center of the box and the boundaries are sufficiently low. This can be achieved either by increasing the box size or by implementing the above 'observation localization'. It is worth noting, however, that severe localization distorts the effective background-error correlations: their length scales L_i may become unrealistically small, which can substantially reduce the accuracy of the analysis. So, we cannot use 'observation localization' to *radically* reduce the background-error length scales, which, thus, appear to be the approximate lower bounds for the respective box radia:

$$\frac{a_i}{2} \geq L_i. \tag{23}$$

Otherwise, we say the box is small. Now, we show that with small boxes, the noise can really be generated. We carried out a simple 1-D experiment. We supposed that the analyzed field had analytic correlation function $C(r) = (1 + r/L)\exp(-r/L)$, where r is the distance on the circle and L the length scale. We selected $L = 300$ km as a typical value for background-error correlations. The field was assumed to have unit variance. The ensemble size was chosen to be $n_e = 50$. The analysis domain was a (latitude) circle. The grid spacing was $h \approx 55$ km (1° at latitude 60°). Realizations of both the pseudo-random 'truth' and forecast perturbations were generated by forming the covariance matrix of the grid-point values, whose entries are $\mathbf{B}_{ij} = C(|r_i - r_j|)$, performing its eigen-decomposition, and perturbing the 'principal components' according to their variances given by the respective eigen-values of $\mathbf{B}$. Observations were placed at grid points with the spacing $h_{obs} = m \cdot h$. The pseudo-random Gaussian observation noise with unit variance was added. Observation errors were assumed to be uncorrelated. 'Observation localization' was implemented with the Gaussian localization function, $\exp(-0.5(r/l)^2)$, where l is the localization length scale.

In Fig.1. we show results of the experiment with $m = 4$ (each fourth grid point was observed), box diameter as small as $12h$, and $l = 3h$. The effective box diameter with the observation localization can be roughly assessed as $a_{eff} = 2l = 6h \approx 330$ km, which is close to $L = 300$ km, so the boxes are nearly small in the above sense. The solid thick curve represents one arbitrarily chosen realization of a reference-analysis increment produced using large local boxes (with diameter $50h$) and exact background-error statistics (OI, essentially). The solid thin curve represents the LETKF analysis increment. The dotted curve corresponds to the analysis produced on a coarser grid (here, 8 times coarser than the analysis grid) and post-interpolated using the weight interpolation proposed by Yang *et al.* (2009).

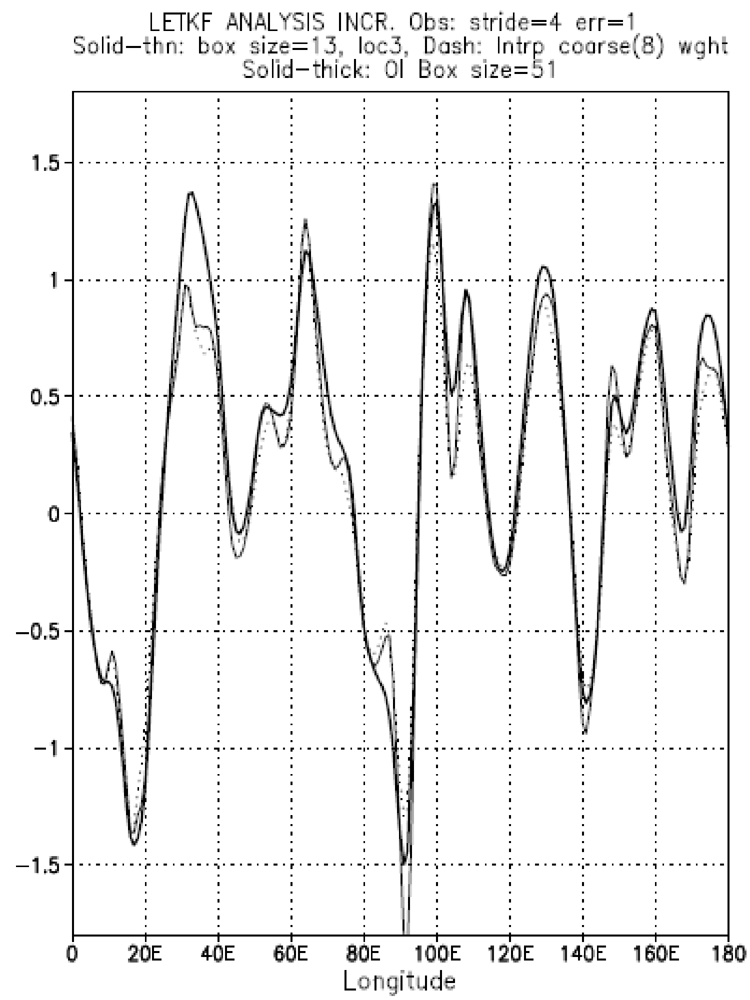

Figure 1: Analysis increment, one realization: OI box diameter 50 (solid thick curve), LETKF box diameter 12, localization length 3 (solid thin), and LETKF on coarse grid with post-interpolated ensemble weights (dotted).

From Fig.1, one can see that indeed small boxes can cause excessive and spurious extrema in LETKF analysis increments. Weight interpolation is seen to smooth somewhat the noisy analysis increments but only slightly. With the coarse-grid mesh size equal to $3h$, the resulting interpolated increment (not shown) appeared to be almost indistinguishable from the full-grid (solid thin) LETKF curve. So, the noise is really generated in spite of 'observation localization' and weight interpolation. With larger boxes, denser observation network and smaller observation errors, the noise in the increment field reduces. We remark that the these experimental results depend only on the ratio L/h, so they are equally valid for, say, $h = 1.8$ km and $L = 10$ km.

Finally, we note that, as it was proposed by Lorenc (1981) for OI and by Bishop and Hodyss (2009) for LETKF, one can suppress the small-scale noise by simultaneously updating a number of grid points near the centre of the box. But this can be only achieved at the expense of increasing the box size, which can exacerbate the ensemble-space-analysis resolution problem discussed in the previous section.

4.4 Observation-error correlations can destroy the LETKF computational efficiency

At first glance, the number of floating-point operations involved in the LETKF analysis algorithm Eqs.(18)–(19) does not critically depend on the number of observations, n_{obs}, because the (small) ensemble size (and thus the dimensionality of the system of algebraic analysis equations to be solved) remains untouched. With the increasing n_{obs}, the number of entries in the $\mathbf{Z}$ matrix and thus the number of floating-point operations (flops) in the analysis grows as $O(n_{obs})$. But this slow growth of the floating-point operation count with the box size becomes badly fast if we try to account for spatial dependencies (correlations) between the *observation errors*.

Indeed, if the local $\mathbf{R}$ matrix is dense [2], its factorization involved in the application of $\mathbf{R}^{-1}$ in Eq.(19)) requires as large as $O(n_{obs}^3)$ flops (e.g. Golub and van Loan 1989). In this case, we state that *the computational advantage of the LETKF algorithm disappears*. This issue is most important for satellite data assimilation and on the meso scale (where radar data do have spatially correlated errors (Xu *et al.* 2007)).

Hunt *et al.* (2007) discussed using 'batches' of observations with zero correlations of observational errors between different 'batches'. But this assumption is, generally, not met in case of data with spatially and temporally almost *continuous* coverage (satellites and radars). So, the 'batch' approach cannot help with these data (the 'batches' will be too large, say, all AMSU-A data will be one 'batch').

Another device capable, in principle, of removing the problem is the diagonalization of the $\mathbf{R}$ matrix before the analysis (e.g. Fertig *et al.* 2007). However, this approach again requires $O(n_{obs}^3)$ flops to compute the matrix $\mathbf{R}^{-1/2}$, which transforms the original observations $\mathbf{x}^o$ to new 'pseudo-observations' with uncorrelated errors:

$$\check{\mathbf{x}}^0 := \mathbf{R}^{-1/2} \cdot \mathbf{x}^o. \tag{24}$$

In addition, these 'pseudo-observations' become substantially *non-local* because their observation operator involves left-multiplication by $\mathbf{R}^{-1/2}$ (as it follows from Eq.(24)), which complicates their efficient assimilation in an *ensemble-space* analysis (as discussed above in section ()). So, diagonalizing the $\mathbf{R}$ matrix is not likely to give rise to a computationally efficient LETKF algorithm with correlated observation errors.

Thus, with the existing methodologies, allowing for correlated satellite and radar observation errors makes the LETKF analysis algorithm computationally inefficient (we have to solve large systems of linear algebraic equations at every analysis grid point).

Finally, we note that $\mathbf{R}^{-1}$ enters the equations of the (L)ETKF analysis ensemble generation scheme (e.g. Hunt *et al.* 2007), which can compromise the applicability of the Ensemble Transform analysis technique in the presence of correlated observational errors.

[2] Bormann *et al.* (2003) report that for AMV (atmospheric motion vectors) observations, the horizontal observation-error correlation falls to 0.5 at 300 km and to zero at about 1000 km.

4.5 Meso-scale issues

On the meso scale, a kind of *scale separation* technique can be a remedy for the above problems with the LETKF assimilation of non-local satellite data. Namely, satellite observations can be assimilated in a global variational analysis, which is used as a first guess for the 'meso' analysis, which, in turn, updates meso scales by using only locally supported 'meso' observations. In this case, the above limitations are greatly relaxed.

Indeed, first, large supports of satellite observations no longer limit the effective box size from below (as there are no 'meso' data with comparably large supports). The boxes can be made small so that the effective resolution within a box, see Eq.(22), can be reasonably high. Second, analyzing only meso scales implies small background-error length scales, so it can be easy to satisfy the requirement Eq.(23). Third, balances are known to be weak on the meso scale (e.g. geostrophy is not valid because the Rossby number is large), so there is little danger to destroy them by localization.

Thus, boxes can be made sufficiently small, which would result in enhanced spatial resolution within a box without excessive smoothing of observations, without generating small-scale noise, and without destroying multivariate balance constraints. However, at scales less than about 1 km, the radar error correlations appear to be significant (Xu *et al.* (2007) report on the 2-km decorrelation radius). In this case, the LETKF algorithm can lose its computational efficiency and its real-data applicability becomes questionable.

We also note that on the meso scale, strong non-linearity of forecast equations can lead to highly non-Gaussian background-error distributions. But Lawson and Hansen (2004) showed that the ensemble transform technique is incapable of properly blending the non-Gaussian prior distribution and the largely Gaussian observation-error distribution. So, on the meso scale, a perturbed-observations technique seems to be more suitable than an ensemble-transform based technique.

5. Published experimental evidence

(1) Concerning satellite data, we state that the only attempt to assimilate real radiances with the LETKF methodology was reported in (Szunyogh *et al.* 2007a) but without detailed presentation of the results. Simulated radiances were assimilated by Fertig *et al.* (2007). All peer-reviewed papers reporting on real-data assimilation (listed in the Introduction) do *not* involve satellite radiances, in spite of the fact that these latter are known to be the crucial part of the global atmospheric observing system (e.g. Kelly and Thépaut 2007).

(2) The necessity of the above relationship, Eq.(21), between the ensemble size and the number of observed degrees of freedom within a box is largely confirmed by the published experimental results: practical schemes appear to work reasonably well if this condition is met. Specifically, Szunyogh *et al.* (2005) found that for $n_e = 40$, when every 9-th horizontal grid point was observed, the best results were obtained with about $n_{dof} = 500$ model variables within the box (see their Fig.8). We note that in this optimal configuration, the number of *observed* degrees of freedom within a box is about $n_{odof} = 500/9 \approx 56$, which is very close to $n_e = 40$.

Fertig *et al.* (2007) found that simulated radiosonde observations were most effectively assimilated with $n_e = 20$ if $n_x = n_y = 7$ and the boxes were only one level deep. The analysis variable comprised 4 three-dimensional fields, so a box contained $n_{dof} = 7{\cdot}7{\cdot}4 \approx 200$ degrees of freedom. But not all of them were observed. Concretely, they used about 600 simulated radiosonde profiles, so that with their analysis grid having $48 \cdot 96 = 4600$ grid points, only a portion of 600/4600 $\approx 1/8$ was observed. Hence $n_{odof} = n_{dof}/8 \approx 25$, which is in excellent agreement with $n_e = 20$.

Miyoshi and Yamane (2007) came up with the following optimized parameters of their LETKF scheme. In their OSSE1 experiments, the box size for $n_e = 40$ was: $n_x = 11$ with the Gaussian observation localization length equal to 3 mesh sizes and $n_z = 7$ with the vertical localization length 2 mesh sizes. As the localization lengths are smaller than the respective box extents, we easily assess the effective box sizes in each of the two horizontal dimensions as $2 \cdot 3 + 1 = 7$ grid points and, in the vertical, $2 \cdot 2 + 1 = 5$ grid points, so that there were, roughly, $7 \cdot 7 \cdot 5 = 245$ grid points within a box. With 5 three-dimensional analysis fields, we obtain $n_{dof} = 5 \cdot 245 = 1225$ effective analysis degrees of freedom. But only each hundredth degree of freedom was observed, which yields $n_{odof} = 1225/100 \approx 12$. This small number explains why Miyoshi and Yamane (2007) found that even n_e as small as 10 could be used.

(3) As regards the possible generation of small-scale noise due to the local nature of the LETKF analysis, Liu *et al.* 2008 reported on a very successful behaviour of LETKF. They used low resolution in the horizontal (about 450-500 km), so that the box size was large ($a_x \approx$ 3000 km). With the box size this large, it is likely that our condition Eq.(23) was satisfied. Indeed, this is the case if the horizontal background-error length scale is as large as $L \leq 1500$ km, which is significantly higher than the typical length scales (300–500 km). Similarly, local boxes in (Szunyogh *et al.* 2005) were, in their base experiment, about $1000 \div 1400$ km broad.

On the other hand, tiny $n_x = n_y = 3$ boxes in (Harlim and Hunt 2007b) *did* lead to small-scale noise, as we would expect (see their Figs. 3 and 5).

(4) No attempt to account for realistic observation-error correlation was reported on yet, so we cannot check the conclusions of section 4.4.

Summarizing this section, we note that our theoretical inference on the applicability of the LETKF analysis does not contradict to the existing experimental evidence and seems to provide explanation for some experimental results.

6. Discussion

We have shown that the major deficiency of the present formulation of the LETKF analysis is its inability to efficiently assimilate non-local satellite observations. This is because in each local LETKF analysis, the analysis increment is confined to be a linear combination of (a small number of) the forecast ensemble perturbations. With other EnKF formulations, this limitation can be relaxed. Solving the analysis equations in observation space allows us to apply covariance localization (e.g. Houtekamer and Mitchell 2006), so that the analysis increment no longer belongs to the low-dimensional ensemble space. Another suitable approach is to use spatially averaged covariances (Raynaud *et al.* 2008). Hybrid EnKF-3DVar schemes also allow us to avoid the ‘curse of (low) dimensionality’ of ensemble space (Hamill and Snyder 2000, Lorenc 2003b, Wang *et al.* 2007).

The experimental fact that LETKF can quite successfully (despite locality and ensemble-space restrictions) assimilate conventional observations, suggests that the *ensemble* data assimilation principle is indeed promising for operational and other purposes. We notice, however, that good results reported in the LETKF and some other ensemble data assimilation papers (e.g. Whitaker *et al.* 2008) were obtained without satellite data, i.e. for poorly observed flows, where the errors have time to develop complicated anisotropic structures. With the addition of frequent and ubiquitous satellite observations, it is likely that the effect of flow-dependent covariances may appear to be less dramatic.

7. Conclusions

The main findings of this study are:

- Non-local satellite observations (both nadir and limb) are shown to make the effective size of local LETKF boxes large: extended by supports of all used observations.
- Small ensemble size implies small number of resolvable features in local LETKF analyses. Large effective boxes and small ensemble size imply, thus, low spatial resolution within a local box, which can make the assimilation of all observations inefficient— if non-local satellite data (radiances, in particular) are assimilated.
- Without non-local satellite data, the local-box extents are limited from below by the respective background-error length scales. Smaller boxes can give rise to significant small-scale noise in the analysis increments.
- Allowing for realistic correlations in observation errors (e.g. for satellite and radar data) removes the advantage of LETKF in computational efficiency as compared to observation-space formulations.

All in all, we state that the LETKF approach in its present formulation does not seem to be a good general method of choice for operational data assimilation on the global scale. LETKF can be utilized as a means of meso-scale data assimilation in a scale-separation scheme without non-local satellite observations. The LETKF technique, being simple and cheap, can be successfully used to solve some other particular data assimilation problems and in other applications (research, education, etc.).

8. Acknowledgments

I appreciate a discussion with B. Hunt on the issues raised in the article. This review is written at request of COSMO working group WG1.

References

[1] Baek S-J, Hunt BR, Kalnay E, Ott E, and Szunyogh I. 2006. Local ensemble Kalman filtering in the presence of model bias. *Tellus*, **58A**: 293-306.

[2] Bishop CH., Hodyss D. 2009. Ensemble covariances adaptively localized with ECO-RAP. Part 2: a strategy for the atmosphere. *Tellus*, **61A**: 97-111.

[3] Bonavita M, Torrisi L, Marcucci F. 2008. The ensemble Kalman Filter in an operational regional NWP system: Preliminary results with real observations. *Q.J.Roy. Meteorol. Soc.*, **134**: 1733-1744.

[4] Bormann N, Saarinen S, Kelly G and Thepaut J-N. 2003. The spatial structure of observation errors in atmospheric motion vectors from geostationary satellite data. *Mon. Wea. Rev.*, **131**: 706-718.

[5] Fertig EJ, Hunt BR, Ott E, and Szunyogh I. 2007. Assimilating non-local observations with a local ensemble Kalman Filter. *Tellus*, **59A**: 719-730.

[6] Gandin LS. 1965. *Objective analysis of meteorological fields*. Gidrometeorologicheskoe izdatelstvo, Leningrad, 1963. Translated from Russian, Israeli Program for Scientific Translations: Jerusalem.

[7] Golub GH and van Loan CF. 1989. *Matrix computations*. The John Hopkins University Press.

[8] Goldberg MD, Crosby DS, and Zhou L. 2001. The limb adjustment of AMSU-A observations: methodology and validation J. Appl. Meteorol., **40**: 70-83.

[9] Hamill TM and Snyder C. 2000. A hybrid ensemble Kalman Filter–3D variational analysis scheme. *Mon. Wea. Rev.*, **128**: 2905-2919.

[10] Harlim J and Hunt BR. 2007a. A non-Gaussian ensemble filter for assimilating infrequent noisy observations. *Tellus*, 59A, **59A**: 225-237.

[11] Harlim J and Hunt BR. 2007b. Four-dimensional local transform Kalman Filter: numerical experiments with a global circulation model. *Tellus*, **59A**: 731-748.

[12] Houtekamer PL and Mitchell HL. 2006. Ensemble Kalman filtering. *Q.J.Roy. Meteorol. Soc.*, **131**: 3269-3289.

[13] Hunt BR, Kalnay E, Kostelich EJ, Ott E, Patil DJ, Sauer T, Szunyogh I, Yorke JA, and Zimin AV. 2004. Four-dimensional ensemble Kalman filtering. *Tellus*, **56A**: 273-277.

[14] Hunt BR, Kostelich EJ, and Szunyogh I. 2007. Efficient data assimilation for spatiotemporal chaos: A local ensemble transform Kalman Filter. *Physica D*, **230**: 112-126.

[15] Kalnay E, Li H, Miyoshi T, Yang S-C, and Ballabrera-Poy J. 2007. 4-D-Var of ensemble Kalman Filter? *Tellus*, **59A**: 758-773.

[16] Kelly G and Thépaut J-N. 2007. Evaluation of the impact of the space component of the Global Observing System through Observing System Experiments. *EUMETSAT / ECMWF Report Series Final report SOW EUM.MET.SOW.04.0290.*

[17] Lawson WG and Hansen JA. 2004. Implications of stochastic and deterministic filters as ensemble-based data assimilation methods in varying regimes of error growth. *Mon. Wea. Rev.*, **132**: 1966-1981.

[18] Liu J, Fertig EJ, Li H, Kalnay E, Hunt BR, Kostelich EJ, Szunyogh I, Todling R. 2008. Comparison between local ensemble transform Kalman Filter and PSAS in the NASA finite volume GCM – perfect model experiments. *Nonlin. Processes Geophys.*, **15**: 645-659.

[19] Lorenc A. 1981. A global three-dimensional multivariate statistical interpolation scheme. *Mon. Wea. Rev.*, **109**: 701-721.

[20] Lorenc AC. 2003a. Modelling of error covariances by 4D-Var data assimilation. *Q.J.R. Meteorol. Soc.*, **129**: 3176-3182.

[21] Lorenc AC. 2003b. The potential of the ensemble Kalman Filter for NWP – a comparison with 4D-Var. *Q.J.R. Meteorol. Soc.*, **129**: 3183-3203.

[22] Miyoshi T and Yamane S. 2007. Local ensemble transform Kalman filtering with an AGCM at a T159/L48 resolution. *Mon. Wea. Rev.*, **135**: 3841-3861.

[23] Ott E, Hunt BR, Szunyogh I, Zimin AV, Kostelich EJ, Corazza M, Kalnay E, Patil DJ, Yorke JA. 2004. A local ensemble Kalman Filter for atmospheric data assimilation. *Tellus*, **56A**: 415-428.

[24] Raynaud L, Berre L, and Desrosiers G. 2008. Spatial averaging of ensemble-based background-error variances. *Q.J.Roy. Meteorol. Soc.*, **134**: 1003-1014.

[25] Szunyogh I, Kostelich EJ, Gyarmati G, Patil DJ, Hunt BR, Kalnay E, Ott E, Yorke JA. 2005. Assessing a local ensemble Kalman Filter: perfect model experiments with the National Centers for Environmental Prediction global model. *Tellus*, **57A**: 528-545.

[26] Szunyogh I, Satterfield EA, Aravequia JA, Fertig EJ, Guarmati G, Kalnay E, Hunt BR, Kostelich EJ, Kuhl DD, Ott E, Yorke JA. 2007a. The local ensemble transform Kalman Filter and its implementation on the NCEP global model at the University of Maryland. *Proceedings of the ECMWF Workshop on Flow dependent aspects of data assimilation*, ECMWF, Reading, UK, 47-64.

[27] Szunyogh I, Kostelich EJ, Gyarmati G, Kalnay E, Hunt BR, Ott E, Satterfield E, Yorke JA. 2007b. A local ensemble transform Kalman Filter data assimilation system for the NCEP global model. *Tellus*, **59A**: 1-18.

[28] Tsyrulnikov MD. 2007. Is the particle filtering approach appropriate for meso-scale data assimilation? *COSMO Technical Report N 10*, 1-16 (http://www.cosmo-model.org/content/model/documentation/techReports/docs/techReport10.pdf).

[29] Wang X, Hamill TM, Whitaker JS, Bishop CH. 2007. A comparison of hybrid ensemble transform Kalman Filter–Optimum Interpolation and ensemble square root filter analysis schemes. *Mon. Wea. Rev.*, **135**: 1055-1076.

[30] Whitaker JS, Hamill TM, Wei X, Song Y and Toth Z. 2008. Ensemble data assimilation with the NCEP global forecast system. *Mon. Wea. Rev.*, **136**: 463-482.

[31] Xu Q, Nai K, Wei L. 2007. An innovation method for estimating radar radial-velocity observation error and background wind error covariances. *Q.J.Roy. Meteorol. Soc.*, **133**: 407-415.

[32] Yang S-C, Kalnay E, Hunt BR, Bowler N. 2009. Weight interpolation for efficient data assimilation with the Local Ensemble Transform Kalman Filter. *Q. J. Roy. Meteorol. Soc.* 135, 251-262.

The importance of small-scale analysis on the forecasts of COSMO-DE

Klaus Stephan and Christoph Schraff

Deutscher Wetterdienst, Frankfurter Strasse 135, 63067 Offenbach, Germany

1 Introduction

With respect to the development of a new assimilation method for COSMO (within the COSMO priority project KENDA) the question arises, which benefit can be expected from small-scale details in the analysis on the quality of COSMO-DE forecasts. To address this question three experiments were conducted for a 2-week-convective summer period in June 2007. This period was dominated by weak anti-cyclonic conditions with frequent air-mass convection in the afternoon. A convective period was chosen, small-scale features in the analysis are expected to be more relevant than in periods governed by large scale circulation.

2 Experimental Setup

Three experiments were conducted, each of them starting forecasts at 00, 06, 12 and 18 UTC (denoted hereafter as 00-UTC, 06-UTC, 12-UTC and 18-UTC runs) from different analyses:

1. starting from an interpolated COSMO-EU analysis,
2. starting from a COSMO-DE analysis with LHN of radar derived rain rates,
3. starting from a COSMO-DE analysis without LHN of radar derived rain rates.

All experiments were performed with COSMO model version 4.8, using the new setting of the PBL parameters suggested by Seifert et al. (2008). The boundary conditions for the forecasts are the one's of the operational setup, which means there were derived from 3 hour old COSMO-EU forecasts. To achieve the best comparability the soil moisture at the beginning of each forecast and analysis run was identical in all 3 experiments by setting equal to the first experiment (i.e. interpolated analysis). Furthermore all forecast were started from the respective analysis of the assimilation cycle in contrast to the operational setup, where a forecast starts from its time-critical analysis. This means that the data cut off is considerably larger than in the operational setup and the set of observations used in the three different analyses of this study are nearly the same.

3 Results

The model results were verified against different observation types, i.e. ground base SYNOP stations, radiosondes, radar derived precipitation rates and integrated water vapour measured by GPS. The verification results in general indicated that the more small-scale feautures are represented within the analysis the better are the forecasts. That means, model runs assimilating radar derived rain rates are the best ones followed by the runs starting from the small-scale analysis. Forecast starting from an interpolated analysis were found to have the lowest quality. In some situations the forecast quality is quite similar. But in cases where the weather conditions are dominated by small-scale phenomena the differences are biggest. This leads to the fact, that 00-UTC or 06-UTC runs are more comparable than 12-UTC or 18-UTC runs. This may be related to the fact, that more benefit is found from the small-scale analysis in 12-UTC or 18-UTC runs than for 00-UTC and 06-UTC runs.

- verification against SYNOP observations:
  Both experiments starting from small-scale analyses tend to improve the quality of the forecast. Especially in the first forecast hours the quality is generally better. Both, RMSE and BIAS are improved. The biggest improvement due to small-scale analyses is found for PMSL (see fig. 1) and 2m temperature. Then forecasts tend to be warmer in 2m temperature and lower in PMSL. The results suggest that the improvements are largest for 18-UTC and 00-UTC runs, whereas the improvements in 6-UTC or 12-UTC runs are smaller, but still present.

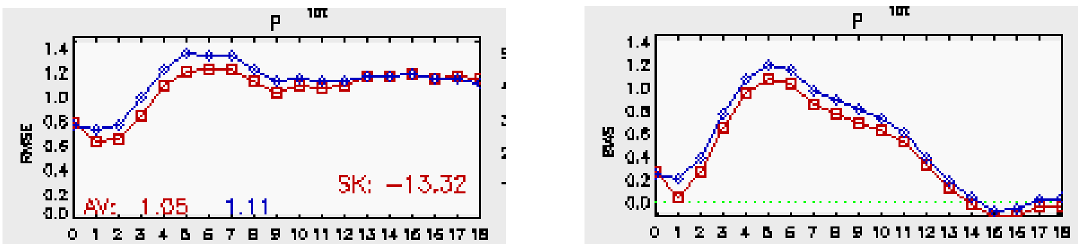

Figure 1: RMSE (left) and BIAS (right) in PMSL against SYNOP measurements over forecast time. 00 UTC forecasts starting from interpolated COSMO-EU analysis (blue) and COSMO-DE analysis (red).

- verification against radiosondes,
  The upper air verification (see fig. 2) depicts the largest difference between the small-scale analyses and the coarse-scale analysis within the mid troposphere. Here the coarse-scale analysis verifies worse and tends to be more cold and wet. This is more pronounced at 12 UTC than at 00 UTC. Also the vertical extent of the difference is greater at noon

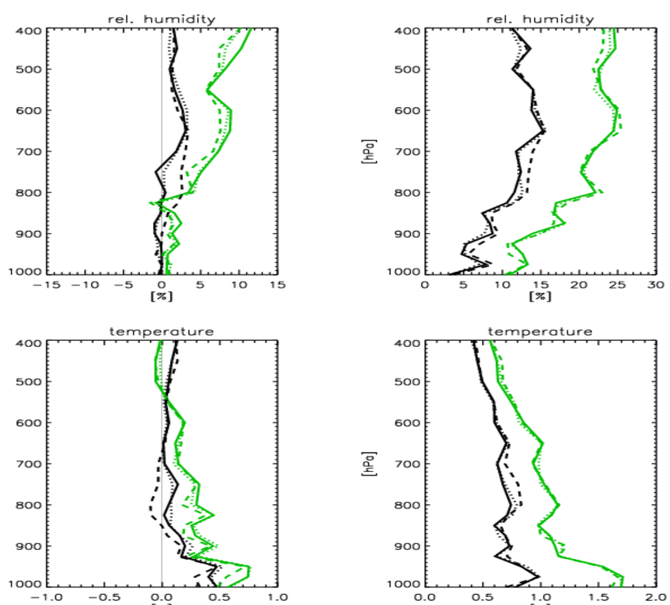

Figure 2: Verification against radio sondes at 12 UTC: Bias (left) and RMSE (right) for relative humidity (upper panels) and temperature (lower panels) at analysis time (black lines) and +12h forecast time (green): bold lines COSMO-DE analysis with LHN, dotted lines COSMO-DE analysis without LHN, dashed lines interpolated COSMO-EU analysis.

and includes the boundary layer. All differences have almost vanished after 12 hour forecast time.

- verification against radar derived rain rates:

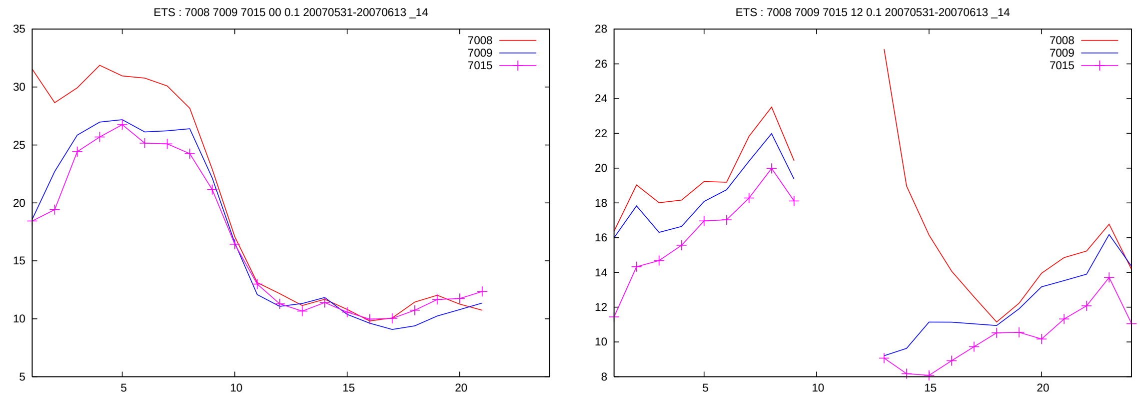

Figure 3: Equitable threat scores against radar observations (threshold of 0.1 mm/h) for 00-UTC runs (left) and 12-UTC runs (right): COSMO-DE analysis with LHN (red), COSMO-DE analysis without LHN (blue), interpolated COSMO-EU analysis (magenta plus sign).

Equitable threat score (fig. 3) show the ability of the LHN analysis to greatly improve the forecast within the first few hours (up to 6 hours, seefig. 3). This agrees well with the results from former studies (Stephan et al. (2008)). Even the small-scale analysis without LHN provides better forecast quality than the coarse-scale analysis. The quality is improved most in the 12-UTC and 18-UTC runs. Furthermore all experiments show a strong dependency of forecasting the diurnal cycle of precipitation on the starting time of the forecast (see fig. 4). 12-UTC runs are not able to produce an acceptable diurnal cycle and in particular they tend to miss the peak of convective precipitation in the afternoon. All other forecasts show better results and the older the forecast the more the modell seems to be able to simulate that peak.

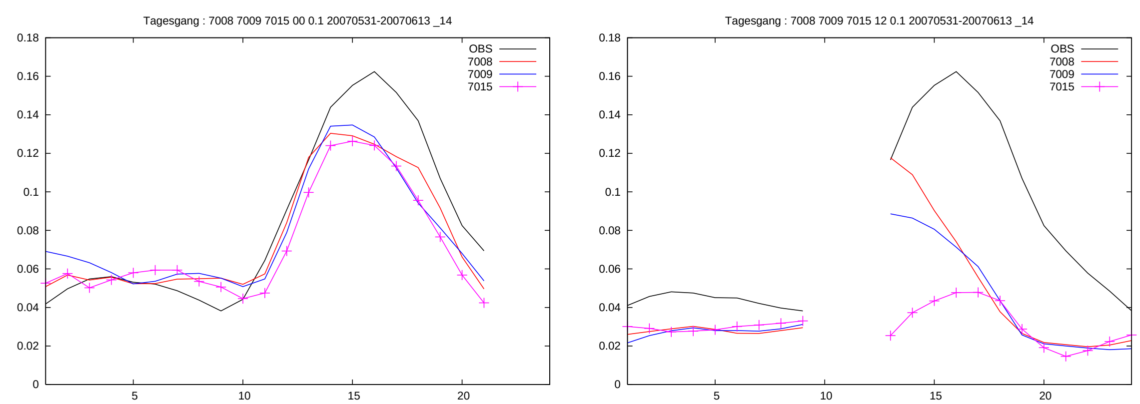

Figure 4: Averaged diurnal cycle of precipitation rate for 00-UTC runs (left) and the 12-UTC runs (right) starting on: COSMO-DE analysis with LHN (red), COSMO-DE analysis without LHN (blue), interpolated COSMO-EU analysis (magenta plus sign). The black line depicts the observations.

Also with respect to the diurnal cycle, the small-scale analysis, and especially the LHN analysis is most beneficial to the 12-UTC and 18-UTC runs, whereas the impact on 12-UTC runs is limited to the first 4-5 hours.

- verification against GPS derived integrated water vapouri (IWV):

Forecast starting from the small-scale analyses verify better against GPS derived IWV during night (see fig. 5). At daytime, and especially in the early afternoon the quality of all three experiments are comparable. At these hours the forecasts starting from the interpolated analysis tend to be even a bit better than the other forecasts. This result seems to be independent from the starting time of the forecast. Furthermore it reveals the fact that the forecasts starting from the interpolated analysis tend to be dryer than the others. The wettest forecasts are the ones which start from the LHN analysis. The differences are greater for 00-UTC runs than for 12-UTC runs.

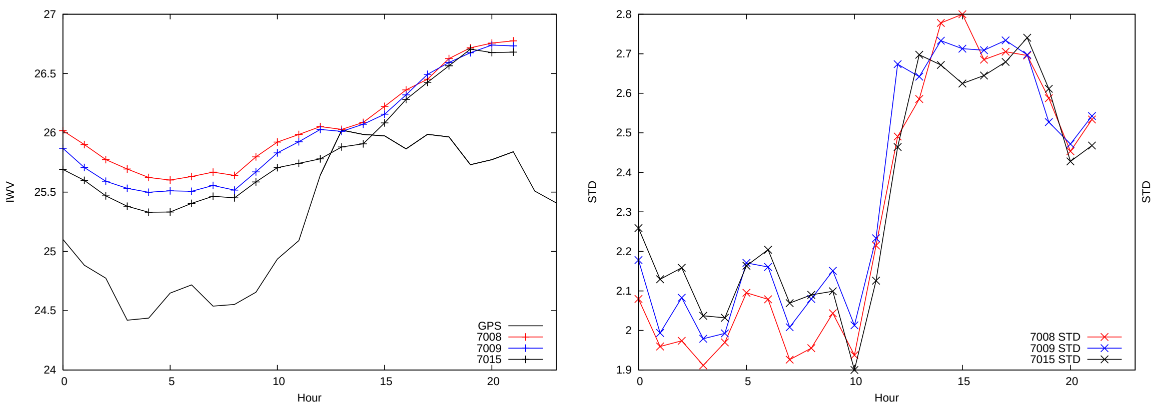

Figure 5: Averaged diurnal cycle of integrated water vapour (IWV, left) and standard diviation (right) of 00-UTC runs: GPS IWV measurements (black), COSMO-DE analysis with LHN (red), COSMO-DE analysis without LHN (blue), interpolated COSMO-EU analysis (black plus sign).

4 Conclusions

A study with the convection permitting model COSMO-DE has been made to indicate whether and how much small-scale detail in the analysis could improve QPF. For the selected two-week summer period dominated by weak anti-cyclonic weather conditions with air-mass convection, the local weather was expected to be clearly influenced by small-scale effects. It has been found that in some cases, the additional small-scale detail in the analysis significantly improved QPF, and statistically, the largest benefit has been found for the forecasts starting at 12 UTC (noon) or 18 UTC. This motivates further investments in high-resolution data assimilation, and namely in the development of an EnKF-based scheme for COSMO.

References

[1] K. Stephan, S. Klink, C. Schraff, 2008: Assimilation of radar derived rain rates into the convective scale model COSMO-DE at DWD. *Q.J.R.Meteorol.Soc.* **134**, 1315-1326

[2] A. Seifert, M. Baldauf, K. Stephan, U. Blahak, K. Beheng, 2008: The challenge of convective-scale quantitative precipitation forecasting, *Proc. 15th Int. Conf. Clouds and Precip., Cancun, Mexico*, 2008

Recent updates of the COSMO-SREPS ensemble system

C. Marsigli[1], F. Gofa[2], P. Louka[2], A. Montani[1], T. Paccagnella[1]

1 ARPA-SIMC, Bologna, Italy
2 HNMS, Athens, Greece

1 Introduction

The perturbations applied to the COSMO-SREPS ensemble have been recently updated, in order to improve the representation of the model error in the ensemble system. The new ensemble configuration is presented in Section 2, where the motivations for this update are also briefly described. In Section 3, a preliminary analysis of the impact of the new perturbations is shown, both in terms of the spread/skill relationship for 2m temperature and in terms of the quality of the different ensemble members.

2 The new COSMO–SREPS configuration

The new ensemble configuration has been selected on the basis of both an extensive testing of new perturbations of the parameters and some physical considerations about the meaning of the parameters, carried out by HNMS. The testing of the new perturbations was performed using the CSPERT suite, a test suite running at ECMWF, using Billing Units from a Special Project (SPITFEAR), where different parameter perturbations are applied. This suite was run over two seasons: autumn (SON) 2007 and summer (JJA) 2008. The quality of the different perturbations was assessed through an objective verification performed both at ARPA-SIMC (over the Alpine area) and at HNMS (over Greece). The outcome of this analysis, together with the aforementioned considerations on the meaning of the parameters, is presented in the SREPS Priority Project Final Report (Marsigli, 2009) and in the CONSENS Quarterly Report March-May 2009 (available on the COSMO web site).

The present COSMO-SREPS configuration is shown in Fig. 1.

member	father	itype_conv	tur_len	pat_len	rlam_heat	rat_sea	crsmin
1	ecmwf	0	150	500	1	20	150
2	ecmwf	1	1000	500	1	20	150
3	ecmwf	0	500	500	0.1	20	200
4	ecmwf	1	500	10000	1	20	150
5	gme	0	500	10000	1	20	150
6	gme	1	500	500	0.1	20	150
7	gme	0	500	500	1	1	200
8	gme	1	500	500	1	1	150
9	avn	0	1000	500	1	20	150
10	avn	1	150	500	1	20	150
11	avn	0	500	500	10	20	150
12	avn	1	500	500	10	20	150
13	ukmo	0	500	500	1	60	150
14	ukmo	1	500	500	1	60	150
15	ukmo	0	500	500	1	20	50
16	ukmo	1	500	500	1	20	50

Figure 1: Scheme describing the new COSMO–SREPS set–up.

The initial and boundary conditions are provided to the ensemble members by the 4 COSMO members of the SREPS system of AEMET (Garcia-Moya et al., 2009), which are 4 runs of COSMO at 25 km horizontal resolution, nested on 4 different global models (IFS, GME, GFS, UM). Then, 16 different set-ups of the physics parameters are applied to the 16 members, irrespective of their driving model. It has to be emphasised that the new suite is no longer symmetric with respect to the perturbations. Hence, for example, the 4 members driven by IFS are now different from the 4 members driven by GME as well as in the physics set-up, while before the same set of 4 physics perturbations was applied to each group of members with the same driving model.

A preliminary analysis of the performance of the new suite over summer 2009 (JJA) is presented in the next section.

3 Preliminary results

An evaluation of the spread/skill relationship of the ensemble in terms of 2m temperature is shown in Fig. 2. The rms error is represented against the rms spread as average values for each class. The classes of spread have been selected in order to be homogenous in terms of class population. The computation is made over the whole domain, for the verification of forecasts at 00 UTC (left panel) and at 12 UTC (right panel).

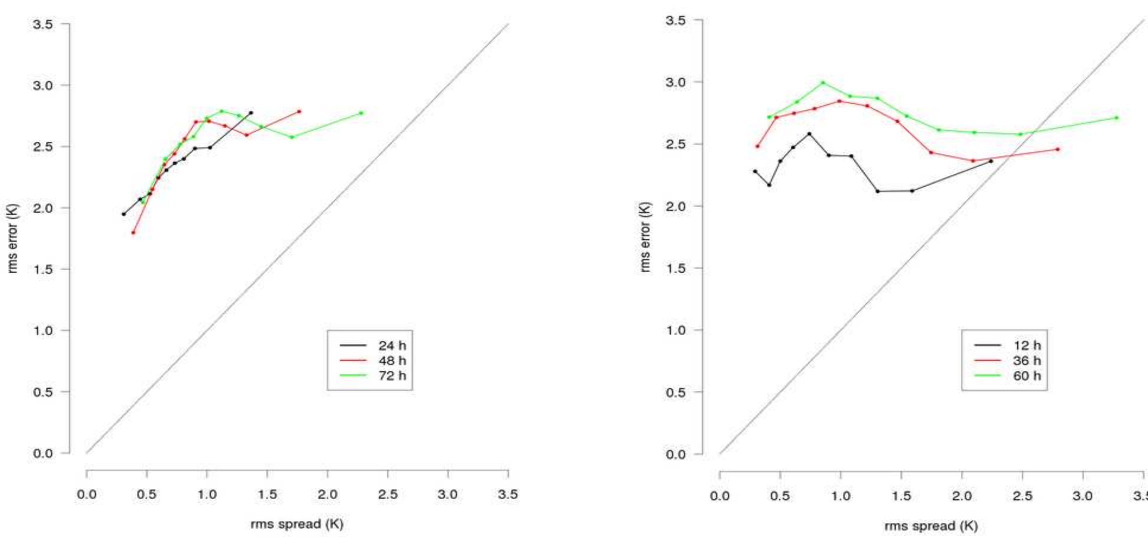

Figure 2: Spread/error relationship of COSMO-SREPS in terms of 2m temperature for the verification of forecasts at 00 UTC (left panel) and at 12 UTC (right panel). The black line is for the first forecast range, the red line for the second and the green line for the third.

While at 00 UTC there is a good relationship between spread and error, though with a strong underdispersion, at 12 UTC the spread does not provide valuable information about the forecast error. This can be due to the dependence of the model bias on the time of the day. As discussed in previous analyses (Marsigli, 2009), it is believed that the bias of the COSMO model in 2m temperature affects this result, by inflating the error to an amount which cannot be represented by the spread.

In order to ensure that the model perturbations applied in the new COSMO-SREPS suite are not producing a general worsening of the forecasts, an evaluation of the performance of the forecasts issued by the 16 members was also carried out. Up to now, this has been done in terms of 2m temperature only over the Alpine area and in term of the continuous parameters (T, U and Td) over Greece. Precipitation has not yet been considered mainly due to the fact that, during the summer season, precipitation over the two areas was not strong enough, but it will be considered for the next season.

In Fig. 3, the BIAS and Mean Absolute Error of the 16 forecasts in terms of 2m temperature are shown, as a function of the forecast range. The scores are computed for the summer season (JJA 2009), over the alpine domain, using data from the SYNOP stations. The same analysis has also been done over Greece, using data from SYNOP stations as well (not shown). The 16 lines are plotted with the same grey colour, except for the lines representing the score of the members where the tur_len parameter is perturbed.

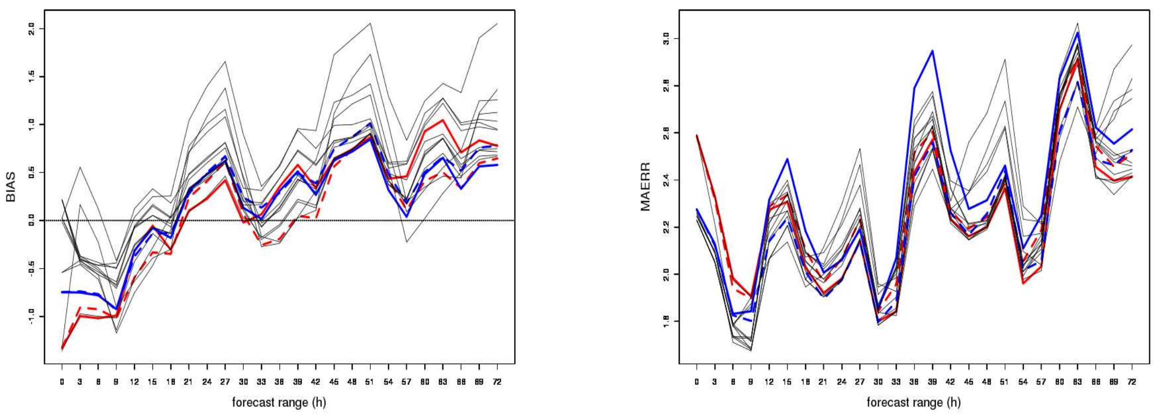

Figure 3: BIAS and Mean Absolute Error of the 16 forecasts in terms of 2m temperature over the alpine area, as a function of the forecast range. The coloured lines represent the score of the members where the tur_len parameter is perturbed.

The effect of these perturbations is generally reasonable, but the run driven by NCEP with the small tur_len value shows high MAE values during daytime. This feature, which also appears in the verification carried out over Greece, will be monitored in the future, in an attempt to establish if it is statistically persistent over a longer period.

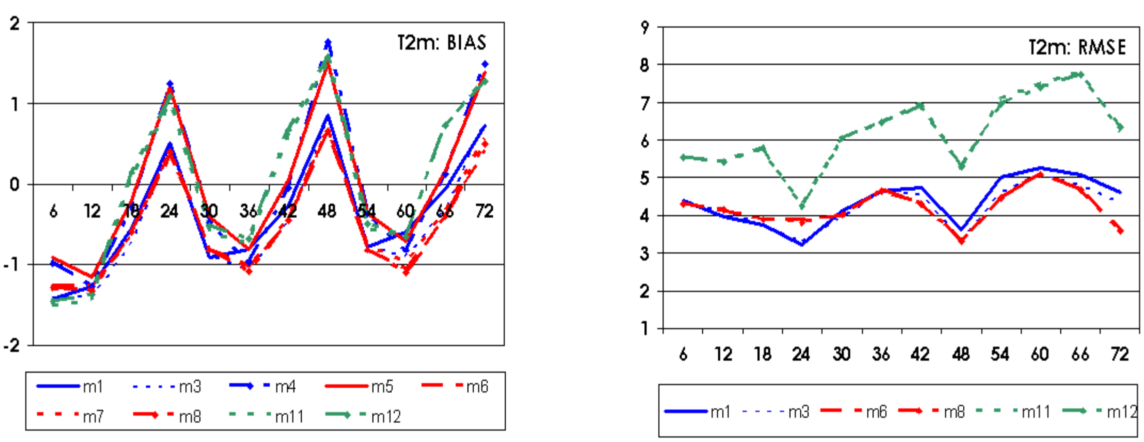

Figure 4: BIAS and Root Mean Square Error of the 16 forecasts in terms of 2m temperature over Greece, as a function of the forecast range. The green lines are for the members where rlam_heat is increased to 10.

Another parameter which deserves attention in the future is rlam_heat. In Fig. 4, the BIAS and RMSE values for some members of COSMO-SREPS are plotted, for the 2m temperature forecasts verified over Greece. The most striking feature is that the members represented by the green lines (m11 and m12) show a large value of RMSE. These two members are those where the rlam_heat parameter was increased to the value of 10. This feature was not evident in the verification carried out over the alpine area (not shown). Hence, this parameter will also be monitored in the future, in order to determine wether this perturbation should be retained or rejected.

4 Summary and Outlook

A preliminary analysis of the new configuration of the COSMO–SREPS ensemble system has been carried out. Before drawing any conclusions on the impact of the new parameters, it is necessary to complete the analysis. The spread/error relationship will also be computed for other meteorological variables (temperature at 850 hPa, mean sea level pressure, precipitation). Furthermore, the bias and error of the different ensemble members will be calculated for another season, focussing on precipitation. Up to now some parameters have been identified as important to be monitored. Finally, new parameters are already under testing in the experimental CSPERT suite, including parameters of the microphysical scheme. Since it is believed that perturbing the physics parameters alone it is not sufficient to have a proper representation of the model error, the perturbation of some soil fields will also be included, starting from soil moisture. This work is being carried out at HNMS.

References

[1] Garcia-Moya, J.A., A. Callado, C. Santos, D. Santos-Munoz and J. Simarro, 2009: Predictability of Short-range Forecasting: A Muli-Model Approach. *Nota Tcnica 1 del Servicio de Predicibilidad y Predicciones Extendidas* (NT SPPE-1), pp. **30**.

[2] Marsigli, C., A. Montani and T. Paccagnella, 2009: COSMO Priority Project "Short Range Ensemble Prediction System" (SREPS): Final Report. *COSMO Technical Report No. 13*, pp.**33**.

Statistical properties and validation of Quantitative Precipitation Forecast

Maria Stefania Tesini, Carlo Cacciamani, Tiziana Paccagnella

Hydro meteorological Regional Service ARPASIMC, Bologna, Italy
email: mstesini@arpa.emr.it

1 Introduction

Observed precipitation fields show a high variability both in space and time and the amount of rainfall could vary a lot within a short distance.(Zepeda-Arce et al.,2000). The increasing of horizontal resolution in NWP models seems to enable them to reproduce this variability, even if frequent errors in time and space positioning make difficult a grid-point based employment of models QPF. In order to asses the ability of the models in reproducing the variability of the precipitation fields, we investigated the statistical properties of the observed and forecasted rain values falling within a predefined geographical area and in a specific time period (also called boxes). In particular we studied the distribution function (*pdf*)and evaluated some summarizing quantities, such as the mean, the maximum value and quantiles for each of the selected box. Results for different size of the chosen areas and period of time are used to validate the QPF of the COSMO suites that run operationally at ARPA-SIMC (COSMO-I7 and COSMO-I2) in comparison with the global model IFS-ECMWF.

The aim of this study is to provide an interpretation key for more correct use of models QPF, especially with respect to high precipitation events.

2 Dataset and methodology

Observed precipitation data consisted of about 1500 rain-gauges made available by the Italian National Department of Civil Protection and, in the framework of the COSMO Cooperation, by a number of Italian regions and Meteo-Swiss. The dataset cover almost all the Italian territory, (see figure 1) even if it is not homogeneous both in space and time. In this work we considered only precipitation values accumulated over 24h , starting at 00 UTC or, in same cases , at 6 UTC. The QPF field investigated in this study is provided by COSMO-I7 (7 km horizontal resolution), COSMO-I2 (2.8 km horizontal resolution) and the global model IFS-ECMWF (25 km horizontal resolution, and 50 km horizontal resolution before 2006). In most of the cases the 00 UTC runs have been taken into account, and the grid-point forecasted values refer to the +24h (or +30h) of integration, even if in same tests (not shown in this work) we considered also the precipitation from +24h to +48h. In order to compare the observations with the forecasted rain field we devised a strategy that takes into account all the observed values and grid-point forecasted values falling into a predefined geographical area, several times wider than the horizontal resolution of the model. As a starting point ,the domain is dived in squared areas, with size and position chosen subjectively and depending on the available number of observation stations and geographical features of the territory. We assumed that the precipitation occurrence in each of the stations points and grid-points within the selected area is equi-probable. The size and the dimension of the area play a crucial role in order to consider well-founded this assumption. In this preliminary study we followed a pragmatic approach: we should have enough forecast and observation points to perform significant statistics in each box. The precipitation values of all stations and all

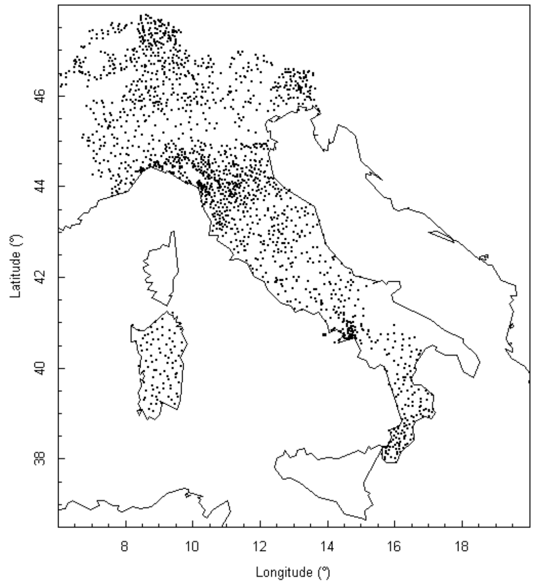

Figure 1: Location of rain-gauges in Italy

model grid-points falling in the same box are aggregated and processed by using two different approaches, schematically described in figure 2. In the first approach, called "*representative value approach*" the evaluation of a summarizing value for the precipitation field in each box, such as the mean or the maximum, has been performed. The second approach consisted in the study of full distribution function of the precipitation values in each area, mainly from a qualitative point of view.

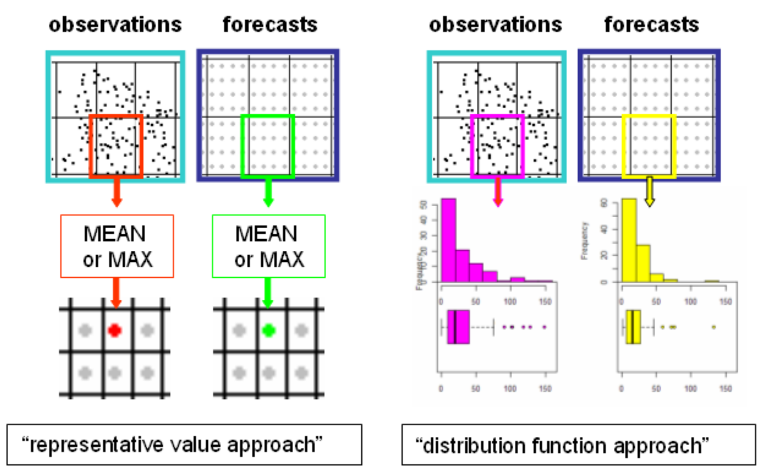

Figure 2: Description of the used approaches to evaluate QPF quality in the selected boxes

3 Results: Validation of QPF using the "representative value approach"

The QPF quality is assessed by making a comparison of a representative value in each box for observations and forecasts, using a methodology developed in the past years at ARPA-SIMC for the verification of COSMO-LEPS high-resolution precipitation forecasts (Marsigli et al.,2008). The verification domain is divided in boxes of 0.5 x 0.5 degree about 50 x 50 Km) in order to contain four IFS-ECMWF grid-points. Each box contains about

45 COSMO-I7 grid-points, 280 COSMO-I2 grid-points, while, as regards the precipitation observation, the number of stations vary between 3 and about 40 (only boxes with at least 3 observations inside have been considered in the computation of the verification scores). Categorical statistics (e.g. Probability of Detection, Frequency Bias, False Alarm Ratio) have been computed from the elements of contingency tables, on the basis of the exceeding of some predefined precipitation thresholds by the representative value (mean or maximum) of forecast and observation for each box over the period of interest. Some results concerning the period Autumn 2008 are presented as example in figure 3 (mean value exceeding the threshold of 1 mm/24h), figure 4 (mean value exceeding the threshold of 20 mm/24h) and figure 5 (maximum value exceeding the threshold of 20 mm/24h), but in outline they are representative of the verification over other periods.

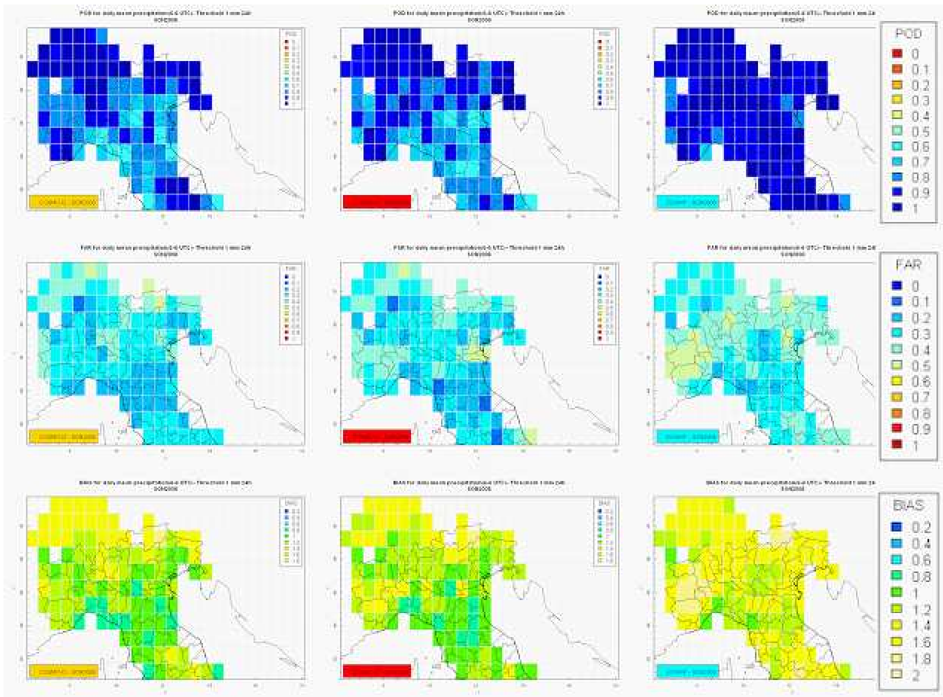

Figure 3: Probability Of Detection (top panels), False Alarme Ratio (middle panels), Frequency Bias (bottom panels), for mean value exceeding the threshold of 1 mm/24h for the models COSMO-I2 (left), COSMO-I7(center),IFS-ECMWF(right)

The results of this type of verification point out a strong dependence on the choice of the thresholds. For low thresholds (e.g. 1 or 5 mm/24h) and in particular for the mean value as indicator, the difference in the scores of the three models are small (except for the BIAS SCORE where IFS-ECMWF has values everywhere greater than one, showing a tendency to over-forecast the precipitation events) and quite independent on geographical location. Increasing the thresholds (e.g. 10 or 20 mm/24h) the scores tend to be very sensitive to the geographical positioning of the considered area and the performance of the models become very different, in particular if the maximum values are considered. In this case the COSMO models seem to have better scores, in particular the POD, even if the number of false alarm cases increases. On the other hand, IFS-ECMWF shows less false alarms but also a noticeably decreases in the BIAS SCORE, moving from a situation of over-forecast at lower thresholds to a situation of under-forecast at higher thresholds, especially when the maximum value is taken into account. The worsening in the scores concerning the maximum values, that means at least one points should exceed the thresholds, suggests that the lower resolution models have difficulties in reproducing high localized precipitation events, such as for example convective events.

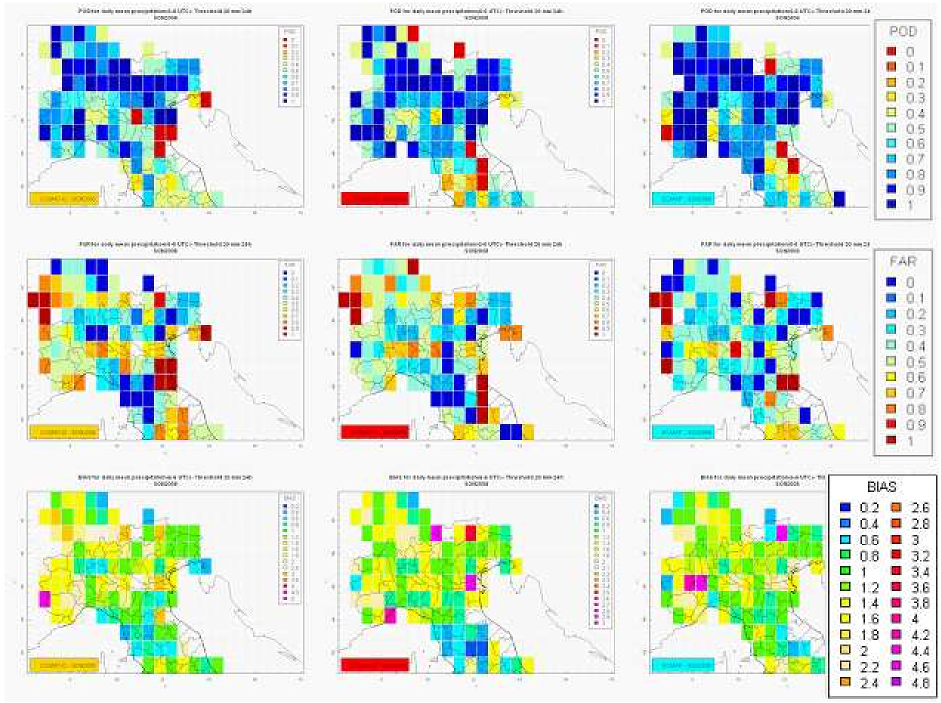

Figure 4: Probability Of Detection (top panels), False Alarme Ratio (middle panels), Frequency Bias (bottom panels), for mean value exceeding the threshold of 20 mm/24h for the models COSMO-I2 (left), COSMO-I7(center),IFS-ECMWF(right)

The "*representative value approach*" has been used also to evaluate the seasonal accumulation of the precipitation, in order to investigate the ability of the models in reproducing the total amount of rain occurred, taking no notice of the daily correspondence of observations and

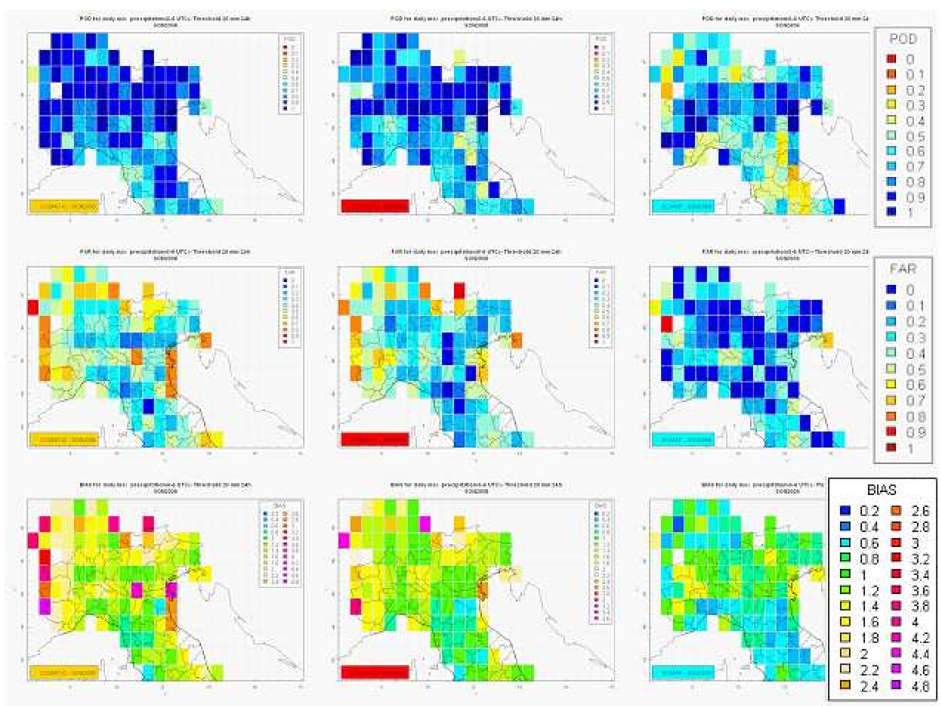

Figure 5: Probability Of Detection (top panels), False Alarme Ratio (middle panels), Frequency Bias (bottom panels), for maximum value exceeding the threshold of 20 mm/24h for the models COSMO-I2 (left), COSMO-I7(center),IFS-ECMWF(right)

forecasts. For each box all the forecasted and observed daily mean (or maximum) values are accumulated over "common days" (depending on the availability of observations). Results concerning the period March-April 2009 with boxes of 50 km x 50 km are presented in figure 6 (sum of the mean values) and figure 7 (sum of the maximum values). The maps of observed total amount, visualized in the bottom-right corners, show a strong dependence on the geographical positions of the boxes, depicting the morphological feature of the Italian territory. The observed precipitation pattern is quite well reproduced by COSMO-I7 and perhaps even better by COSMO-I2, considering both mean and maximum values cases. On the other hand IFS-ECMWF does not show the observed geographical variability in the accumulated precipitation pattern and in the case of the maximum values the amount of rain is definitely underestimated.

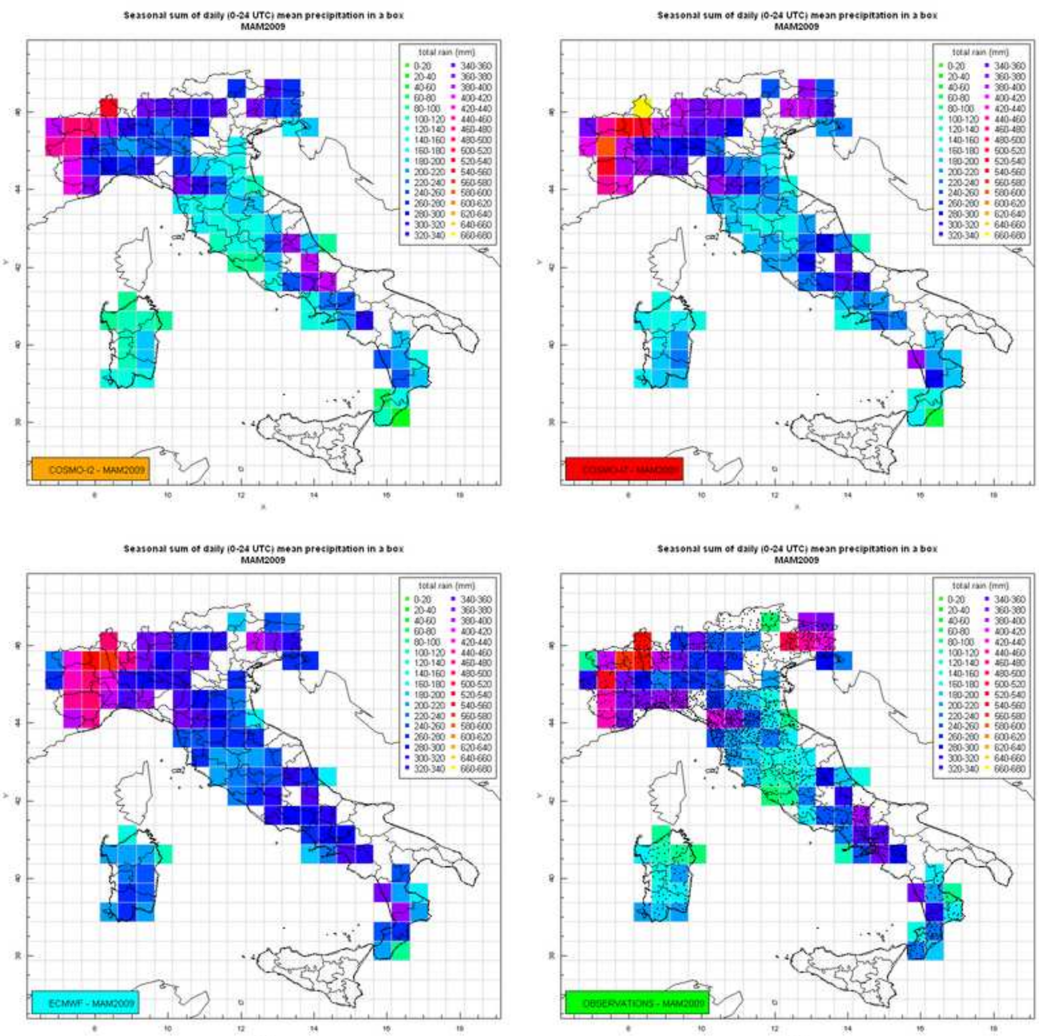

Figure 6: Accumulation of daily mean precipitation over the period March-April 2009: Observations(bottom right),COSMO-I7(top right), COSMO-I2 (top left), IFS-ECFMF (bottom left)

4 Results: Assessment of quality of QPF *pdfs*

In order to asses the ability of models in reproducing the variability of the precipitation fields inside a box over a period of time, we focused on the study of their distribution function (*pdf*), mainly form a qualitative point of view. We used a box-plot representation, that easily provides information about the spread of the distribution and furnishes a roughly

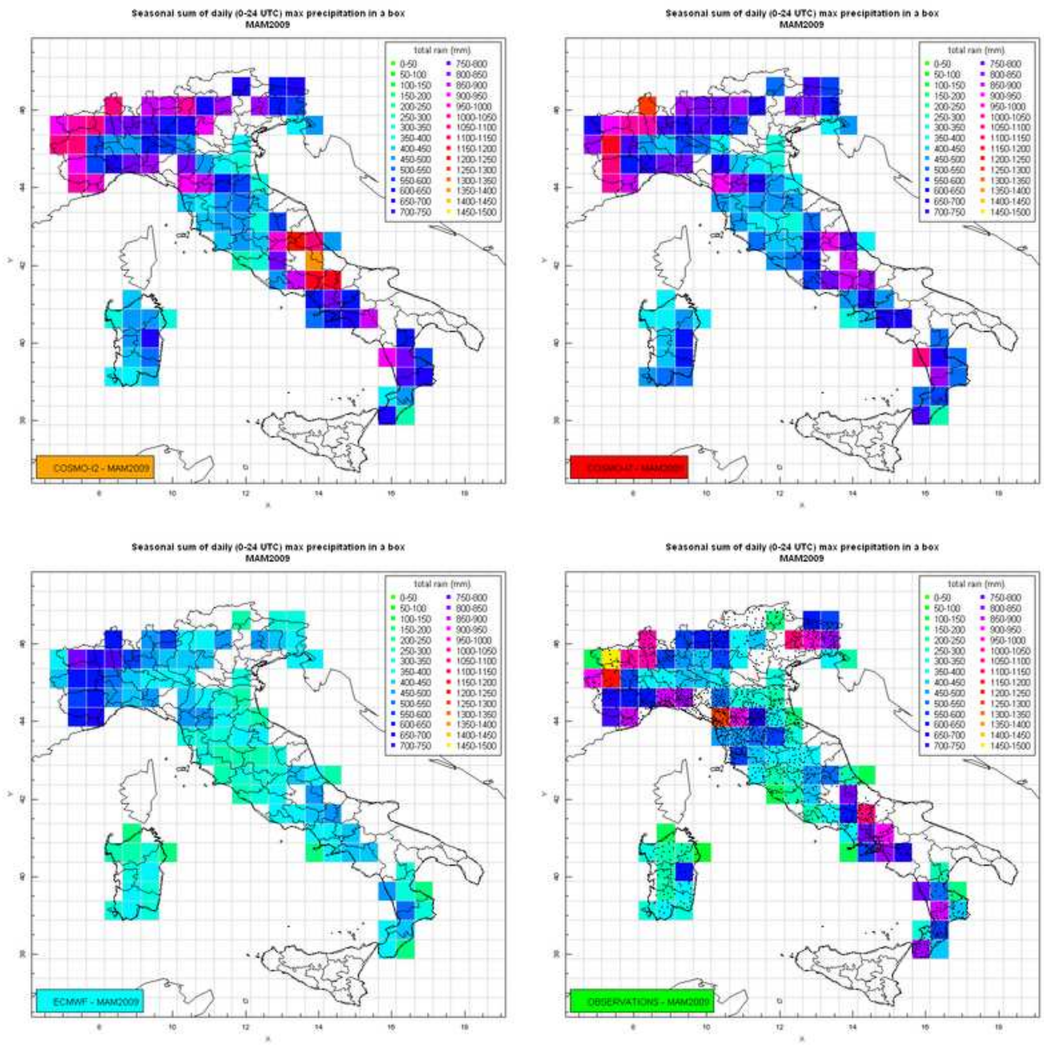

Figure 7: Accumulation of daily maximum precipitation over the period March-April 2009: Observations (bottom right), COSMO-I7 (top right), COSMO-I2(top left), IFS-ECFMF (bottom left)

description of the key measures that define it, such as the median, the quartiles, maximum and minimum values, and a range of values identified as "outliers". Chronologically our first attempt to investigate the distribution function of the precipitation fields was done comparing the models COSMO-I7 and IFS-ECMWF, considering area of about 100 km x 100 km selected on the basis of the geographical position. The idea was to select, for example, area with homogeneous terrain (almost entirely flat or in the same mountain slope) in order to consider equi-probable, at least in a first approximation, the precipitation falling in each point of the area. The subdivision of the Italian territory in 1x1 degree boxes is shown in 8.

The main aim of that study was the assessment of the "climatology" of the forecasted and observed precipitation in each box over a relative long period of time (e.g. same season for a couple of years), taking into account, for the study of the distribution functions, all the daily precipitation in each points of the area of interest.

In figure 9, as an example, by means of the box-plot representation are displayed the distribution of COSMO-I7 QPF (red), observations (green) and IFS-ECMWF QPF (blue) for each area of the study (along the x-axis), concerning the period Autumn 2005 (named: SON2005) and Autumn 2007 (named: SON2007). Green dotted lines in each panel represent the 99th and 90th percentile of the observed rain distributions, while the red and blue lines refer

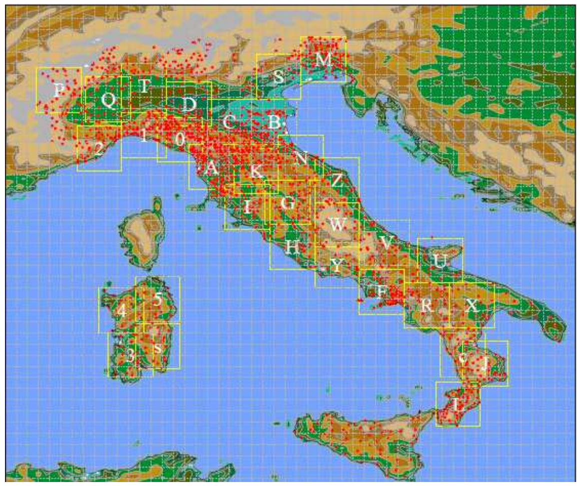

Figure 8: distribution of 1x1 degrees boxes over Italian territory

respectively to the model QPF distributions. The distribution of observed rain shows that the 90 % of rain events throughout SON2005 and SON2007 is generally lower than about 20 mm/24hours, with a large variability due to geographical position of the areas. Events greater than 50 mm/24hours represent only 1% of the total, but it is noteworthy that these are just the events in which forecasters are interested in for the issue of high impact weather warnings.

COSMO-I7 distribution seems to be fairly realistic, at least since the 90th percentile, even if in many areas also the 99th percentile is well described. Greater differences are due to outliers, with large overestimation of the maxima in many areas. However, it should be noted that very often the results could be affected by spatial representation problems, such as in costal areas that present sea points not covered by observation. The features of the observed *pdf*, and in particular the spread of the tail of the distribution, seem to be reasonably well reproduced. On the other hand, the spread of IFS-ECMWF *pdf* does not cover all the range of the observed values, with large underestimation both of 90th and 99th quantiles.

In the "representative approach" the daily comparison among forecasts and observations was performed using only some indicator of the distribution of the precipitation fields, nevertheless, even in a small area (e.g. 2500 Km^2) , the difference in the amount of rain from a station to an other one can be large. In figure 10 is presented ,as an example, the time-series of the daily distribution for the month April 2009 in an area of 50 km x 50 km in the east of Sardinia.

For each day along the x-axis , the box-plot represents the distribution of the amount of rain within the selected area. Considering, for example, the observed rain for the 12^{th} of April (presented in the bottom-right corner): it ranged from a minimum of about 15 mm/24h to more than 60 mm/24h as a maximum, with most of the values around 30 mm/24h. This intra-box variability is quite well reproduced by the COSMO models, in particular COSMO-I2, even if in terms of mean values IFS-ECMWF can be considered the more accurate. Of course the number of grid-points inside a box play an important role (only 4 for IFS-ECMWF), nevertheless this is the major aspect to be taken into account in order to appreciate the additional information that higher resolution models can provide. On the other hand this example pointed out that the precipitation verification based on the comparison of station point against the nearest grid-point is in general very misleading, in particular for non homogeneous terrain where orographic effects can influence the precipitation structures, or in case of convective events.

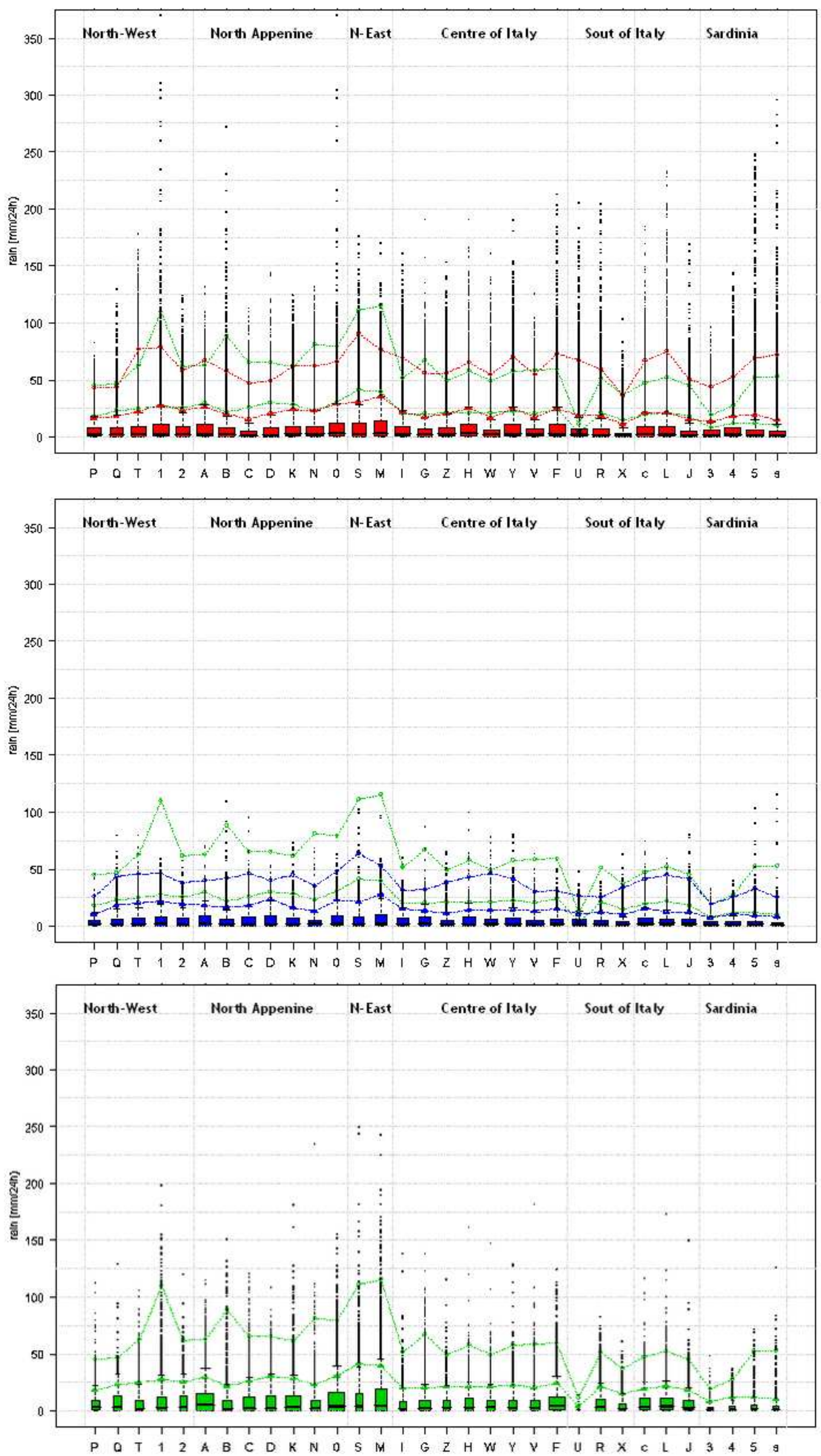

Figure 9: Distribution of COSMO-I7 QPF (red, top panel), IFS-ECMWF QPF (blue, central panel) and observations (green, bottom panel) for the period SON2005 and SON2007 in each area of the study

5 Conclusions

In this study the variability of the observed and forecasted precipitation fields in relatively small areas has been investigated, considering the COSMO model implementations running operationally at ARPA-SIMC (COSMO-I7 and COSMO-I2) in comparison with the global

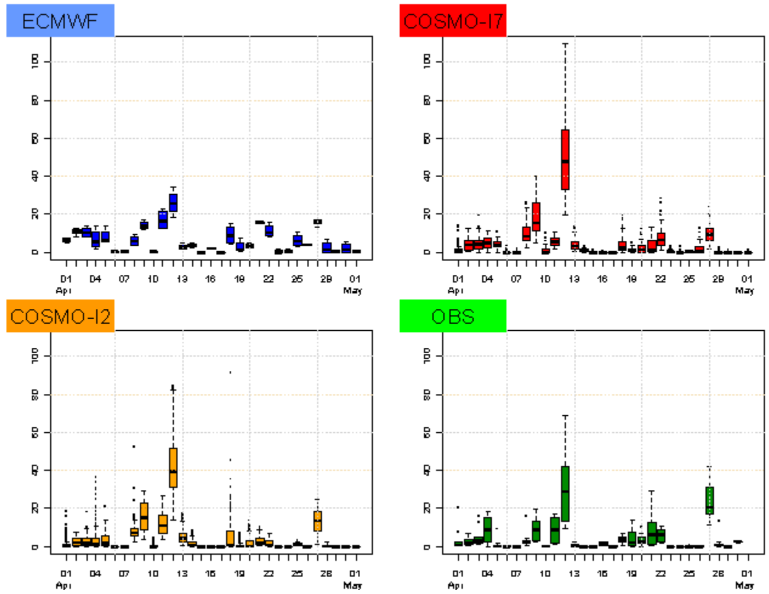

Figure 10: Time-series of the daily distribution for the month April 2009 in an area of 50 km x 50 km in the east of Sardinia

model IFS-ECMWF. The study of the distribution functions over a quite long period (e.g. two seasons) has pointed out, mainly from a qualitative point of view, that the distribution function COSMO-I7(the higher resolution model in the preliminary study) seems to be fairly realistic, at least since the 90th percentile, even if in many areas also the 99th percentile is well described. Greater differences are due to outliers, with large overestimation of the maxima in many areas. The features of the observed *pdf* , and in particular the spread of the tail of the distribution, seem to be reasonably well reproduced. On the other hand, the spread of IFS-ECMWF *pdf* (the lower resolution model in this study) does not cover all the range of the observed values, with large underestimation both of 90th and 99th percentile. The study of the intra-box variability of the daily amount of rain confirms the ability of higher resolution models in reproducing the main features of the distribution function of precipitation fields; in particular COSMO-I2 seems to be the more realistic while COSMO-I7 in many cases presents too high maximum values. These qualitative considerations about the distribution functions of forecasted and observed precipitation fields are confirmed also from a quantitative point of view considering the results of the QPF verification based on the "representative value approach". When the mean value is taken into account for the evaluation of the categorical statistics, the result pointed out the good quality of IFS-ECMWF, especially if lower reference thresholds are considered. Increasing the precipitation thresholds and taking into account the maximum value for the evaluation of the statistical scores, higher resolution models tend to gain respect to lower resolution model, even if the number of false alarm is also relatively high. On the other hand, IFS-ECMWF presents a greater number of missed alarms when we choose high reference thresholds. According to most standard verification measures, high resolution model forecasts would have poor quality, but it might be very valuable to the forecaster since it provides information on the distribution and variability of the rain field over the considered region. It's also interesting to note the strong dependence of the models behaviour on the geographical positioning of the boxes, on the period of the year and on weather type occurrence. In some areas models exhibit different behaviour depending on season, and throughout the same season they perform differently according to a different weather regime. This aspect is even more evident for higher resolution models because of the stronger interaction of the synoptic flow with the orography.

References

[1] Marsigli,C., Montani,A., Paccangnella,T.,2008: A spatial verification method applied to the evaluation of high-resolution ensemble forecasts, *Meteorol. Appls.*, **15**, 125-143

[2] Zepeda-Arce, J, E. Foufoula-Georgiou, and K. Droegemeier, 2000. Space-time rainfall organization and its role in validating quantitative precipitation forecasts, *J. Geophysical Research*, 105(D8), **10**,129-**10**,146.

QPF verification for 2008/2009 of several COSMO-Model versions

Elena Oberto [1], Massimo Milelli [1], Matteo Giorcelli [2]

1 ARPA Piemonte, Via Pio VII 9, I-10135 Torino, Italy
2 ARIANET S.r.l, via Gilino 9, I-20218 Milano, Italy

1 Introduction

In this report we present the QPF verification of the 4 model versions at 7 km resolution (COSMO-I7, COSMO-7, COSMO-EU, COSMO-ME) and 2 model versions at 2.8 km resolution (COSMO-I2, COSMO-IT) using high resolution network of rain gauges coming from COSMO dataset and Civil Protection Department, that counts about 1300 stations. In detail, we show an update of the most recent results highlighting the failings and the improvements of the 00 UTC runs up to +24h. The skills and the scores are calculated considering an accumulation time of 6h or 24h, averaged over 90 meteo-hydrological basins that cover all the peninsula with the exception of some Southern regions.

2 Long period verification

We have carried out the seasonal verification for the coarser models for the first and second day for the following thresholds: 0.2 mm/24h, 2 mm/24h, 10 mm/24h, 20 mm/24 starting from DJF 2004 to MAM 2009. The main results relatively to the first 24h for the lower and higher thresholds are reported in the next pictures, Fig. 1 and Fig. 2 respectively:

- for low thresholds it is noticeable a seasonal cycle in Bias with big peaks during summertime; the biggest overestimation is for Cosmo-I7 (Fig. 1);
- in general it is evident a Bias reduction trend for low thresholds (Fig. 1);
- the Pod index has got a stable or slight worsening trend in time for low thresholds (Fig. 1);
- the Pod index has got a slight improvement trend in time for high thresholds (Fig. 2);
- the best Pod performance is during spring/summertime for low thresholds (Fig. 1);
- the worst Pod performance is during summertime for high thresholds, probably due to the difficulty to detect correctly the intense and localized convective events (Fig. 2);
- a Far reduction has been achieved, with the worst performance during summertime both for low and high thresholds (Fig. 1 and Fig. 2);
- the Ets shows a slight improvement trend in time with a seasonal cycle both for low and high thresholds: it becomes better during moist seasons and worse during dry seasons (Fig. 1 and Fig. 2);
- for high thresholds the Bias reduction trend has been confirmed (at least for the latest years, where it appears to have a general good performance); also the seasonal cycle with the big peaks during spring-summertime (the convective period) has been confirmed, although it seems to disappear during the latest summer (Fig. 2);

- Cosmo-7 underestimates the precipitation amount and gets worse in terms of Pod during the latest seasons both for low and high thresholds (Fig. 1 and Fig. 2).

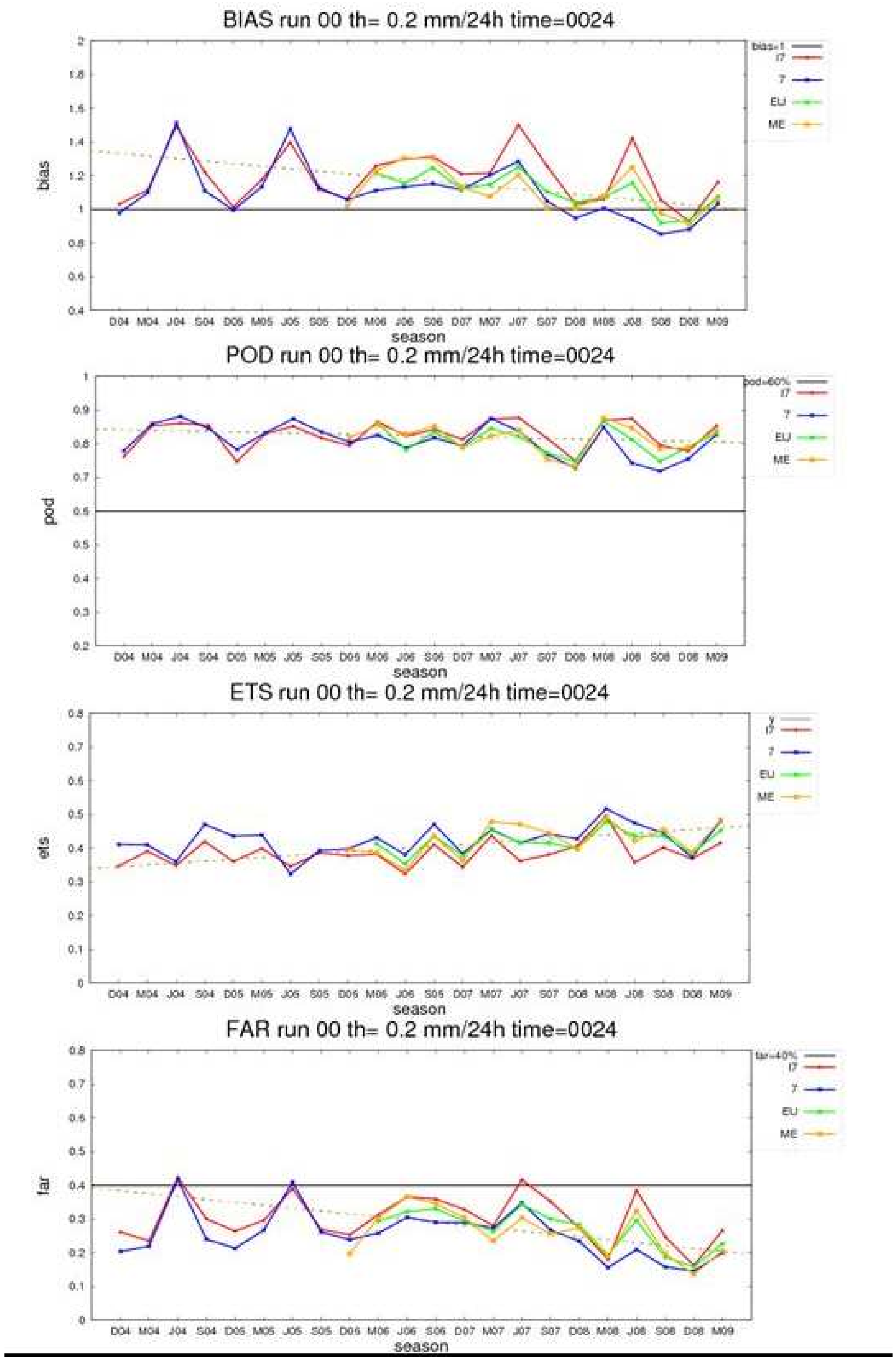

Figure 1: Bias, Pod, Ets and Far: seasonal trends from DJF 2004 to MAM 2009 for 0.2 mm/24h.

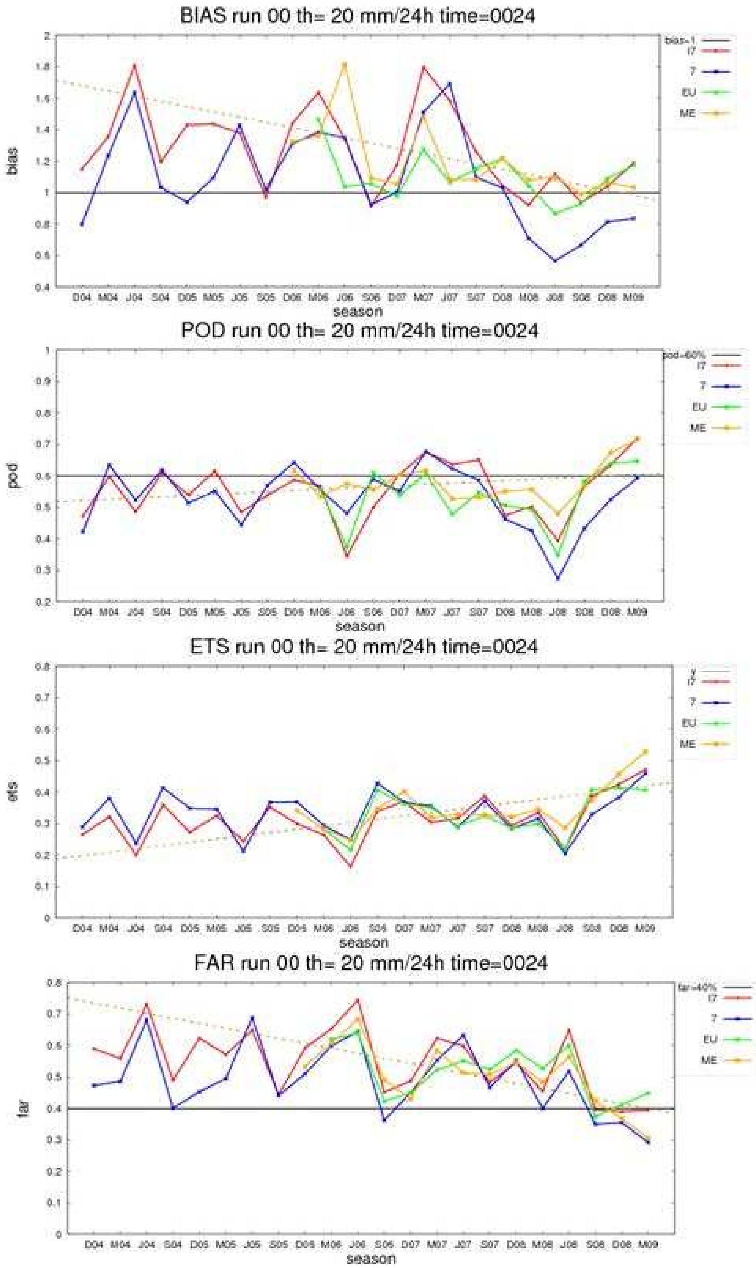

Figure 2: Bias, Pod, Ets and Far: seasonal trends from DJF 2004 to MAM 2009 for 20 mm/24h.

3 Verification over the latest years

A focus on the verification over the latest years is reported here.

Comparison between Cosmo-7 and Cosmo-EU

In Fig. 3 we plot Bias, Pod, Ets and 1-Pofd versus increasing thresholds considering a period from 200806 to 200905. It is noticeable a good performance of Cosmo-EU while Cosmo-7 underestimates the amount of precipitation (even if it forecasts more correctly the non-events).

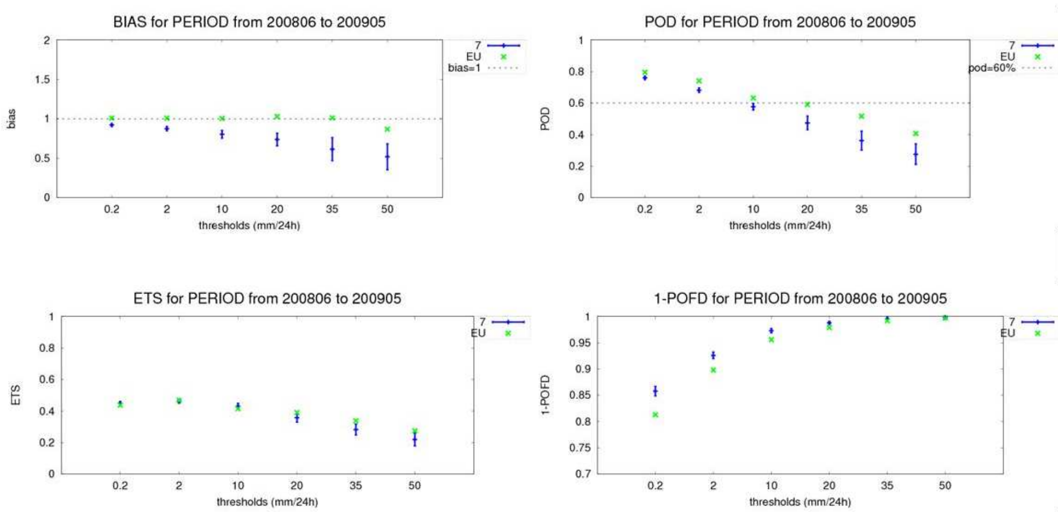

Figure 3: Bias, Pod, Ets, Far and 1-Pofd versus increasing thresholds.

In Fig. 4 we show the same indices at a fixed threshold of 20 mm/24h season by season. It is confirmed the general better results for Cosmo-EU and an underestimation for Cosmo-7. The slightly positive trend is significant and important for both the models.

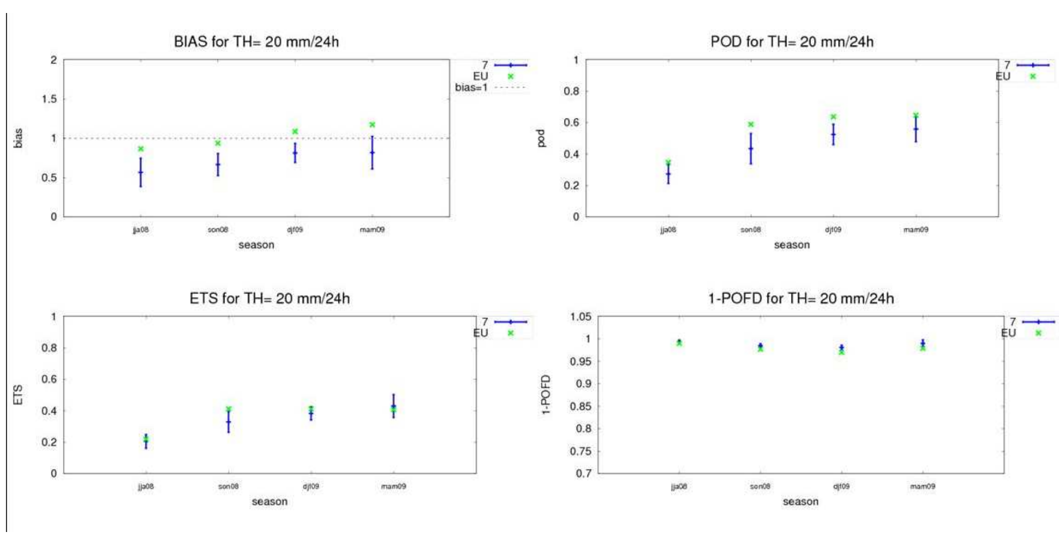

Figure 4: Bias, Pod, Ets, Far and 1-Pofd season by season.

Comparison between Cosmo-I7 and Cosmo-ME In Fig. 5 we plot Bias, Pod, Ets and 1-Pofd versus increasing thresholds considering a period from 200806 to 200905 and, in Fig. 6, the same indices season by season. The same results are obtained in both cases: similar and fairly good performances for the two versions, slightly better for Cosmo-ME.

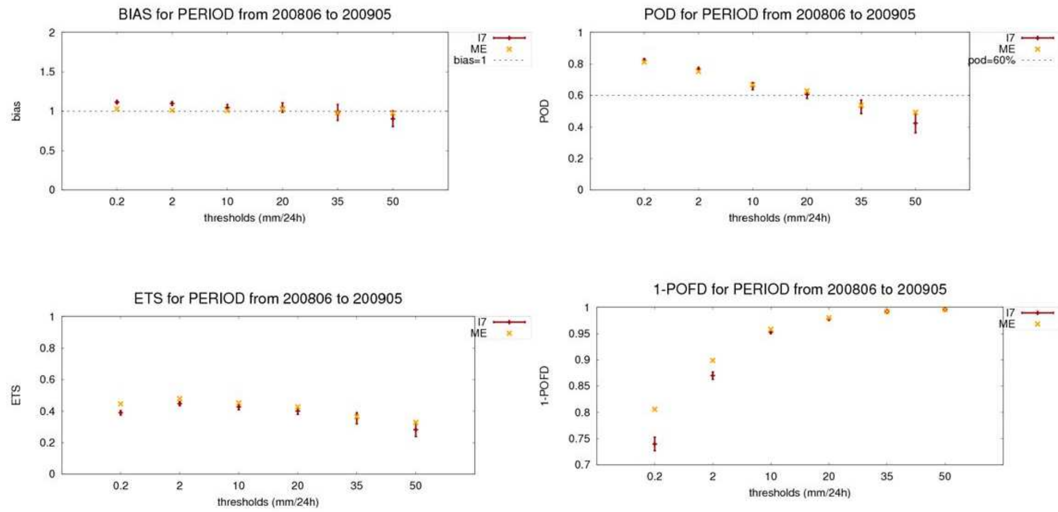

Figure 5: Bias, Pod, Ets, Far and 1-Pofd versus increasing thresholds.

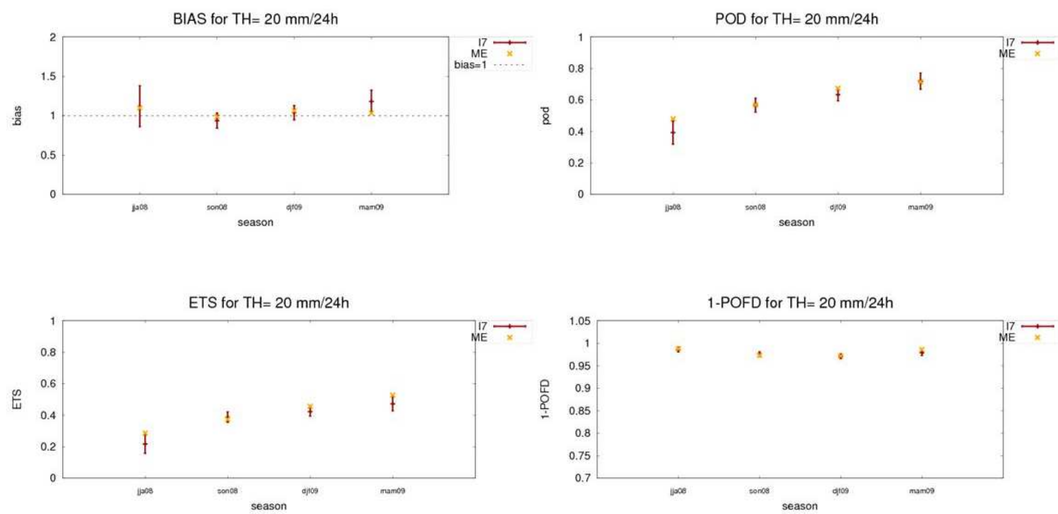

Figure 6: Bias, Pod, Ets, Far and 1-Pofd season by season.

Driving model comparison: Ecmwf, Cosmo-I7, Cosmo-I2

In the Fig. 7 the comparison among the three models versus increasing thresholds shows a general big gap between Ecmwf and the Cosmo-models. Moreover, Ecmwf overestimates for low thresholds and underestimates for the higher ones (it is an intrinsic feature and behaviour for hydrostatic and coarser models). In general, Cosmo-I7 is better than Cosmo-I2 (Cosmo-I2 underestimates the precipitation and, consequently, it has a smaller Far).

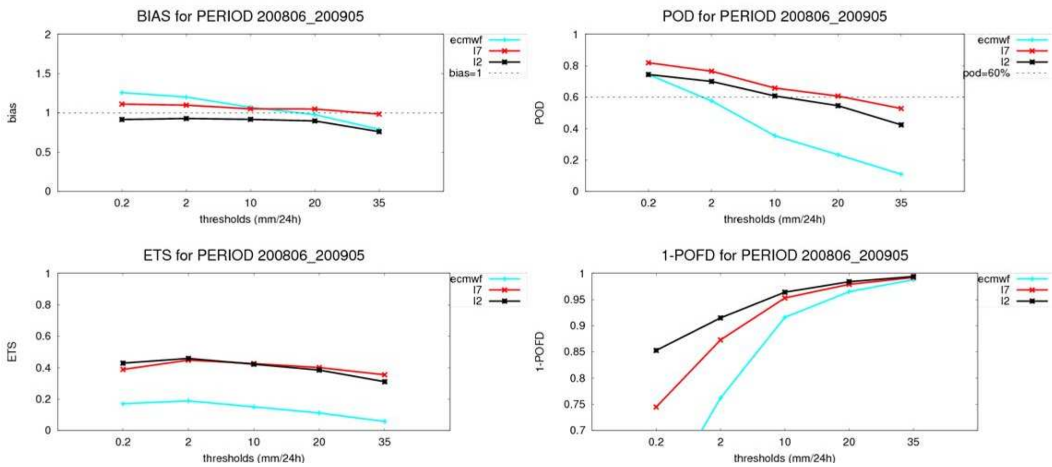

Figure 7: Bias, Pod, Ets, Far and 1-Pofd versus increasing thresholds.

In the following picture (Fig. 8) we plot the indices season by season at a fixed thresholds of 20 mm/24h: it is confirmed the big gap between Ecmwf and the Cosmo-models. Both Cosmo-models show a slightly positive trend, but Cosmo-I2 has got an underestimation tendency, more pronounced during summer (convective) periods.

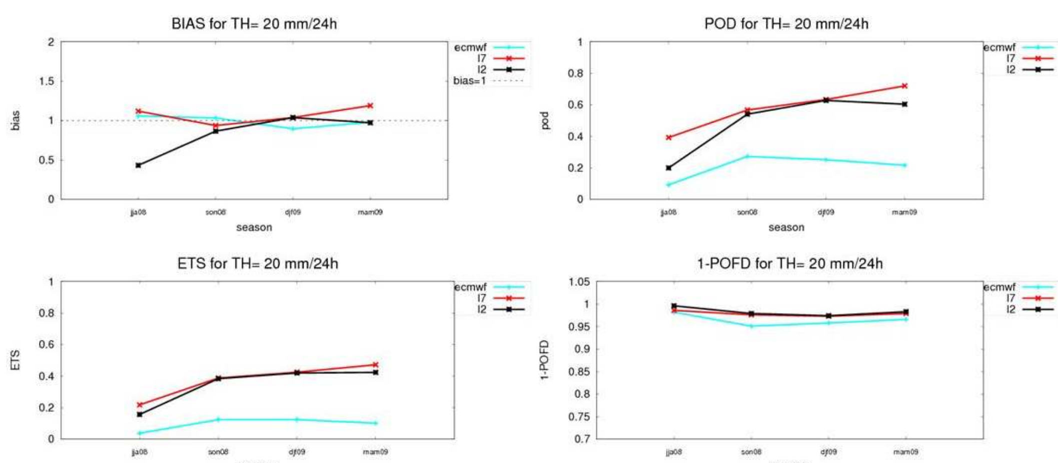

Figure 8: Bias, Pod, Ets, Far and 1-Pofd season by season.

Driving model comparison: Ecmwf, Cosmo-ME, Cosmo-IT

In Fig. 9 the comparison among the three models versus increasing thresholds shows again a general big gap between Ecmwf and the Cosmo-models. Cosmo-ME and Cosmo-IT display a similar behaviour, with an overestimation tendency by Cosmo-IT.

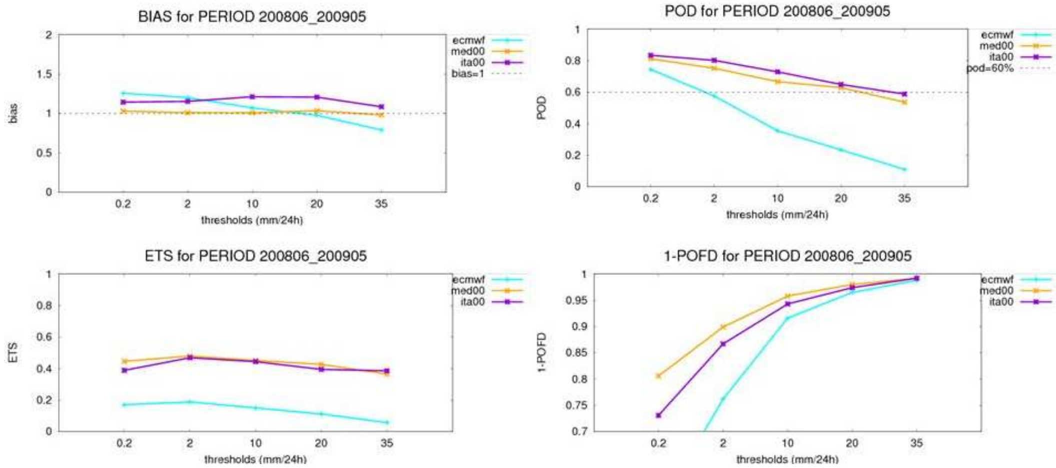

Figure 9: Bias, Pod, Ets, Far and 1-Pofd versus increasing thresholds.

In the following picture (Fig. 10) we plot the indices season by season at a fixed thresholds of 20 mm/24h: it is confirmed again the big gap between Ecmwf and the Cosmo-models. Both Cosmo-models have a similar performance, but Cosmo-IT overestimates quite a lot the precipitation, especially during summer (convective) periods.

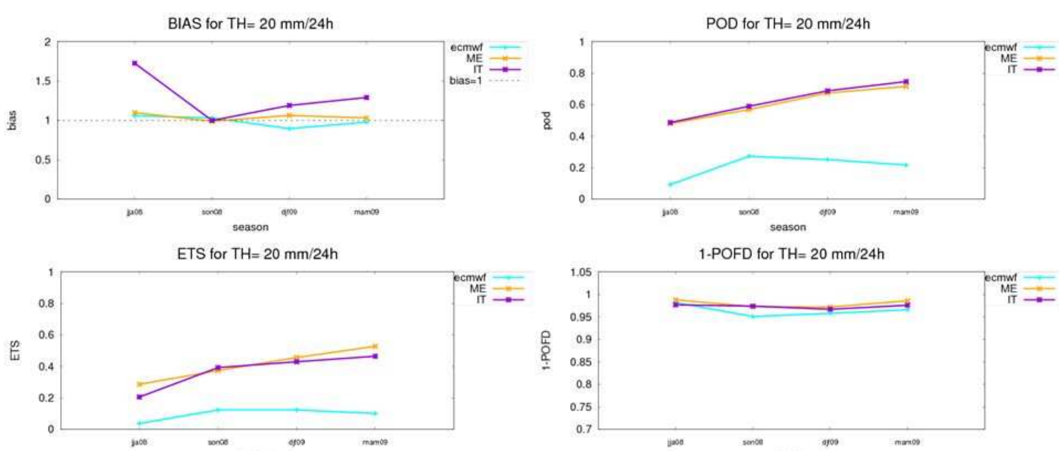

Figure 10: Bias, Pod, Ets, Far and 1-Pofd season by season.

The diurnal cycle

In the following picture (Fig. 11) we check the models features considering 6h integration precipitation starting from 06UTC to 72UTC forecast time. We analyze the behaviour of all the 6 model versions at low and higher threshold (0.2 mm and 10 mm) over the latest years. In particular, we note a Bias overestimation peak during midday for both thresholds and, moreover, it is confirmed an underestimation for Cosmo-7, more pronounced for high precipitation amounts. All the model versions, especially Cosmo-I7 and Cosmo-I2, present a spin-up problem for low thresholds, that seems to disappear for the higher ones where the models underestimate the precipitation during the first 6h. In general it is noticeable a slight improvement with respect to the previous years results.

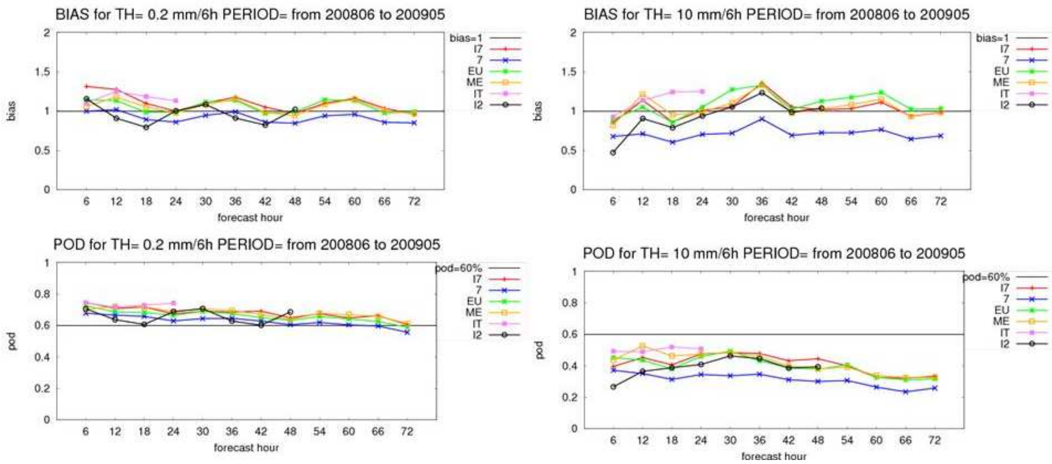

Figure 11: Diurnal cycle for Bias and Pod for 0.2 mm/6h and 10 mm/6h.

The spatial distribution of the error

Finally, the latest year skills and scores have been calculated over each meteo-hydrological basins in order to evaluate the spatial error distribution: here we show only the Bias for 10 mm/24h (Fig. 12) from 200806 to 200905 and the relative error (Fig. 13) for MAM 2009. Observing the Bias distribution over the territory (Fig. 12), apart from the general characteristics we have found before with the statistical indices, we can underline some more feature:

- all the versions overestimate the precipitation over the Alpine chain;
- there is a strong underestimation for Cosmo-7;
- there is a quite good general performance for Cosmo-ME, Cosmo-I7 and Cosmo-EU, with an underestimation over Southern Italy, Sardegna and Tyrrenian regions and an overestimation over the Adriatic area;
- there is an overestimation for Cosmo-IT and an underestimation for Cosmo-I2.

Eventually, Fig. 13 depicts the relative error distribution ((forecast-observed)/observed) in percentage during last spring:

- all the versions forecast too much precipitation over the Alpine chain;
- Cosmo-7 and Cosmo-I2 predict too less precipitation over some basins;
- Cosmo-IT predicts too much precipitation over some basins;
- Cosmo-I7 overestimates the precipitation in Central-Southern Italy;
- Cosmo-ME and Cosmo-EU have a general good performance.

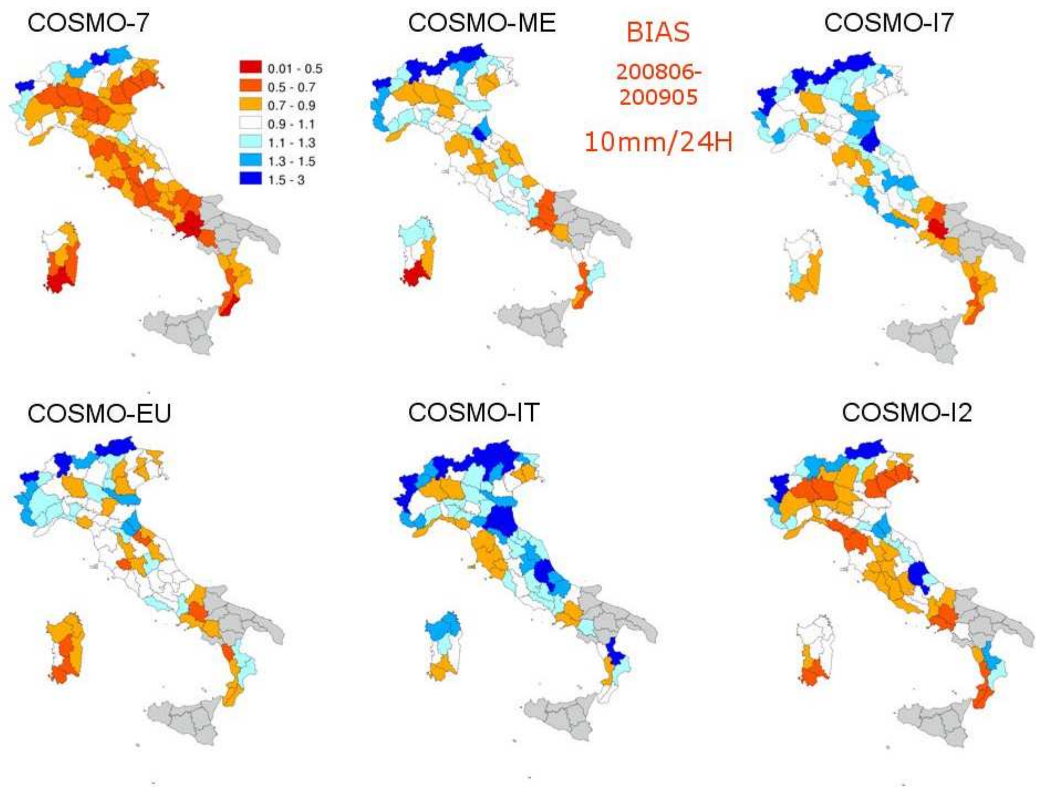

Figure 12: Bias spatial distribution for 10 mm/24h for MAM 2009.

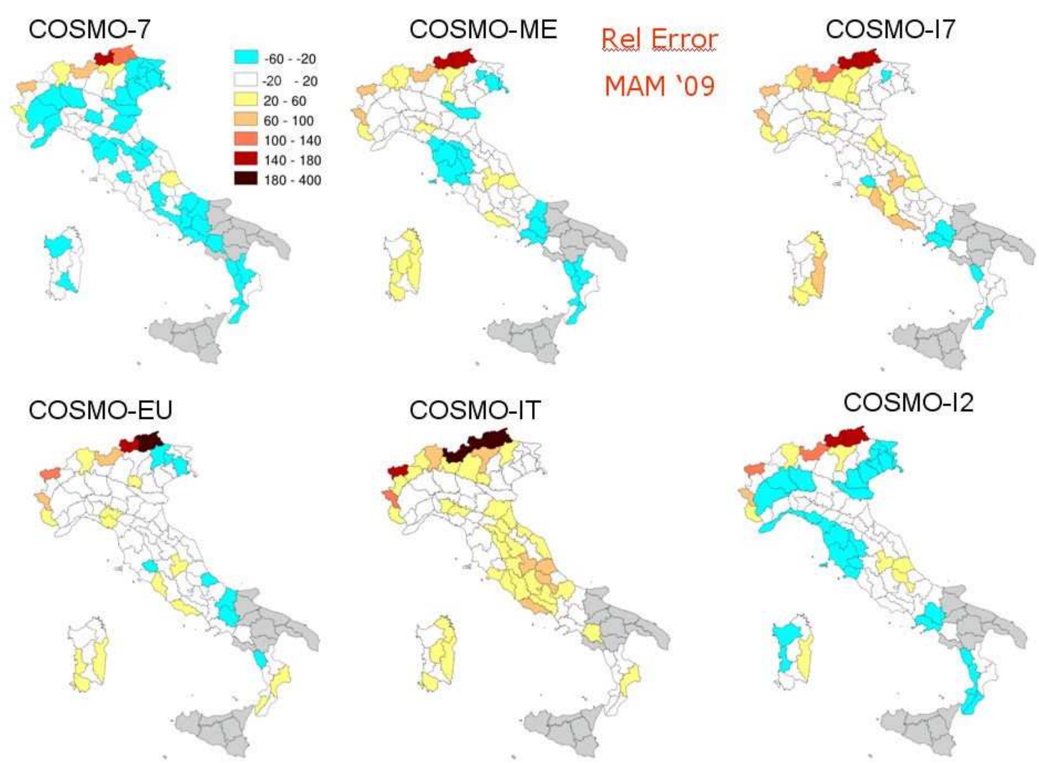

Figure 13: Relative error (%) distribution for MAM 2009.

Verification of COSMO-2 with independent data from a wind profiler

Christophe Hug, Pirmin Kaufmann and Dominique Ruffieux

Federal Office of Meteorology and Climatology MeteoSwiss, Zürich, Switzerland

Abstract

Wind profiler data collected during two field campaigns of 3 months each have been used as an independent measurement source to validate the high resolution numerical model COSMO-2 of MeteoSwiss. This action has taken place within a larger project for nuclear safety and emergency preparedness, aiming at the development of an improved high resolution weather prediction model for the Swiss Plateau.

Vertical profiles of wind direction and speed have been compared between wind profiler and model. The results of this verification show a bias close to zero for both parameters. This confirms that the model generally reproduces the air flow as observed at the location of the wind profiler. However the standard deviation of the model error is considerable, indicating that the model forecast cannot reproduce the profiler measurements during certains time periods.

1 Introduction

In order to renew and improve the current Swiss warning and dispersion forecast system for nuclear power plants (NPP), the Federal Office of Meteorology and Climatology MeteoSwiss has built up a new wind profiler network (Figure 1) and developed a new numerical model configuration COSMO-2 with a very high resolution of 2.2 km (Calpini 2008). The tools created for this purpose are the essential component of the CN-MET project. As part of the validation process of this project, two three-months field campaigns took place, a first from August to October 2008 and a second from mid-March to mid-June 2009. An independent mobile wind profiler has been located close to the sites of two different Swiss NPP and the data collected have been compared to model simulations.

2 COSMO Configuration

MeteoSwiss uses COSMO in two configurations: COSMO-7 with a grid spacing of 6.6 km for the short-range forecasting over the next 72 hours, and COSMO-2 with a grid spacing of 2.2 km for now-casting and short-range forecasting over the next 24 hours. The development of the higher resolution of COSMO-2 was for a large part induced by the performance expected from the new forecasting system developed in the framework of CN-MET.

COSMO-7 uses the lateral boundary conditions from the Integrated Forecast System (IFS) of the European Centre for Medium-Range Forecasts (ECMWF). A continuous assimilation cycle has been implemented, ingesting conventional surface observations as well as upper atmosphere soundings, aircrafts and wind profilers. Two daily 72 hours forecasts are calculated, based on the 00 and the 12 UTC analyses, with a 45 minutes cut-off time. At MeteoSwiss COSMO-7 is calculated on a 393 $\times$ 338 grid covering most of Western Europe. COSMO-7 provides the lateral boundary conditions for COSMO-2. The COSMO-2 domain of 520 × 350 grid points is centred over the Alps.

Model data are available on 60 model levels. Because model values represent a value averaged in space over one grid cell, turbulence is not represented on the model grid. The model wind therefore relates to a measurement with the turbulent contribution filtered by averaging over a time span of about half an hour to one hour.

The current configuration of COSMO-2 is operational since 27 February 2008. Assimilation of radar data with Latent heat nudging has been added in Spring 2008 mainly in order to improve the reproduction of convective precipitation. Because consecutive COSMO-2 forecasts are started every three hours and cover 24 hours, each verification time is available in 8 different model forecasts with the respective 8 different lead times. This redundancy is an additional security element.

3 Wind profiler data

The first field campaign took place in the northern part of Switzerland half way between the two NPPs Leibstadt and Beznau (Figure 1; Ruffieux et al. 2009). A site representative to the Leibstadt-Beznau region and to the confluence of the Aare valley with the Rhine Valley was chosen. It is located north of Kleindöttingen, halfway between Leibstadt and Beznau, next to the Aare River. The second field campaign was conducted near the NPP Mühleberg. The wind profiler was located in Wileroltigen, a site representative for the Saane and Aare valleys west of Mühleberg (Figure 2).

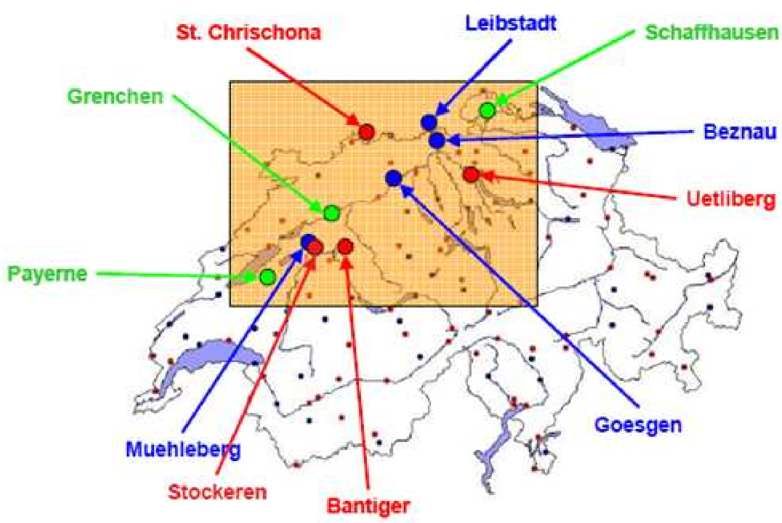

Figure 1: Overview of the CN-MET Network

The data were processed and went trough a 1^{st} level automatic quality control. At the end of the campaign, an operator made a manual 2^{nd} level QC. The wind profiler has been operated in two modes, delivering two sets of quasi simultaneous data. The low-mode measured up to 1'100 m above ground and the high mode went to almost 4'500 m. The characteristics of the mobile wind profiler are summarised in Table 1. The temporal resolution of the measurement available for the model comparison has been set to 30 minutes during the first campaign and to 60 minutes during the second campaign.

Figure 2: Vaisala mobile wind profiler during the second field campaign (March to June 2009) in the vicinity of the power plant of Mühleberg.

low mode	high mode
$\Delta H = 72$ m	$\Delta H = 205$ m
440 - 1452 m MSL	675 - 4773 m MSL

Table 1: Key numbers of the wind profiler configurations for low-mode and high-mode operation modes.

4 Verification method

Model outputs were available every 10 minutes for the purpose of the validation study. Since wind profiler data have been produced every 30 or 60 minutes, corresponding time stamps have then been used for the comparison. The observation data have been interpolated to model height to perform the comparison during the first campaign, and to profiler hight during the second campaign. Data of the 3 months field campaigns served as basis for the analysis. In order to avoid problems with high variability of the wind direction for low winds, winds with a speed lower than 3 m s^{-1} have been removed from the sample for wind statistics. The products that have been generated for the validation and assessment of the model quality include upper-air verification profiles, histograms of model error, and scatter plots of observed values versus mode values. All products have been created for both low-mode and high-mode wind profiler data and for the wind-speed threshold mentioned above. The profile verification for two sites will be shown in the next section.

5 Results

Vertical profiles of wind direction and speed have been compared between wind profiler and model. The verification shows a bias close to zero for both parameters (Figure 3). This confirms that the model generally reproduces the air flow as observed at the location of the independent wind profiler. However the standard deviation of the model error is quite large, indicating that the model forecast is inaccurate over short time periods. This occurs during rapidly changing weather conditions, when the model does not reproduce the fast changing and sometimes back and forth switching of the measured airflow. A comparison with the operationally assimilated wind profiler in Payerne (Figure 4) shows a smaller standard deviation for the wind direction, although not as small as when the verification is done with the radio sonde (not shown), which is assimilated during the analysis cycle. The wind speed bias is very close to zero at Payerne, but the wind direction shows a small bias of about 5° below 4000 m a.s.l. This systematic bias is to a smaller extent also found in the operational COSMO-2 verification with the radio soundings of Payerne and in the surface verification (Schubiger et al. 2008). The standard deviation is around 40° at the lower levels at both sites, and in Payerne decreases to around 10°-30° towards the top of the profile. The low-mode results (not shown here) show a value about 5° larger. Finally a very positive conclusion is that the quality of the forecast remains very high over the initial 6 hours of the model forecast, indicated by all curves in the Figures 3 and 4 that remain in the same range for bias and standard deviation.

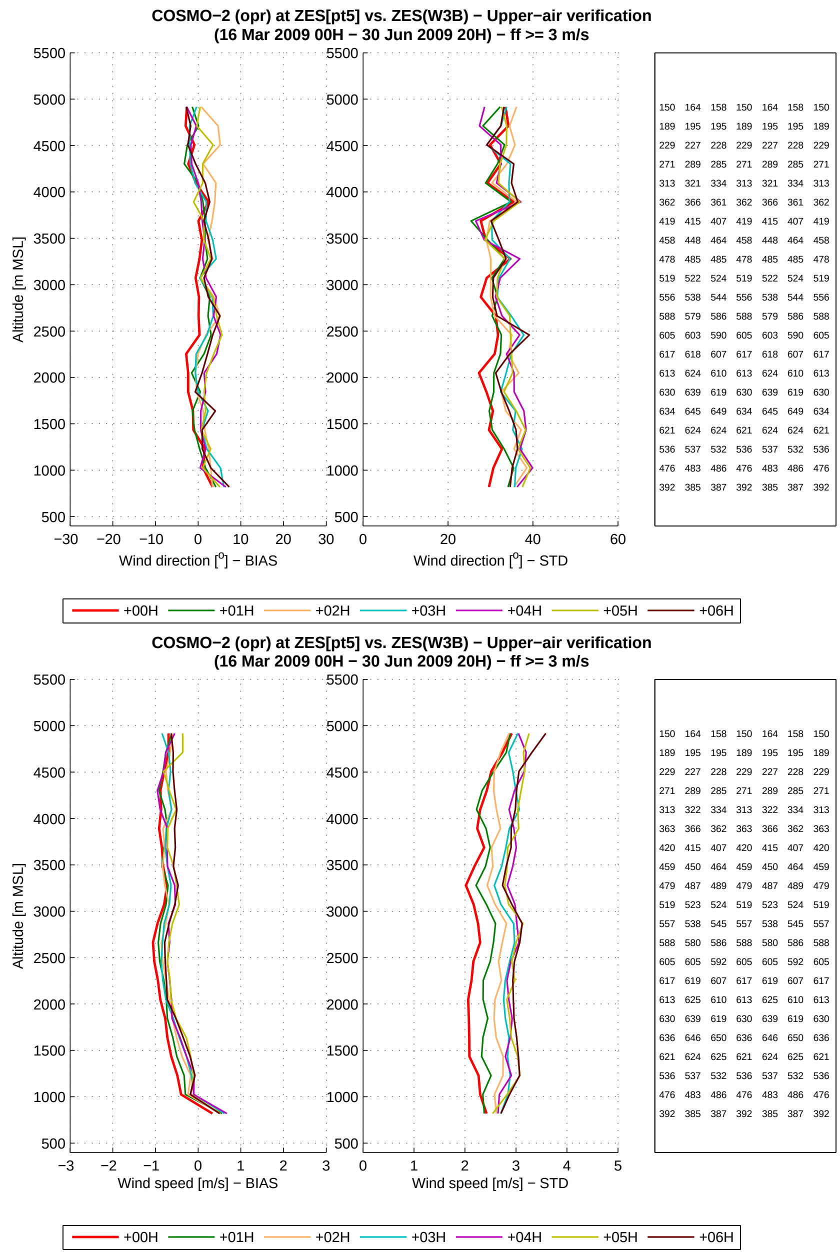

Figure 3: Vertical profiles of (left) model bias and (middle) standard deviation for the first 6 forecast hours versus wind profiler in Mühleberg. The numbers in the box on the right show the number of cases. The top figure shows the statistics for wind direction and the bottom figure for speed, in both cases restricted to measurements with wind speed above 3 m s^{-1}.

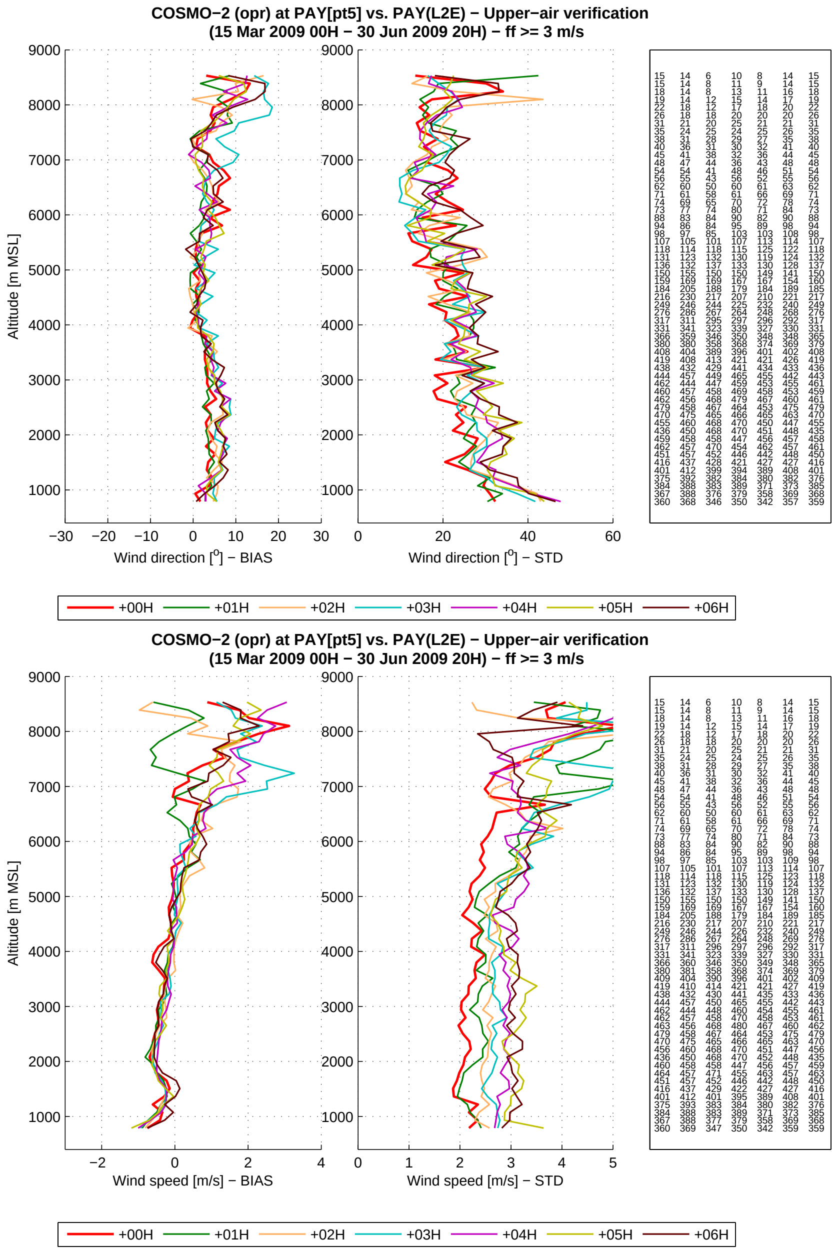

Figure 4: As Figure 3 but for the assimilated operational profiler in Payerne.

6 Conclusions

Wind profiler data have been collected during a three months field campaign in the complex topography of the Swiss Jura, and the north slope of the Alps. The high resolution model COSMO-2 has been compared to these data for the first 6 hours of forecast and a good average agreement between observation and model could be found especially for the upper levels of the vertical profile. In the lower part of the profile, a slight positive bias can be observed for both wind speed and wind direction. The results show only a minor decrease of quality of the forecast over the first 6 hours. The standard deviation however appears to be considerable. This indicates that the timing of the model is sometimes incorrect. Analysis of individual events demonstrate this behaviour (see for example Ruffieux et al. 2009).

Acknowledgments

The authors would like to thanks Bertrand Calpini initiator and leader of the CN-MET project, and Philippe Steiner for useful comments during the analysis of the results. The field campaigns have been planned and organised by Pierre Huguenin and Olaf Maier.

References

[1] Calpini, B., 2008: Surface and Upper-air recent developments at MeteoSwiss. The WMO Technical Conference on Meteorological and Environmental Instruments and Methods of Observation TECO 2008, 27-29 November 2008, St. Petersburg, Russia

[2] Ruffieux D., P. Huguenin, B. Calpini, Ch. Hug, O. Maier, 2009: Ground-based remote sensing profiling and NWP model to manage nuclear power plants meteorological surveillance in Switzerland, 8^{th} International Symposium on Tropospheric Profiling: Integration of Needs, Technologies and Applications ISTP 2009, 18-23 October 2009, Delft, The Netherlands.

[3] Ch. Hug, P. Kaufmann, D. Ruffieux, 2009: Validation of the high resolution numerical weather prediction model COSMO-2 with independen wind profiler measurement data, 8^{th} International Symposium on Tropospheric Profiling: Integration of Needs, Technologies and Applications ISTP 2009, 18-23 October 2009, Delft, The Netherlands.

[4] Schubiger F., P. Kaufmann, A. Walser, E. Zala, 2008: WG5-Report from Switzerland: Verification of the COSMO model in the Year 2006. *COSMO Newsletter 7* (available at http://www.cosmo-model.org) , **91-99**, Deutscher Wetterdienst DWD, Offenbach, Germany.

Retrieving tornado's like wind structure (20.07.2007, Czestochowa, Poland case) using singular radar Doppler velocity

Jan Parfiniewicz

Institute of Meteorology and Water Management
61 Podlesna str., PL-01673 Warsaw, Poland

1 Poland case, 20.07.2007

This is an addendum to Tornado Case, Parfiniewicz, 2008, presenting results of direct retrieval of Doppler radar measurements from Brzuchania. The applied method of retrieval resembles techniques known as ECUW (combination of Continuity with the uniform wind technique, Hagen,2002) and VVP (velocity volume processing, Koscielny et al., 1982) but was developed purely independently on experimental manner. The final algorithm consists of 3 main steps (the order is important):

1. Retrieval of tangential wind component on polar grid circles (or part of them depending on the domain) by solving differentiated continuity equation by tridiagonal TDMA solver.
2. Retrieving averaged Cartesian components from retrieved on the step 1 polar components, accounting strictly for proper metrics transformation from polar to Cartesian grid, when using least square method. The 3D volume estimated to provide best results is 1 km in vertical (3 levels) and 28 km ($\pm 14km$, 5 grids of 2.8km) in horizontal. It was necessary to apply this procedure twice (first for horizontally reduced volume) - possibly to compensate aliasing bias, Gao & Droegemeier, 2004.
3. Finally, instead of formal mixing (or smoothing) the 2D "Cartesian model" with nudging term on rhs (replacing pressure gradient) that assures convergence to radial measurements was introduced. 20 iterations (for $dt = \pm 20s$ with changeable sign every 3 iterations) were found enough, and confirmed stability of solution, even when tested for 1000 iterations.

The result is presented via 3D streamlines: Fig. 1

2 Post Scriptum

The result concerning tornado and presented above was obtained by merging modeled wind field (as a first guess) with embedded radial Doppler velocities. As for operational needs we were forced to test pure retrieval, without modeled wind on input. The same was checked on the tornado case, showing nearly identical results in vertical wind component while significant differences in horizontal ones - thus modifying 3D picture by enhancement of vertical movement. This is not presented here since it was recognized as less credible, thus confirming positive impact of modeled wind on Doppler radar retrieval. Acknowledgment: to Bogdan Rosa for stimulating talks.

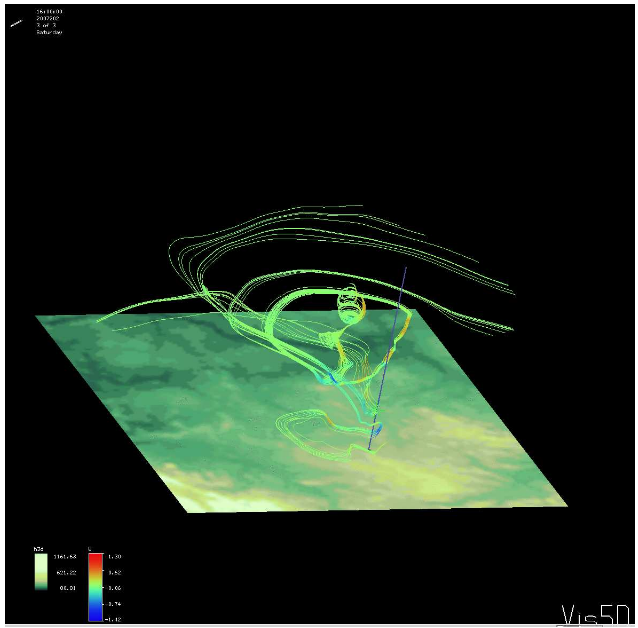

Figure 1: Vis5d was used to obtain 3D streamlines as set of characteristic trajectories. They are colored by w - vertical velocity in m/s. Scaling for w and topography (in m) is included. Vertical line indicates tornado localization. Descending spiral motion, that is beginning at about 7 km, is dominating it reaches maximum downward velocity just above tornado.

References

[1] M. Hagen, K. Friedrich, and J. Seltmann: Wind-field observations with the operational Doppler radar network in Germany, Proceedings of ERAD (2002): **195-199** Copernicus GmbH 2002, ERAD 2002

[2] Koscielny, A.J., Doviak, R.J., and Rabin, R., Statistical considerations in the estimation of divergence from single-Doppler radar and application to prestorm boundary-layer observations. *J. Appl. Meteorol.*, 21, **197-210, 1982**.

[3] Jidong Gao, Kelvin K. Droegemeier, A variational technique for daaliasing Doppler Radial Velocity data, *J. Appl. Meteorol.*, 43, **934 - 940**, 2004

[4] J. Parfiniewicz, 20th of July 2007 explosive convection over Europe. The COSMO perspective. *COSMO Newsletter No. 9*, **79 - 85**, 2008

Overview of operational verification results in Poland

Katarzyna Starosta and Joanna Linkowska

Institute of Meteorology and Water Management, Centre of Numerical Weather Prediction, Warsaw

1 Introduction

A goal of this work is to summarize the main results of operational verification in Poland. The verification results of a few continuous meteorological parameters, as well as 12 and 24h accumulated precipitation are presented in this paper.The fields from COSMO_PL had been verified with 58 Polish SYNOP stations. The model configuration was: 14 km horizontal grid spacing, initial time at 00 UTC, the forecast range 72 h. To verify the diurnal behavior of the model, the couples forecast-observation were stratified according to the hour of the day (3 hourly frequency for continuous parameters) and the season of the year.The verification was performed using a new verification tool - VERSUS. The verification results from June 2008 to May 2009 are shown bellow.

2 The verification method

The mesoscale COSMO_PL had been verified for four seasons for the selected period (JJA, SON, DJF, MAM). The verification was performed for following parameters: temperature at 2m a.g.l, the air pressure at sea level, the wind speed at 10m e.g.l., 12h and 24h accumulated precipitation. For continuous parameters the mean error (ME), the mean absolute error (MAE) and the root mean square error (RMSE) were calculated. For the accumulated precipitation indices FBI, POD, FAR, ETS from contingency table were calculated. For the precipitation verification following thresholds were taken into account: 0.2, 0.4, 0.6, 0.8, 1, 2, 3, 4, 5, 6, 7, 8, 9, 10, 12, 14, 16, 18, 20 mm.

3 Results

3.1 The 2m temperature

Figures 1-4 present a behavior of 2 m temperature forecast errors for all the set of Polish stations. The diurnal and seasonal cycles were observed. The errors were bigger in summer than in winter time. During half-yearly period from May to August (MAM,JJA) diurnal cycle was marked with large amplitude for ME, MAE, RMSE. The errors reached maximum values around 3UTC and 15 UTC The cold bias was observed during the day and warm bias during the night time. The diurnal amplitude of ME took values in the range (0, -2,5) in DJF. The maximum of errors occurred at midday. The ME was negative for the whole forecast range. ME behavior was quite similar in summer, autumn and spring but the smaller errors were observed in autumn. In SON the maximum values of ME were at 3 UTC and 12 UTC.

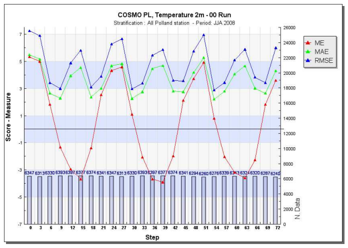

(a) ME, MAE,RMSE, Temperature 2m, JJA 2008, Poland

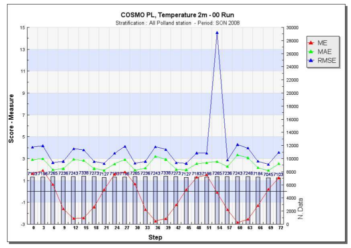

(b) ME, MAE,RMSE, Temperature 2m, SON 2008, Poland

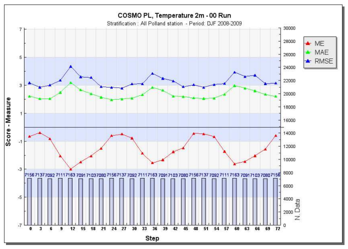

(c) ME, MAE,RMSE, Temperature 2m, DJF 2008/2009, Poland

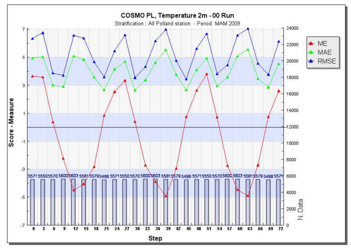

(d) ME, MAE,RMSE, Temperature 2m, MAM 2009, Poland

Figure 1: Temperature verification results over Poland

3.2 The sea level pressure

Figures 5-8 show ME, MAE, RMSE for the pressure reduced to mean sea level. For all the seasons we observed clear increasing tendency of RMSE and MAE with the forecast step. No clear tendency of ME was noticed. The errors (RMSE, MAE) were smaller in the summer than in the winter. ME error was near zero (-0.5 0.5) in the autumn and winter. The amplitude of ME was bigger in the spring and summer and took the range (-1.0-1.0).

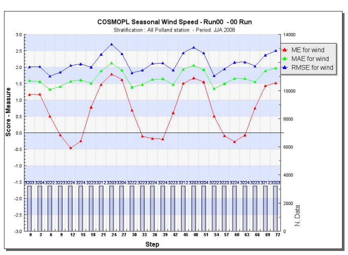

(a) ME, MAE,RMSE, Sea level pressure, JJA 2008, Poland

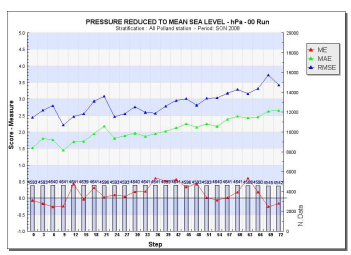

(b) ME, MAE,RMSE, Sea level pressure, SON 2008, Poland

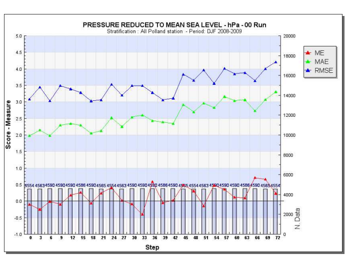

(c) ME, MAE,RMSE, Sea level pressure, DJF 2008/2009 Poland

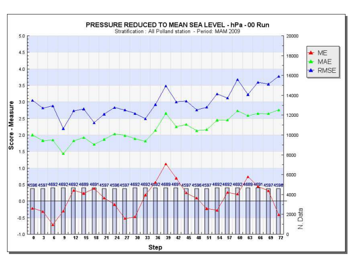

(d) ME, MAE,RMSE, Sea level pressure, MAM 2009, Poland

Figure 2: SLP verification results over Poland

3.3 The wind speed 10m above ground level

The verification results of the wind speed 10m above ground level are presented in figures 9-12. Very explicit seasonal runs of errors with a division for two half-yearly period were noticed. For the first period, summer 2008 and spring 2009, we observed explicit diurnal cycle of all errors (RMSE, MAE, ME) with maximum at midnight. ME was above zero during the night and below zero during the day. For the second period, September 2008-February 2009, the amplitude of errors was small. Despite of the small amplitude of ME clear diurnal cycle was observed.

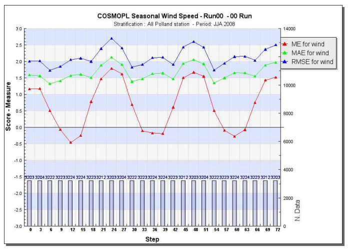

(a) ME, MAE,RMSE, Wind speed 10m, JJA 2008, Poland

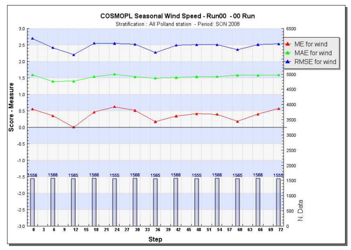

(b) ME, MAE,RMSE, Wind speed 10m, SON 2008, Poland

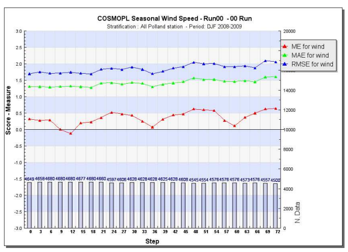

(c) ME, MAE,RMSE, Wind speed 10m , DJF 2008/2009, Poland

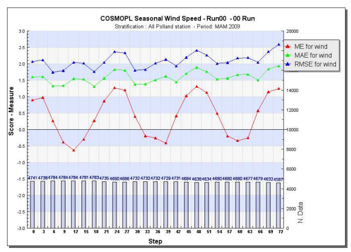

(d) ME, MAE,RMSE, Wind speed 10m, MAM 2009, Poland

Figure 3: 10m wind speed verification results over Poland

3.4 12h and 24h accumulation precipitations

Figures 13-28 show verification of 12h accumulated precipitations and figures 29-44 show 24 h accumulated onces. For both precipitation sums an overestimation was noticed for small thresholds (0-2.0 mm) and underestimation for higher thresholds. FBI plots decreased rapidly for higher thresholds. The results of FBI were better for JJA and MAM. Also POD diminution with the precipitation thresholds was observed. The curve broke down rapidly around the threshold of 2 mm. FAR increased monotonous with precipitation thresholds. The results were better for the first day of forecast. ETS score was quite low for the all seasons and the precipitation sums. Almost no skill level was noticed. For all indices the results of verification were better for 24h accumulated precipitation than for 12h accumulated precipitation.

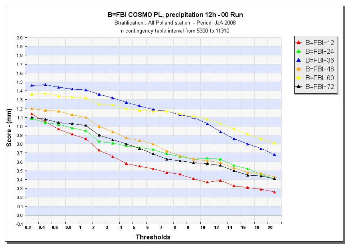

(a)

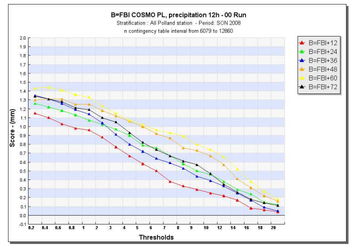

(b)

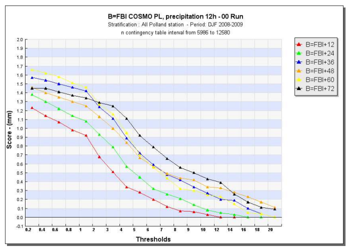

(c)

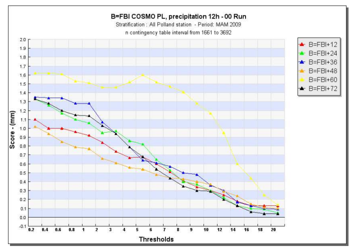

(d)

Figure 4: FBI , 12h accumulated precipitation, June 2008-May 2009, Poland

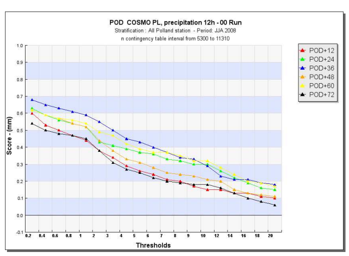

(a)

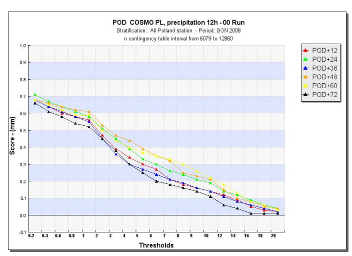

(b)

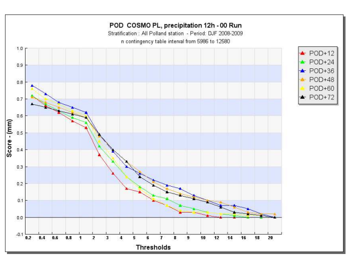

(c)

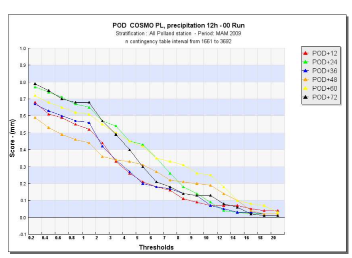

(d)

Figure 5: POD, 12h accumulated precipitation, June 2008-May 2009, Poland

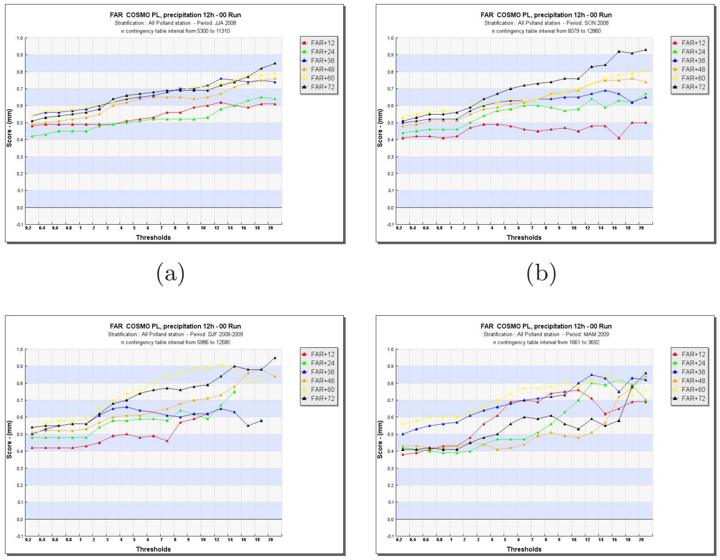

(a) (b)

(c) (d)

Figure 6: FAR, 12h accumulated precipitation, June 2008-May 2009, Poland

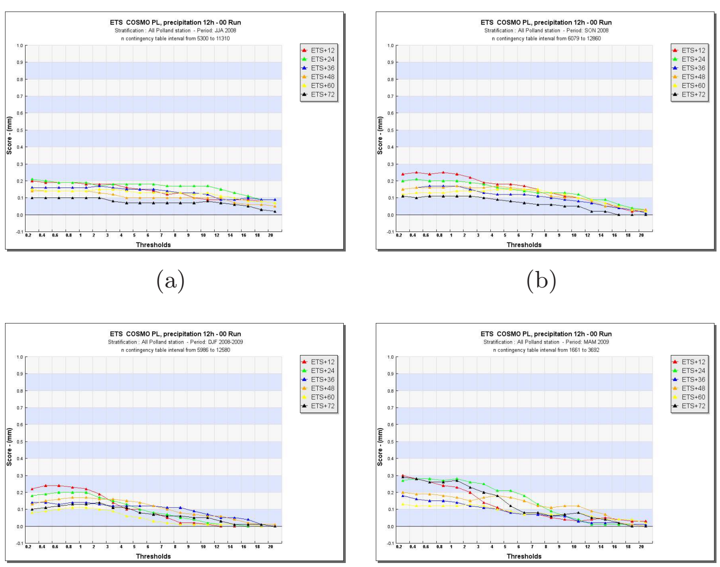

(a) (b)

(c) (d)

Figure 7: ETS, 12h accumulated precipitation, June 2008-May 2009, Poland

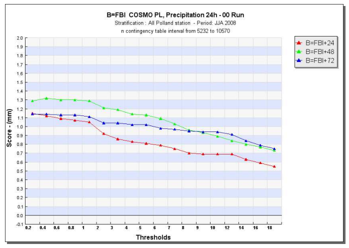

(a)

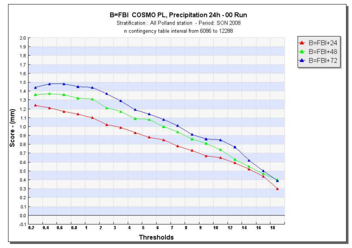

(b)

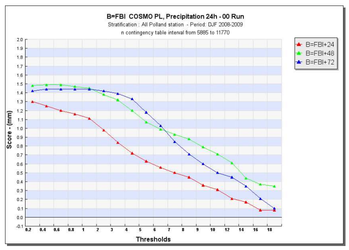

(c)

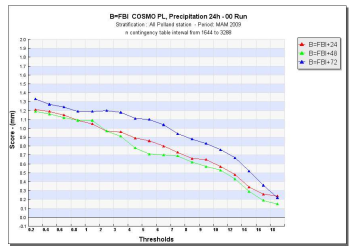

(d)

Figure 8: FBI, 24h accumulated precipitation, June 2008-May 2009, Poland

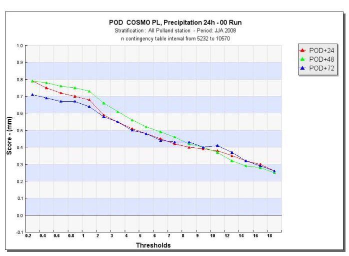

(a)

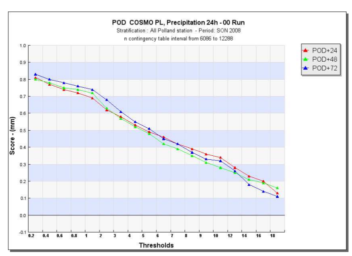

(b)

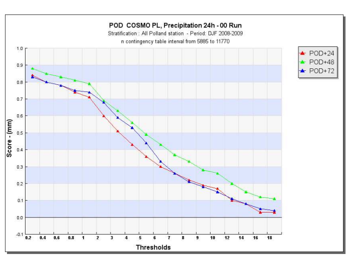

(c)

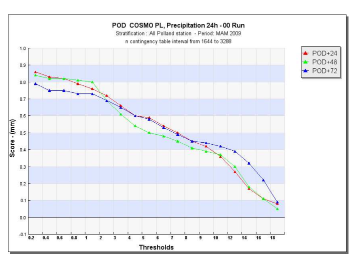

(d)

Figure 9: POD, 24h accumulated precipitation, June 2008-May 2009, Poland

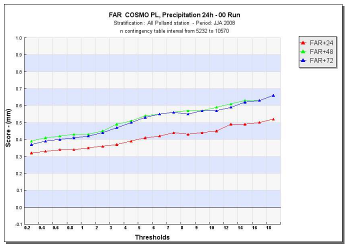

(a)

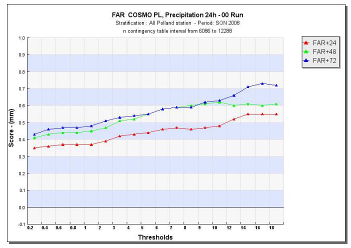

(b)

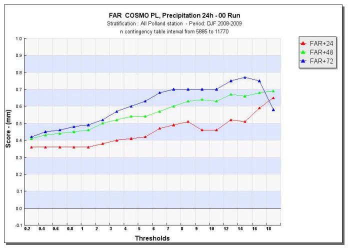

(c)

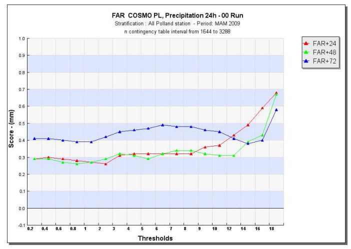

(d)

Figure 10: FAR, 24h accumulated precipitation, June 2008-May 2009, Poland

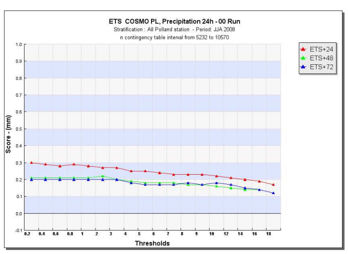

(a)

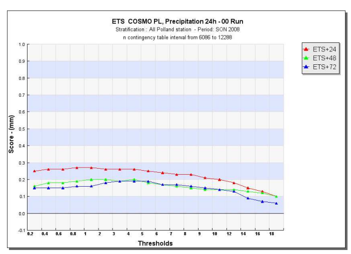

(b)

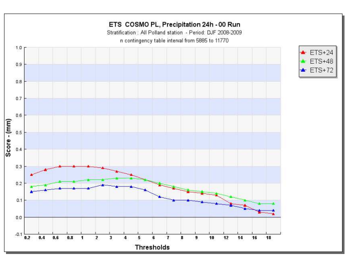

(c)

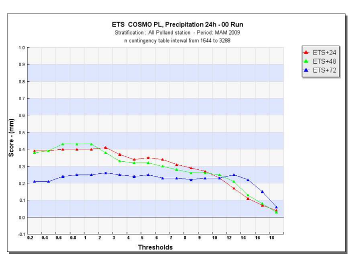

(d)

Figure 11: ETS, 24h accumulated precipitation, June 2008-May 2009, Poland

4 Conclusions

Operational verification results using a new verification tool VERSUS was presented in this paper. Diurnal, seasonal and half-yearly period cycles of the errors were observed for the 2 m temperature and the wind speed. The model seems to underestimate 2m temperature for the winter time. For remaining seasons the temperature is underestimated during the day and overestimated during the night. For all seasons the wind speed is always overestimated during the day. MAE and RMSE of sea level pressure increase with the forecast time. The model underestimates the precipitation for higher thresholds. The verification results were obtained better for 24 h accumulated precipitation.

References

[1] I.T.Jolliffe, D.B.Stephenson, 2003. Forecast Verification, A Practitioners Guide in Atmospheric Science, *WILEY* D.S. Wilks, 1995. Statistical Methods in the Atmospheric Science *Academic Press*

[2] Zepeda-Arce, J, E. Foufoula-Georgiou, and K. Droegemeier, 2000. Space-time rainfall organization and its role in validating quantitative precipitation forecasts, *J. Geophysical Research*, 105(D8), **10**,129-**10**,146.

List of COSMO Newsletters and Technical Reports

(available for download from the COSMO Website: `www.cosmo-model.org`)

COSMO Newsletters

No. 1: February 2001.

No. 2: February 2002.

No. 3: February 2003.

No. 4: February 2004.

No. 5: April 2005.

No. 6: July 2006; Proceedings from the COSMO General Meeting 2005.

No. 7: May 2008; Proceedings from the COSMO General Meeting 2006.

No. 8: August 2008; Proceedings from the COSMO General Meeting 2007.

No. 9: December 2008; Proceedings from the COSMO General Meeting 2008.

No.10: January 2010; Proceedings from the COSMO General Meeting 2009.

COSMO Technical Reports

No. 1: Dmitrii Mironov and Matthias Raschendorfer (2001):
Evaluation of Empirical Parameters of the New LM Surface-Layer Parameterization Scheme. Results from Numerical Experiments Including the Soil Moisture Analysis.

No. 2: Reinhold Schrodin and Erdmann Heise (2001):
The Multi-Layer Version of the DWD Soil Model TERRA_LM.

No. 3: Günther Doms (2001):
A Scheme for Monotonic Numerical Diffusion in the LM.

No. 4: Hans-Joachim Herzog, Ursula Schubert, Gerd Vogel, Adelheid Fiedler and Roswitha Kirchner (2002):
LLM ⁻ the High-Resolving Nonhydrostatic Simulation Model in the DWD-Project LITFASS.
Part I: Modelling Technique and Simulation Method.

No. 5: Jean-Marie Bettems (2002):
EUCOS Impact Study Using the Limited-Area Non-Hydrostatic NWP Model in Operational Use at MeteoSwiss.

No. 6: Heinz-Werner Bitzer and Jürgen Steppeler (2004):
Description of the Z-Coordinate Dynamical Core of LM.

No. 7: Hans-Joachim Herzog, Almut Gassmann (2005):
Lorenz- and Charney-Phillips vertical grid experimentation using a compressible nonhydrostatic toy-model relevant to the fast-mode part of the 'Lokal-Modell'

No. 8: Chiara Marsigli, Andrea Montani, Tiziana Paccagnella, Davide Sacchetti, André Walser, Marco Arpagaus, Thomas Schumann (2005):
Evaluation of the Performance of the COSMO-LEPS System

No. 9: Erdmann Heise, Bodo Ritter, Reinhold Schrodin (2006):
Operational Implementation of the Multilayer Soil Model

No. 10: M.D. Tsyrulnikov (2007):
Is the particle filtering approach appropriate for meso-scale data assimilation?

No. 11: Dmitrii V. Mironov (2008):
Parameterization of Lakes in Numerical Weather Prediction. Description of a Lake Model.

No. 12: Adriano Raspanti (2009):
Final report on priority project VERSUS (VERification System Unified Survey).

No. 13: Chiara Mirsigli (2009):
Final report on priority project SREPS (Short Range Ensemble Prediction System).

No. 14: Michael Baldauf (2009):
COSMO Priority Project "Further Developments of the Runge-Kutta Time Integration Scheme" (RK); Final Report.

No. 15: Silke Dierer (2009):
COSMO Priority Project "Further Developments of the Runge-Kutta Time Integration Scheme" (RK); Final Report.

No. 16: Pierre Eckert (2009):
COSMO Priority Project "INTERP"; Final Report.